The oxidation of the (100) surface of the intermetallic alloys Ni_3Al and CoAl and the growth of Co on the clean and oxidized $N_3Al(100)$ surface

I n a u g u r a l - D i s s e r t a t i o n
zur
Erlangung des Doktorgrades der
Mathematisch-Naturwissenschaftlichen Fakultät
der Heinrich-Heine-Universität Düsseldorf

vorgelegt von

Ioan Costina
aus Alesd/Rumänien

Februar 2002

Gedruckt mit der Genehmigung der Mathematisch-Naturwissenschaftlichen Fakultät der Heinrich-Heine-Universität Düsseldorf

1. Referent: Prof. Dr. René Franchy

2. Korreferent: Prof. Dr. Klaus Schierbaum

Tag der mündlichen Prüfung: 18.10.2002

Contents

List of Figures

List of Tables

Introduction

Thin film structures and self-assembled nano-particles supported on various substrates became in recent years of fundamental importance in so far as these have dimensions low enough to give unusual physical properties with respect to those of the bulk. Electronic devices, coatings, sensors, displays, heterogeneous catalysis and other numerous technologies are strongly dependent on the quality of thin films.

The oxidation of binary alloys has attracted a considerable interest because, for various systems, the growth of epitaxial oxide overlayers was observed [1]. For practical applications, the thin oxide films must be highly reproducible in composition and thickness. One way of preparing thin oxide layers, presented in this work, is the *in situ* thermally controlled oxidation of the surface of binary alloys. Ni-Al, Fe-Al, Co-Al and Co-Ga compounds, in various stoichiometry, are suitable alloys for the preparation of thin alumina films through direct oxidation [1]. In general, *in situ* oxidation of the surface of these alloys at room temperature, leads to a thin, amorphous Al_2O_3 or Ga_2O_3 film, respectively. Annealing of these films at higher temperatures, or the oxidation directly at high temperature results in well-ordered, thin oxide films. The thickness of the oxide films ranges between 5 and 20 Å. The structure and properties of the thin oxide film are still an open questions. The structure and symmetry of the substrate, as well as the preparation temperature are key factors which determine the structure of the oxide film.

The discovery, in the early 1990s, of the Tunnel Magnetoresistance (TMR) effect [2, 3] renewed the interest in the study of thin alumina films. The TMR effect is

based on the fact that tunneling of electrons between two magnetic layers depends on the relative orientation of the magnetization between the ferromagnetic layers. The magnetic layers, are separated, in the case of TMR structures, by an insulator. The current flows perpendicular to the film plane, and the best results (highest magnetoresistance amplitude) were achieved with aluminum-oxide tunnel barriers [4]. In the tunneling experiments, the thickness of the tunneling barriers has to be homogeneous over the entire substrate and should have values around 10-20 Å. Thus, the knowledge about the oxidation process of the surface of intermetallic alloys can serve to handle the process of growing of uniform oxide layers with defined thickness.

Nanometer-sized metallic clusters are now also being used in experimental electronic devices [5]. The insertion of a layer of cobalt aggregates in the insulator of a tunnel junction between two magnetic electrodes combines the giant magnetoresistance [6] with Coulomb blockade [7]. Using these two effects several types of future devices, such as microscopic magnetic reading heads and magnetically operated logic gates, could be developed.

For microelectronics the differences of the magnetic properties of thin layers with respect to those of the bulk system play a significant role [8]. Planar junctions (grown layer-by-layer) or rough interfaces are preferred in many applications, but granular systems (obtained by three-dimensional growth) can also be technologically interesting. An example are the devices using TMR effect. Planar junctions of two magnetic materials separated by a thin insulator present a high TMR effect at room temperature and small magnetic fields [2]. Granular systems, having a special design, can also present a TMR effect at low external field [9]. The influence of the architecture and size of the granular system on the device quality based on TMR and Coulomb blockade effect was pointed out in Ref. [10].

The large number of factors involved in the growth of a material deposited on a substrate (mismatch of lattice parameter between deposit and substrate, the balance between free energies and adhesion energy of the two components etc.) make an *a priori* prediction about a specific growth mode very difficult.

The aim of this work was to study the early stages and the mechanisms of oxide growth on the (100) surface of Ni_3Al and CoAl in ultra high vacuum (UHV) conditions. Another purpose was to prepare a well-defined TMR model system by deposition of Co on the Al_2O_3 layer grown on Ni_3Al.

The thesis is structured as follows:

In Chapter 1 is presented the theoretical background of experimental methods. Evidences for the complementarity of the methods used are presented.

Chapter 2 comprises the basics of growth processes (thermodynamic and kinetic aspects), as well as of the oxidation process necessary for the analysis of the experimental results.

In Chapter 3 the experimental setup is described.

In Chapter 4 the main structural and physical properties of the Ni_3Al and CoAl intermetallic substrates and of the Al-oxide are shortly outlined.

Chapter 5 presents the results obtained for the growth of Co on the $Ni_3Al(100)$ surface. The temperature stability of the cobalt film is also discussed.

In Chapter 6 the oxidation of $Ni_3Al(100)$ surface is presented. The oxidation at 300 K leads to the growth of a thin amorphous Al_2O_3 oxide layer. Oxidation at 1100 K produces a well-ordered Al_2O_3 layer.

Chapter 7 presents the results of Co deposition on the thin Al_2O_3 film grown on the $Ni_3Al(100)$ surface. The thermal stability of the film is also analyzed.

Chapter 8 presents investigations of the oxidation of the CoAl(100) surface.

The thesis ends with a summary in which the most important results are comprised.

Chapter 1

Theoretical background of experimental methods

The growth of thin films trough different methods (oxidation, MBE, etc.) on various substrates is a complex process. In order to understand these processes and to get a better characterization of the films obtained, complementary methods of investigations have to be used. This chapter briefly reviews the four techniques employed in the present work:

- **H**igh **R**esolution **E**lectron **E**nergy **L**oss **S**pectroscopy(**EELS**)
- **A**uger **E**lectron **S**pectroscopy (**AES**)
- **L**ow **E**lectron **E**nergy **D**iffraction (**LEED**)
- **S**canning **T**unneling **M**icroscopy (**STM**)

The first three methods belong to the group of techniques involving the interactions of low energy electrons (1 eV - 10 keV) with the matter. Electrons in this energy range interact with matter strongly. Consequently, their mean free path is of about few atomic layers making them appropriate tools for surface studies. A first requirement for experimental techniques using electrons is ultra-high vacuum

(UHV) condition due to the small mean free path of these particles in the gas phase [11]. This condition meets also another important requirement for surface research, namely the maintenance of a well defined surface, free of contamination for reasonable times.

STM offers the possibility to study the structure and topography of a surface at atomic scale. However, this method gives very limited information about surface chemistry, and the identification of the surface species is not straightforward. This is the reason why additional techniques are used, like EELS and AES, which fulfill this requirement. In the following, the theoretical background of the experimental methods used in the present work will be briefly exposed.

1.1 High Resolution Electron Energy Loss Spectroscopy (EELS)

High Resolution Electron energy loss spectroscopy (EELS) is the study of the vibrational properties of the surface and of the adsorbates on the surface of solids by the analysis of the energy spectrum of low-energy electrons backscattered from it.

The basis of ***EELS*** consists of producing a monoenergetic low energy electron beam, making impact on a surface and determining the energy loss of the scattered electrons.

In order to provide a better understanding of the observed EEL spectra we will give a short description of the phenomena involved in the EELS process.

There are three important ***scattering mechanisms*** involved in EELS.

- The ***dipole scattering*** is a long range effect involving the interaction of the incoming electrons with the dynamic electric dipole induced by vibrations. The incident electrons are scattered while they are still some 100 - 200 Å above the surface. Dipole scattering involves negligible change in the wave vector of the electron thus producing a *"dipole scattering lobe"* sharply centered around

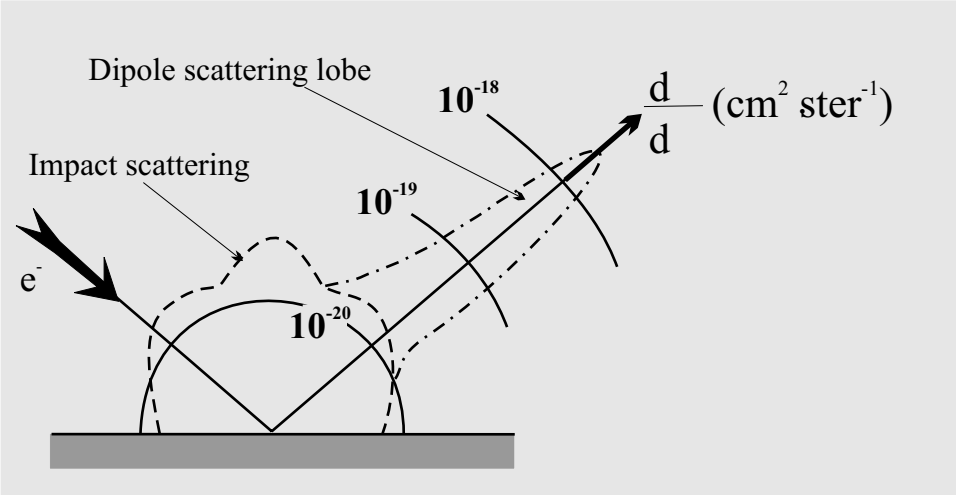

Figure 1.1: The cross-section of dipole scattering and impact scattering.

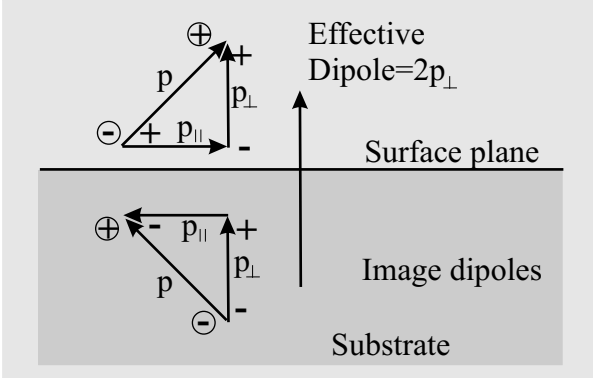

Figure 1.2: The image dipoles on a metallic substrate.

the specular direction (Fig 1.1). The so-called *dipole selection rule* applies for dipole scattering. Only those surface vibrations can be observed which have a component of their dynamic dipole oriented perpendicular to the surface. This can be explained as follows: on a metallic substrate a dipole creates an *image dipole* in the substrate (Fig. 1.2). The parallel component of the true and the image dipole cancel and there is no net polarization field. The perpendicular components of the true and the image dipoles reinforce each other, there is an effective dynamic dipole moment ($2p_\perp$) and scattering does occur. Therefore, for a metallic substrate only vibrations, which belong to the total symmetric

representation of a point group (A_1 and $A^{'}$), can be observed.

- In ***impact scattering***, the incident electrons are scattered by short range interaction with the atomic potential of the lattice. This short-range scattering mechanism gives a broad angular distribution of inelastically scattered electrons (Fig 1.1). This mechanism is not subject to the same selection rule as dipole scattering, i.e. a vibrational mode need not be oriented perpendicular to the surface to be excited. The theoretical description of impact scattering requires detailed knowledge of the electron-surface scattering potential, a problem which is similar to LEED where multiple scattering has to be included.

  Impact and *dipole scattering* mechanisms can be distinguished therefore by measuring the angular distribution of scattered electrons. Impact scattering usually has a much lower cross section than dipole scattering.

- In ***negative ion resonance scattering***, for a certain energy, the incident electrons are temporarily captured by empty electronic energy levels of weakly bound molecules on the surface and a short-lived negative ion appears on the surface. The short-lived negative ion will decay and the electrons are scattered in directions depending on the symmetry of the excited state.

1.1.1 Dielectric theory of inelastic electron scattering

In the present work the growth of thin oxide films on metallic substrates is investigated. Intense losses due to the ionic layers appears in the EEL spectra which are long-wavelength optical surface phonons, so-called Fuchs-Kliewer phonons [12]. In the following a short description of the dielectric theory of inelastic electron scattering is given, which allows a better understanding of the observed EEL spectra and theoretical calculations of the EEL spectra.

The dielectric theory allows the description of electron interaction with dipole fields

at the surface. The electrons are considered as classical particles, while the collective excitation of the medium, such as optical phonons, are described quantum mechanically [13]. The interaction of the electron with the solid can be described in the following manner: The Coulomb field accompanying the moving electron during its approach to the solid interacts with the electrons of the solid material via long-range dipole fields. This interaction creates a space- and time-dependent polarization field which in turn damps the motion of electrons. From classical electrodynamics the energy loss per unit volume is [14, 15]:

$$\mathrm{Re}\left\{2\pi i \int_{-\infty}^{\infty} \omega \mathbf{E}(\omega)\, \mathbf{D}^*(\omega)\, d\omega\right\}. \tag{1.1}$$

where $\mathbf{E}$ is the electric field and $\mathbf{D}$ the electrical displacement.

The classical scattering probability $P_{cl}(\omega)$ for an incident electron inelastically scattered into the energy-loss range between $\hbar\omega$ and $\hbar\omega + d\omega$ and into solid angle spanned by the detector, is given by dipole scattering theory [16]:

$$P_{cl}(\omega) = \frac{e^2}{4\pi\varepsilon_0 \hbar \mathbf{v}_\perp} \frac{2}{\pi^2} \int\int_D \frac{q_\parallel {\mathbf{v}_\perp}^3}{[(\mathbf{q}_\parallel \cdot \mathbf{v}_\parallel - \omega)^2 + (q_\parallel \mathbf{v}_\perp)^2]^2} \,\mathrm{Im}\left\{\mathrm{g}(\mathbf{q},\omega)\right\} d^2q, \tag{1.2}$$

where $\mathbf{v}_\parallel$ and $\mathbf{v}_\perp$ are the electron velocity components parallel and perpendicular to the surface, respectively. The integration includes all wave-vectors which scatter the electron into the acceptance angle of the spectrometer analyzer according to energy and momentum conservation. The scattering probability consist of two factors: the kinematic prefactor and the energy loss function $\mathrm{Im}\left\{\mathrm{g}(\mathbf{q},\omega)\right\}$.

The *kinematic prefactor* predicts strong features in the scattered intensity characterized by a narrow lobe in its angular distribution of with $\theta_0 = \hbar\omega_0/2E_i$. In the case of granzing incidence ($v_\perp \ll v_\parallel$), the pre-factor shows a sharp maxima when $v_\parallel$ equals the phase velocity $\omega/q_\parallel$. This means that when

$$v_\parallel = \frac{\omega}{q_\parallel} \tag{1.3}$$

one has the optimal coupling between the primary electrons and the surface mode [15]. In terms of energy and wave vector $\mathbf{k}$ the condition 1.3 can be expressed

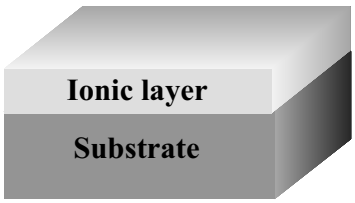

Figure 1.3: The model of a ionic layer supported on a metallic substrate.

as $q_\parallel = k\hbar\omega/2E$. For a primary energy in the range of 10 eV, and excitation around 100 meV, the $q_\parallel$ is smaller than 0.01 Å^{-1}. Such a small wave vector leads to scattering centered in small angles (1 - 2 °) around the specular direction, which is compatible with the acceptance aperture of the electron spectrometers. Thus, the measurement of the angular distribution of the energy losses allows to distinguish dielectric scattering (due to long-range density fluctuation) from other scattering processes.

The dielectric properties of the sample are given by the *imaginary part of the surface loss function,* $\mathrm{g}(\mathbf{q},\omega)$. For semi-infinite isotropic insulator samples $Im[\mathrm{g}(\mathbf{q},\omega)]$ reduces to $Im(-1/(\epsilon(\omega)+1))$. In the general case of a plane-stratified medium or of an anisotropic sample $\epsilon(\omega)$ is replaced by an appropriate effective dielectric function $\xi(\mathbf{q},\omega)$ with $\mathbf{q}$ the wave vector of the surface phonons. For the isotropic model (for which ξ is independent of the angle of $\mathbf{q}$ [13]) of an oxide layer (ϵ_1) on a semi-infinite metallic substrate (ϵ_S), $\xi(\mathbf{q},\omega)$ is given by:

$$\xi(\mathbf{q},\omega) = \epsilon_1(\omega)\frac{\epsilon_1(\omega)\tanh(qd_1) + \epsilon_S(\omega)}{\epsilon_S(\omega)\tanh(qd_1) + \epsilon_1(\omega)} \tag{1.4}$$

The frequency dependence of the dielectric constants $\epsilon_1(\omega)$ and $\epsilon_S(\omega)$ can be expressed as a sum of n Lorentzian oscillator terms:

$$\epsilon(\omega) = \epsilon_\infty + \sum_{k=1}^{n} \frac{S_k\omega_{\mathrm{TO}k}^2}{\omega_{\mathrm{TO}k}^2 - \omega^2 - i\gamma_k\omega} \tag{1.5}$$

where ω_{TOk} denotes transverse-optical phonon frequency with strength S_k, and damping constants γ_k, and ϵ_∞ is the high frequency dielectric constant for $\omega \longrightarrow \infty$ (i.e. the values of $\epsilon(\omega)$ for which $\omega \gg \omega_{TO}$). For the oscillator strength, S_k, the

following relation is fulfilled:

$$\epsilon_0 = \epsilon_\infty + \sum_{k=1}^{n} S_k. \tag{1.6}$$

where ϵ_0 is the value of $\epsilon(\omega)$ for which $\omega \ll \omega_{TO}$.

In certain cases (metal or semiconductors) the experimental results are best reproduced when a Drude contribution:

$$\frac{-\omega_p^2}{\omega^2 + i\gamma\omega} \tag{1.7}$$

is added to the right-hand side of eq. 1.6. In this term ω_p is the bulk plasmon frequency of the charge carriers, and the Ohmic damping frequency γ is the reciprocal value of the free carrier relaxation time τ.

Lambin et al. [17] developed a computer program which allows the calculation of the EEL spectrum of an arbitrary plane-stratified medium for low energy electrons specularly reflected at the surface. A dielectric approximation is used to characterize the response of the target material to the long-range Coulomb field of the impinging electrons. The input parameters $(\omega_{\mathrm{TOk}}, S_k, \epsilon_\infty, \gamma_k, \omega_p)$ are taken from infra-red measurements for the same materials. The parameters of the spectrometer and the incident electron energy are known by the user. The layer thickness is a free input parameter. The comparison of calculated spectra with experimental ones leads to the identification of the surface layer. As the input parameters are, mostly, the bulk values, the application of dielectric theory to very thin films is questionable. This problem has been investigated by Sennet et. al [18] using the *rigid ion approximation*. They carried out lattice-dynamic calculations of the surface loss function associated with optical excitation in an ionic crystal. The calculations were performed for NaF isolated films and NaF slabs on a semi-infinite substrate. It was shown that dielectric theory provides a valid description of the surface energy loss function when the film thickness exceeds 200 Å. For very thin films the dielectric theory fails in producing the correct frequency of the surface energy-loss peaks, but

the intensity of the peaks is more accurately predicted. The dimensions of the Al_2O_3 films presented in this work certainly are verging on the limits of the dielectric theory approximation. However, the agreement between the calculated spectra based on this theory and experimental results is rather good. The description of the loss feature in terms of Fuchs-Kliewer (FK) modes is reasonable since it allows the understanding and interpretation of the spectra in a straightforward way. Neglecting retardation effects (i.e. $c \rightarrow \infty$) the FK modes are solutions of the Maxwell and material equations, for which both $div\mathbf{P} = 0$ and $rot\mathbf{P} = 0$ hold, with $\mathbf{P}$ being the polarization vector [15]. For a semi-infinite insulator the phonons have frequencies ω_{SP} with $\mathrm{Re}\{\epsilon(\omega)\}$ = -1, i.e. $\omega_{TO} \leq \omega_{SP} \leq \omega_{LO}$ (with the dielectric constant $\epsilon(\omega)$; ω_{TO} and ω_{LO} denote the TO and LO phonon frequencies of the bulk modes). If one considers a thin film of an ionic crystal, both surfaces of the film support a FK mode which results in a superposition field within the slab. For $(qa) \rightarrow 0$ (with q the wave vector parallel to the surface and a the slab thickness) the surface phonon splits up into two branches ω_- and ω_+. In the limit $(qa) \rightarrow 0$ (i.e. at vanishing slab thickness or $\lambda \rightarrow \infty$), ω_- approaches ω_{TO} while ω_+ approaches ω_{LO} [19]. If the dielectric layer is supported by a conducting material, as in our case, only the high frequency ω_+ branch is observable. Since the ω_- modes are parallel to the conducting plane, they are screened by free electrons in the metal [12].

1.2 Scanning Tunnelling Microscopy (STM)

In the early 1980's Binning and Rohrer [20] developed a new technique for studying surface structure - Scanning Tunnelling Microscopy (STM). STM is an example of the practical application of a quantum mechanical phenomenon: quantum tunnelling. Quantum mechanical tunnelling involves the penetration of a potential barrier by an electron wave function. The potential barrier is, in our case, the vacuum. In order to quantify the properties of the STM microscopy we must calculate the tunneling current in the framework of a quantum mechanical formalism. The

Fowler-Nordheim formalism applied to the tunneling between two planar electrodes at a distance s gives the following expression:

$$I \propto e^{-A\cdot\sqrt{\varphi}s} \tag{1.8}$$

where A is a constant, and φ is the average work function of the two electrodes.
If one considers a rectangular barrier of height V, the Schrödinger equation is:

$$-(\hbar^2/2m)(\mathrm{d}^2\Psi/\mathrm{d}x^2) = (E-V)\Psi \tag{1.9}$$

The solutions of these equations are of the form $\Psi \propto \mathrm{e}^{\pm kx}$ where $k = \sqrt{\frac{2m}{\hbar^2}(V-E)}$.

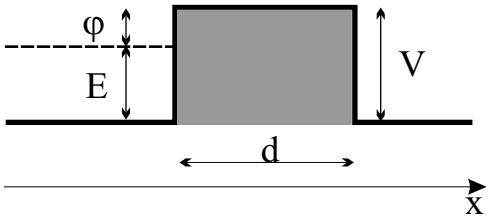

Figure 1.4: Potential barrier scheme for STM.

In the case of V>E the wave function within the barrier is a decreasing exponential and the transmission probability is given by: $|\Psi|^2 \propto \mathrm{e}^{\pm kx}$. The quantity $\varphi = V - E$ is called work function, and the tunnel current which is proportional to the transmission probability, is given by equation 1.8, if one defines A as:

$$A = \frac{2k}{\sqrt{\varphi}} = \frac{4\pi}{h}\cdot\sqrt{2m} = 1.025\cdot\ eV^{-1/2} \quad \text{Å}^{-1} \tag{1.10}$$

taking into account that

$$\varphi = \frac{\varphi_1 + \varphi_2}{2} \tag{1.11}$$

is the average work function of the two electrodes, which amounts to 4 - 5 eV for the most metallic clean surfaces.
If one of the electrodes is the STM tip, the tunneling current, I_T, can be written as

$$I_T \propto \frac{U}{d}\cdot e^{-Ad\sqrt{\phi}} \tag{1.12}$$

where U is the applied voltage between the tip and the sample, ϕ-the average work function and A a constant with a value of 1.025 $Å^{-1}$ $eV^{-1/2}$ for a vacuum gap. I_T is easily measurable for distances d of several tens of Å and, in order to get information about surface, d has to be controlled with a precision of 0.05 - 0.1 Å.

1.2.1 Basic Principles of STM measurements

In STM experiments the tunnelling current is measured between a metallic tip and a conducting substrate which are in very close proximity but not in physical contact. The magnitude of the tunnel current reflects the electronic density of states (DOS) of the surface.

In order to get information on the surface structure at the atomic level, using STM, the position of the tip with respect to the surface must be very accurately controlled (to within about 0.1 Å). The tip must be very sharp - ideally terminating in just a single atom at its closest point to the surface. It is possible to accurately control the relative positions of the tip and the surface by ensuring good vibrational isolation of the microscope and using sensitive piezoelectric positioning devices.

If the tip is biased with respect to the surface, electrons can tunnel, provided the separation of the tip and surface is sufficiently small - this gives rise to a tunnelling current. The direction of the current flow is determined by the polarity of the bias. If the tip potential is negative with respect to the sample, electrons tunnel from occupied states of the tip into unoccupied states of the sample. When the tip potential is positive with respect to the sample, electrons tunnel from occupied states of the sample into unoccupied states of the tip (Fig. 1.5). This is an over-simplistic model of the tunnelling that occurs in STM but it is a useful starting point for understanding how the technique works.

Imaging of the surface topology may then be carried out in one of two ways:

- in the ***constant current mode*** (CCT) - in which the tunnelling current is maintained constant as the tip scans across the surface. This is achieved by

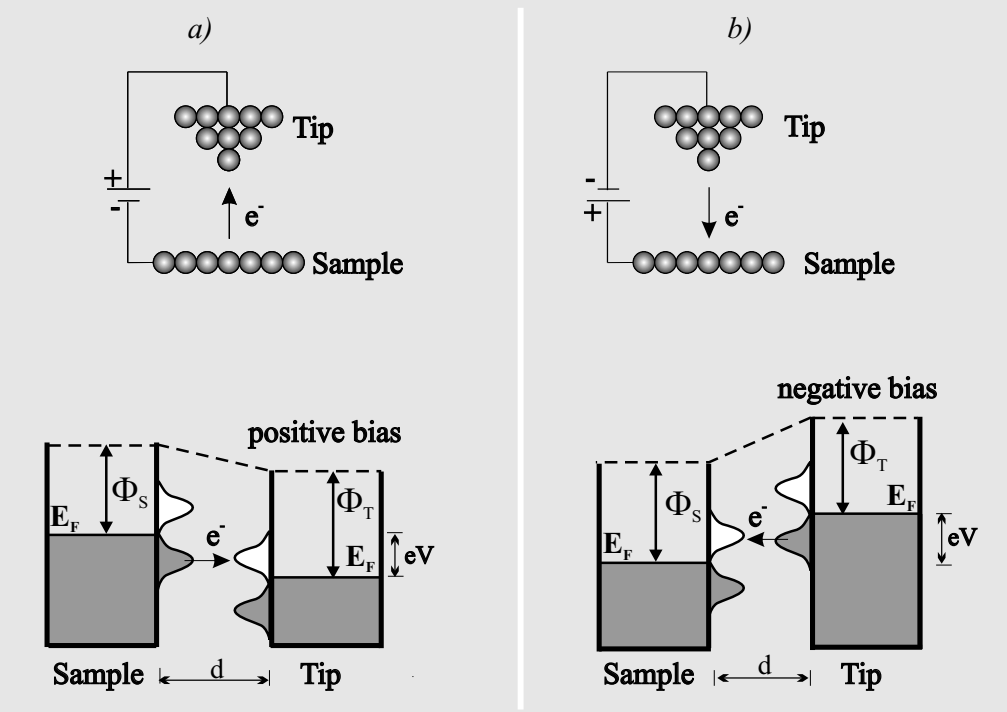

Figure 1.5: Bias dependence of the electron flow in a STM experiment.

adjusting the tip's height above the surface so that the tunnelling current does not vary with the lateral tip position. In this way the tip will move slightly upwards as it passes over a surface atom, and conversely, slightly towards the surface as it passes over a hollow. The image is then formed by plotting the tip height (which is related to the voltage applied to the z-piezo) versus the lateral tip position (Fig 1.6a). This mode is used in our experimental setup.

- in the ***constant height mode*** - in which the tunnelling current is monitored as the tip is scanned, with the same height, parallel to the surface (Fig 1.6b). If the tip is scanned at what is nominally a constant height above the surface, then there is actually a periodic variation in the gap between the tip and the surface atoms. At one point the tip will be directly above a surface atom, and the tunnelling current will be large, while at other points the tip will be above hollow sites on the surface, and the tunnelling current will be much smaller. The computer converts the tunnel current signal into a grey scale plot where

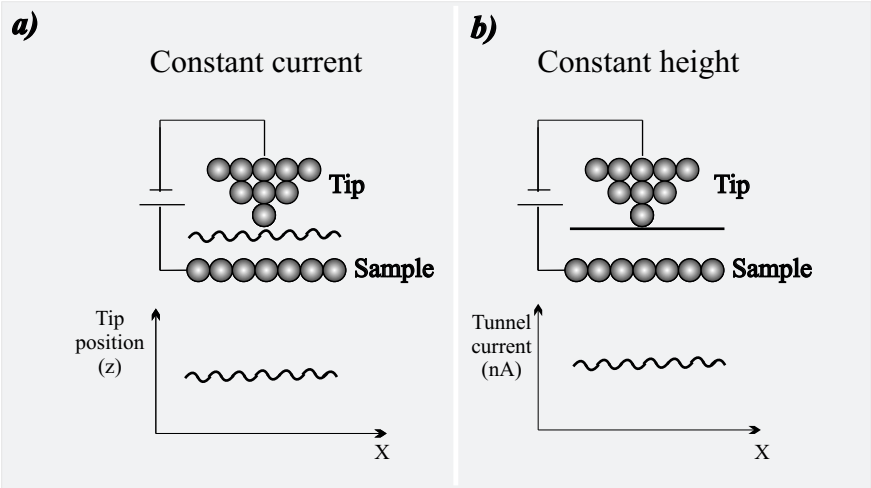

Figure 1.6: Schematic representation of the two scanning modes used in STM.

small currents are represented by dark shades of grey and higher currents by brighter shades.

In both scanning modes the tunnel current variations depend on the variation of the electronic surface state density with position. A plot of the tunnelling current versus tip position therefore shows a periodic variation which matches that of the surface structure - hence it provides a direct picture of the surface (strictly speaking, the image of the spatial variation of the density of electronic states at the surface). Unless the substrate is particularly flat, the constant current mode is essential to prevent the tip from crashing into the surface.

1.3 Auger Electron Spectroscopy (AES)

Auger electron spectroscopy allows identification of the chemical composition of the layers in the vicinity of the surface by ionization of an inner-shell level of the atoms. These holes recombine with electrons from higher energy levels of the sample, which in turn leads to the emission of electrons, the so-called Auger electrons. Auger Electron Spectroscopy (AES) was developed in the late 1960's. The name of the method derives from the name of Pierre Auger, a french physicist, who observed

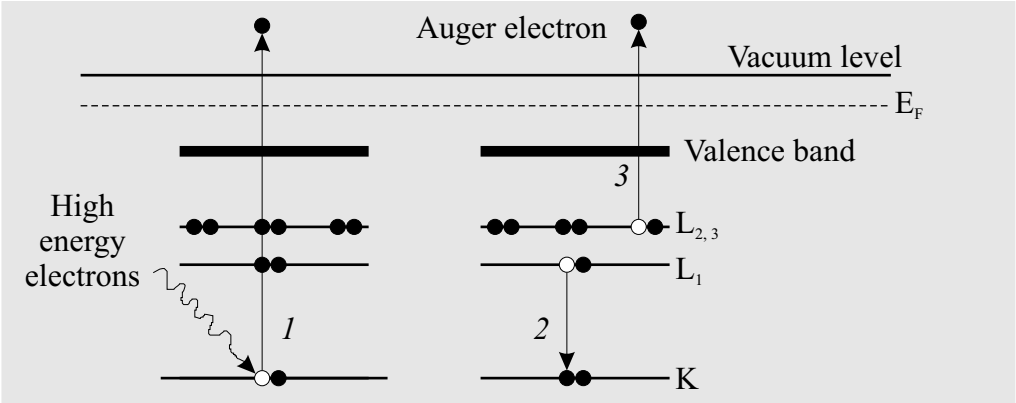

Figure 1.7: AES process.

this effect for the first time in 1920.

AES involves the following steps, shown in Fig 1.7:

1. The ionization of one of the inner-shell electrons (K) of an atom using a high energy primary electron beam (2-10 keV),

2. The occupation of this vacancy by an electron from a higher energy level (L_1) which releases energy corresponding to the difference between the two states,

3. The radiationless transfer of this energy to an electron located on the same or higher level. ($L_{2,3}$), and the emission of this electron.

The kinetic energy of the Auger electron is given by

$$E_{kin} = E_K - E_{L_1} - E_{L_{2,3}} - \Delta E \tag{1.13}$$

The correction term ΔE is used to describe the many-electron effects related to the corresponding rearrangement of the other electrons.

In the solid state, the core levels of atoms are little perturbed and essentially remain as discrete, localized (i.e. atomic-like) levels. The valence levels, however, overlap significantly with those of neighboring atoms generating bands of spatially-delocalised energy levels. As an example, in Fig 1.8, the energetic configuration of Al in various environments is presented. In metallic Al and in Al_2O_3 compounds the

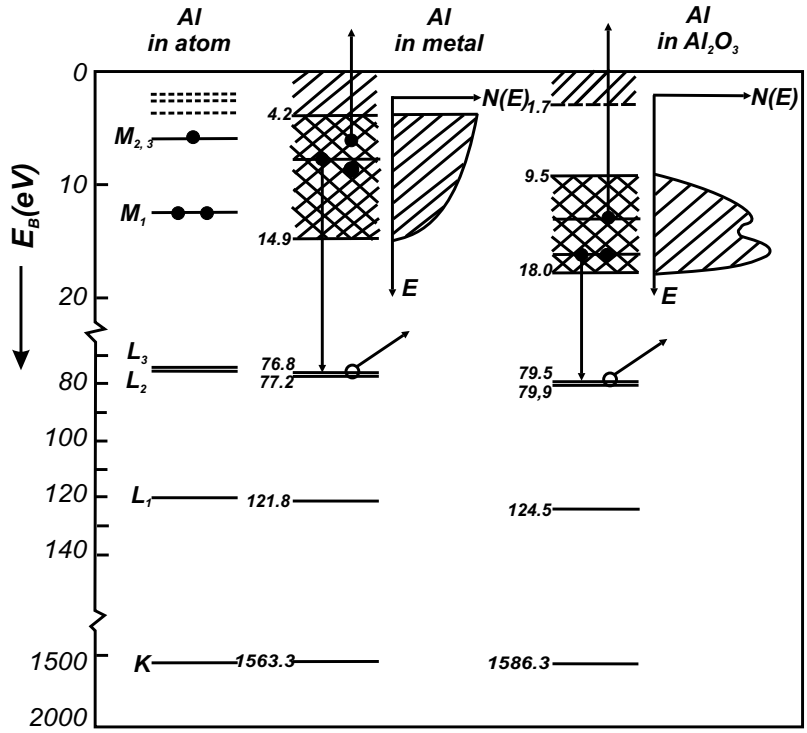

Figure 1.8: Energy-level schemes and density of state of Al in various environments [21].

valence levels overlap forming energy bands depending on the actual composition. Hence, the core levels are slightly shifted. This leads to a shift also in the corresponding AES transitions. Consequently, the energy of AES transitions can give a valuable indication of the environment of the Al atoms.

For a film grown on a substrate the Auger signal allows an estimation of the film thickness. Before leaving the system, the Auger electrons from the substrate atoms have to pass trough the film. Thus, the Auger intensity I signal depends on the inelastic mean free path (IMFP) λ of the electrons and on the thickness of the film. In order to determine the dependence of intensity on the film thickness, the growth mode has to be considered [15]. For layer-by-layer growth the change of the AES intensity is related to the change dh of the film thickness by the relation:

$$\frac{\mathrm{d}I}{I} = -\frac{\mathrm{d}h}{\lambda} \tag{1.14}$$

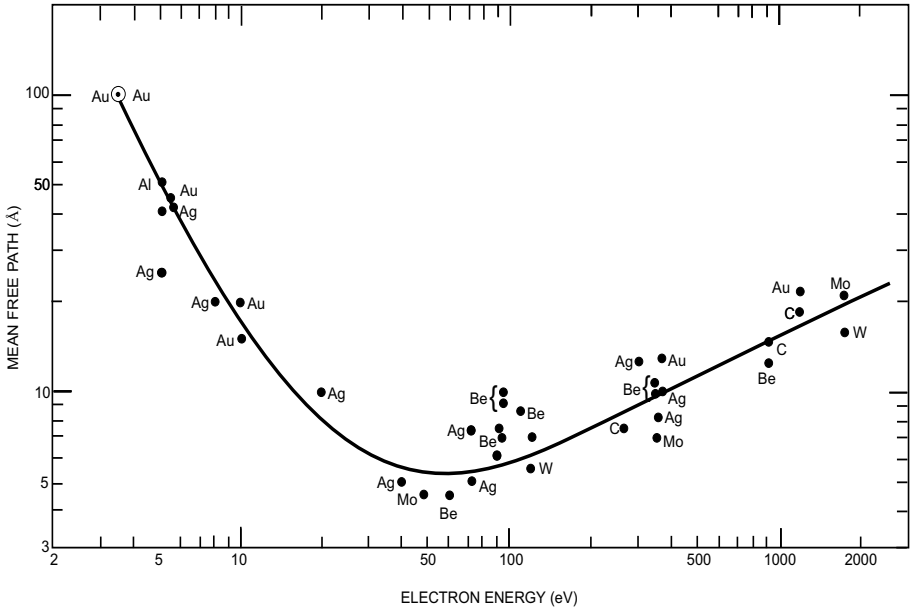

Figure 1.9: "Universal curve" for the inelastic electron mean free path as a function of electron kinetic energy [22].

By integrating this relation between appropriate limits one obtains:

$$\int_{I_0^S}^{I^S} \frac{\mathrm{d}I}{I} = -\int_0^d \frac{\mathrm{d}h}{\lambda} \qquad \Rightarrow \qquad I^S = I_0^S e^{\frac{d}{\lambda}} \tag{1.15}$$

where I_0^S is the intensity of Auger signal of the substrate before deposition and I^S represents the intensity after deposition of a film of thickness d. The mean free path of electrons depends on their energy. Fig. 1.9 shows this dependence, the so-called "universal curve". For electron energies between 50 and 3000 eV, the IMFP of electrons varies from ~ 5 to ~ 25 Å. For elements IMFP depends on the electron energy as [23]:

$$\lambda = \frac{538}{E^2} + 0.41(a \cdot E)^{1/2} \tag{1.16}$$

and for inorganic compounds the relation is:

$$\lambda = \frac{2170}{E^2} + 0.72(a \cdot E)^{1/2} \tag{1.17}$$

where the a parameter is given by:

$$a = \sqrt[3]{\text{volume of an atom}} = \sqrt[3]{\frac{\text{unit cell volume}}{\text{number of atoms per unit cell}}} \tag{1.18}$$

1.4 Low Electron Energy Diffraction (LEED)

Low Electron Energy Diffraction (LEED) is a key technique used in investigation of surfaces structure. The first experiment which showed that the electrons are diffracted by crystalline solids in the same way as X-ray was made by Davisson and Germer in 1927. They observed the first diffraction effect in the electrons backscattered from a nickel single crystal [24]. The LEED technique was developed further by Germer and co-workers [25] in 1960.

Electron diffraction relies on the interference of electron waves elastically scattered from the surface of a crystal. The *de Broglie* wavelength of electrons, λ is given by $\lambda(\text{Å}) = \sqrt{150.4/E}$ where E is measured in eV. Electrons with energy between 10 and 500 eV have wavelengths between 3.9 and 0.54 Å, on the order of interatomic distances in solids. Thus, electrons in this energy range are used to provide information about the surface structure. The diffracted electrons from an ordered surface give an interference pattern, which represents the projection of the surface symmetry in the two-dimensional reciprocal space. These interference pattern will be observed on the screen of LEED optics.

The electrons with wavelength λ diffracted by two scatterers separated by a distance d (Fig. 1.10), give the first maximum of diffraction at an angle where the two diffracted beams are in phase. If the incident angle is θ_0, interference occurs in the direction θ_1, where θ_1 is given by:

$$d(sin\theta_1 - sin\theta_0) = n\lambda \tag{1.19}$$

An arrangement of lattice points which is periodic in two dimensions may be considered as an ensemble of parallel rows of scatterers with directions [h'k'] and mutual distances $d_{h'k'}$. In this case the interference maxima occur in the directions given

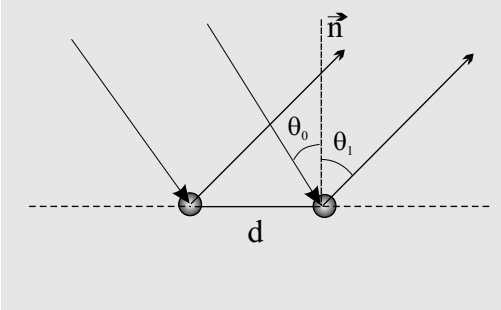

Figure 1.10: Diffraction process on two scatterers separated by a distance d

by:

$$d_{h'k'}(sin\theta_1 - sin\theta_0) = n\lambda \tag{1.20}$$

For normal incidence (θ_0=0) the equation simplifies to:

$$n\lambda = d_{h'k'}sin\theta_1 \tag{1.21}$$

In the case of diffraction by a two-dimensional surface only two Laue equations are considered:

$$\vec{a}_i(\vec{k}_f - \vec{k}_i) = \vec{a}_i \cdot \vec{K} = 2\pi n_i, \quad i = 1, 2 \tag{1.22}$$

where $\vec{a}_i$ are the primitive translation vectors of the surface lattice, $\vec{k}_i$ and $\vec{k}_f$ are the wave vectors of the incident and diffracted electrons, $\vec{K}$ ($\vec{K} = \vec{K}_\parallel + \vec{K}_\perp$) the scattering vector and n_i are integers. The reciprocal lattice is defined by:

$$\vec{a}_i \cdot \vec{a}_j^* = 2\pi\delta_{ij} \quad i = 1, 2 \qquad \delta_{ij} - \text{the Kronecker symbol} \tag{1.23}$$

where $\vec{a}_j^*$ are the basis vectors of the reciprocal lattice. The condition for occurrence of Bragg spots is given by:

$$\vec{K}_\parallel = \vec{k}_{f,\parallel} - \vec{k}_{i,\parallel} = \vec{G}_\parallel \tag{1.24}$$

where $\vec{G}_\parallel$ is a vector of the 2D surface reciprocal lattice, and

$$\vec{K}_\parallel = m_1 \cdot \vec{a}_1^* + m_2 \cdot \vec{a}_2^* \qquad m_1, m_2 \quad \text{integers} \tag{1.25}$$

where $\vec{K}_\parallel$ is the parallel component of the scattering vector.

Therefore, a diffraction spot (Bragg reflex) will be observed only when the component of the scattering vector parallel to the surface ($\vec{K}_{\parallel}$) is equal to a vector of the surface reciprocal lattice.

These are the Laue conditions for diffraction on a two-dimensional lattice. The interference structure observed on the screen of LEED optics represents the transformation of the translational symmetry of the surface structure into reciprocal space. The analysis of the LEED pattern allows the determination of the reciprocal lattice vectors $\vec{a}_1^*$ and $\vec{a}_2^*$ and, by transformation into real space (eq. 1.23), the basis vectors of the surface unit cell are found.

In a real LEED experiment the electrons penetrate several atomic layers into the solid. As they penetrate deeper, multiple scattering events in the z direction perpendicular to the surface contribute to the LEED pattern, and the third Laue condition becomes more important. This leads to a modulation of the intensities of the Bragg reflections as a function of electron energy. Thus, the LEED I-V curves contain additional information on the structure perpendicular to the surface.

Surface reconstruction or gas adsorption on a surface usually result in a change in the diffraction pattern corresponding to the appearance of a new surface periodicity. The relation between the adsorbate reciprocal lattice vectors ($\vec{b}_1^*$, $\vec{b}_2^*$) and those of the substrate ($\vec{a}_1^*$, $\vec{a}_2^*$) are given by:

$$\begin{pmatrix} \vec{b}_1^* \\ \vec{b}_2^* \end{pmatrix} = \begin{pmatrix} m_{11}^* & m_{12}^* \\ m_{21}^* & m_{22}^* \end{pmatrix} \begin{pmatrix} \vec{a}_1^* \\ \vec{a}_2^* \end{pmatrix} \tag{1.26}$$

In real space, the adsorbate vectors are related to the substrate vectors by the relation:

$$\begin{pmatrix} \vec{b}_1 \\ \vec{b}_2 \end{pmatrix} = \begin{pmatrix} m_{11} & m_{12} \\ m_{21} & m_{22} \end{pmatrix} \begin{pmatrix} \vec{a}_1 \\ \vec{a}_2 \end{pmatrix} \tag{1.27}$$

The coefficients of the two matrices are related by the following equations:

$$m_{11} = \frac{m^*_{22}}{m^*_{11}m^*_{21} - m^*_{21}m^*_{12}} \tag{1.28}$$

$$m_{12} = \frac{-m^*_{21}}{m^*_{11}m^*_{21} - m^*_{21}m^*_{12}} \tag{1.29}$$

$$m_{21} = \frac{-m^*_{12}}{m^*_{11}m^*_{21} - m^*_{21}m^*_{12}} \tag{1.30}$$

$$m_{22} = \frac{m^*_{11}}{m^*_{11}m^*_{21} - m^*_{21}m^*_{12}} \tag{1.31}$$

so that when the ones of matrix are known the others may be readily calculated. In LEED experiments the matrix relating the reciprocal vectors is determined by analyzing the pattern and then transformed in order to give the matrix which relates the vectors in real space.

In addition to the matrix notation another system originally proposed by Wood [26] is also used. In Wood's notation the adsorbate unit cell is related to that of the substrate by scale factors n and m, where $|\vec{b}_1| = n \cdot |\vec{a}_1|$ and $|\vec{b}_2| = m \cdot |\vec{a}_2|$. Whereas the matrix system can be applied to any system, the Wood notation can only be used if the angle between the adsorbates and the substrate vectors is the same. In this case the surface structure is labeled using the general form $p(n \times m)\mathrm{R}\Phi^0$ or $c(n \times m)\mathrm{R}\Phi^0$ depending on whether the unit cell is primitive or centered. $\mathrm{R}\Phi^0$ indicates a rotation of the adsorbate unit cell by an angle Φ^0 with respect to the substrate unit cell. For Φ^0=0, $\mathrm{R}\Phi^0$ is omitted and so the surface structure of the adsorbate is labeled $p(n \times m)$ or simply $(n \times m)$.

Chapter 2

Growth processes

One of the classical methods of preparing a clean metal surface in UHV is evaporation and condensation of thin films. Materials with a high melting temperature are most conveniently evaporated by electron bombardment. Depending on the surface and on the evaporation conditions, sublimed films can be polycrystalline or monocrystalline.

2.1 Thermodynamics of growth

The thermodynamic classification of growth modes was first addressed by Bauer [27]. He divides the film morphology into three classes determined by the balance of interfacial and surface free energies. Bauer's criterion, the so-called *wetting* condition, is given by [28]:

$$\Delta\gamma \ = \gamma_f + \gamma_i - \gamma_s \tag{2.1}$$

where γ_f, γ_s and γ_i are the surface free energies of the film, of the substrate, and of the film-substrate interface, respectively. Eq. 2.1 gives a formal distinction of the three growth modes depending on the sign of $\Delta\gamma$. The first mode is called Frank-van der Merwe (FM) [29] or two-dimensional (2D) growth (see Fig. 2.1). In this mode, each layer tends to be completed before a new layer begins to grow on top

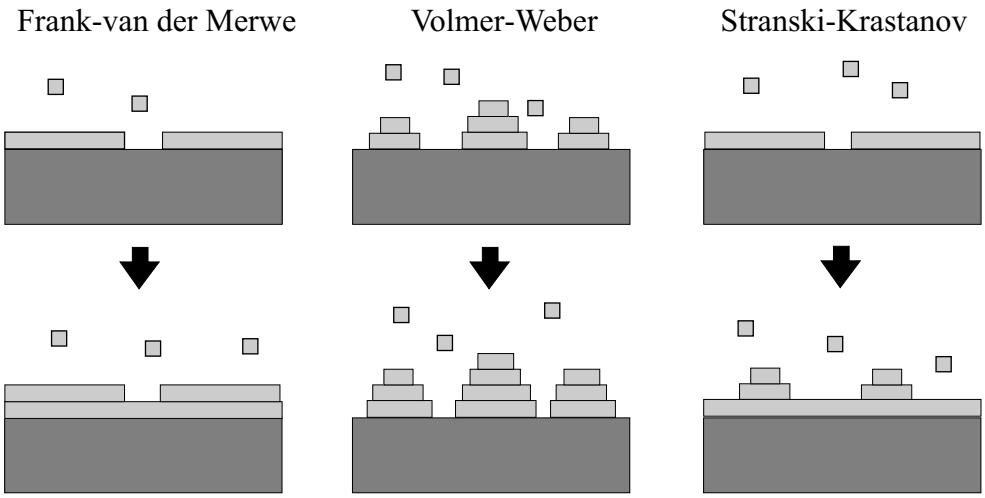

Figure 2.1: Schematic representation of the three thermodynamic growth modes.

of it. For this reason the FM mode is also called *layer-by-layer* growth. In terms of static thermodynamics, it occurs when $\Delta\gamma \leq 0$, i.e. "wetting" of the surface by the deposited film takes place. The opposite case is called the Volmer-Weber (VW) [30] or three-dimensional (3D) growth (see Fig. 2.1). In this mode, several crystal layers grow simultaneously, which causes hillocks and cavities to form on the surface. In this case the "wetting" condition is no longer fulfilled ($\Delta\gamma \geq 0$). The third, intermediate mode arises if the first few monolayers satisfy the layer-by-layer condition and the VW condition applies to all subsequent layers. This is called the Stranski-Krastanov [31] mode (Fig. 2.1). This situation arises only in heteroepitaxy if a lattice mismatch between the substrate and the deposit causes the growing layers to be strained. In such a case, it is often energetically favorable for the first few layers to grow in the layer-by-layer fashion, but after that, the strain is relieved more efficiently by the 3D mode.

2.2 Kinetics of atomic processes

In the kinetic picture, based on atomistic models, the growth mode is a complex balance of many competing processes, which are sketched schematically in figure 2.2. The film morphology, as the outcome of this competition, is strongly influenced by the experimental conditions, i.e. the surface temperature and symmetry, the flux of adatoms impinging on the surface (deposition rate) and the choice of material. Each of the atomic processes is characterized by an activation energy and a prefactor. At a given temperature and deposition rate certain processes might be kinetically inhibited, whereas others are rate determined. Arrhenius-type exponential laws describe mathematically these activated processes. The basic atomic processes taking place

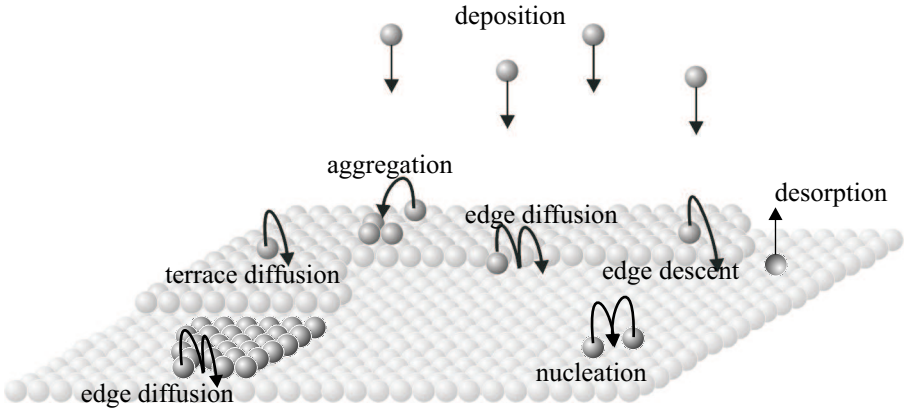

Figure 2.2: Atomic processes in the kinetics of 2-D film growth

during growth are: *deposition*, *surface diffusion* and *desorption*. A process competing with the deposition is the desorption. The desorption probability depends on two factors, the energy barrier E_D necessary for the atom to overcome in order to leave the surface and the temperature T. The average time an atom remains on the surface follows an Arrhenius-type of law:

$$\tau = -\tau_0 \cdot e^{E_D/k_B T} \tag{2.2}$$

where the pre-factor τ_0 is of the order 10^{-14} s and k_B is the Boltzmann constant.

The desorption rate increases if the temperature is increased, eventually reaching a point where the surface atoms begin to evaporate. Under MBE growth conditions that produce quality crystals, the desorption frequency is usually very low compared to the deposition rate, and it can therefore be treated as negligible [32].

The adatoms move on the surface by diffusion events, such as terrace-, interlayer and edge-diffusion [33]. These atomic events are thermally activated and their rates depend on the local surroundings and can usually be described by Boltzmann statistics. Once adsorbed, the atoms move across the surface depending on their diffusion coefficient:

$$D = \frac{1}{4}(\nu_0 \cdot a^2) \cdot e^{-\varepsilon_{Diff}/k_B T} \tag{2.3}$$

where ν_0 is the prefactor, a is the distance between two adjacent sites and ε_{Diff} is the activation energy for diffusion.

If defects are present on the surface, the adatoms may be trapped at these sites forming nuclei for subsequent growth process, which is called heterogeneous nucleation. The other case is homogeneous nucleation where a stable nucleus is generated by aggregation of several (at least two) adatoms on regular sites. The minimum number of atoms (that a single diffusing atom must find for this process) is called *critical cluster size*. By addition of further adatoms, these nuclei will then grow. In contrast, islands up to that size can dissolve again.

When an adatom, wandering on a terrace, reaches a descending step, it encounters an additional energy barrier for hopping down the step known as the Erlich-Schwoebel (ES) barrier [32]. This is due to the fact that the adatom is more weakly bound to the substrate atoms when it is at the upper step edge. A modification to this picture has also been proposed. In this model, there is also a barrier for hopping upwards and the descending step barrier is encountered slightly before the adatom reaches the actual edge. The edge, therefore, acts reflectively towards atoms approaching from above. This effect is also known as diffusion bias.

In far-from-equilibrium growth the growth mode usually changes from 3D growth at low temperatures to layer-by-layer at higher temperatures. At low temperatures the

local energy barriers at step edges prevent the surface adatoms from jumping down a step. At higher temperatures the surface adatoms become so mobile that they can overcome these barriers and the film grows according to the two-dimensional mode. Larger lattice mismatches generally favor island-like growth, and higher deposition rates, on the other hand, lead to a greater tendency towards layer-like growth. Under certain conditions, when the adatoms are mobile but the barriers at step edges suppress the inter-layer transport, the growth results in the creation of large, ordered, pyramid-like formations on the surface. This is called the unstable MBE growth mode. It was first detected by Villain in 1991 [34].

2.3 Oxidation Processes

In this section the oxidation of single crystal surfaces and the formation of well-ordered oxide is briefly presented. An oxide surface can be prepared from bulk samples by cutting a crystallographic plane mechanically or by spark erosion and then polishing the surface [35]. Other methods of preparation of oxide surface are based on the growth of thin films on metallic substrates or metallic alloy surfaces [1]. The crystallographic structure of the substrate then determines to a large extent the structure of the oxide film [36]. The structural quality of the oxide film depends very strongly on the relation between the lattice constants of the metallic substrate and the oxide film, and on the temperature. Oxide films can be grown via oxidation of a metal or via oxidation of a metal deposited on an inert metallic substrate. The lattice constant of the inert substrate has to be chosen properly in order to prepare a less strained oxide layer with long-range order. A third procedure is based on the oxidation of alloy surfaces. Most of the recent studies were performed by oxidation of surfaces of binary intermetallic alloys like NiAl [37, 38, 39], FeAl [40] and CoGa [41, 41]. The oxide layers grow after adsorption of oxygen and the preferential segregation of one of the metallic components (Al, Ga) at the surface. In general, adsorption of oxygen at room temperature leads to the formation of

amorphous oxide layers. Subsequent annealing to elevated temperatures or direct oxidation at elevated temperature leads to thin well-ordered (crystalline) films. One of the advantages of using alloys as substrate instead of pure metals is, that higher annealing temperatures can be used for ordering of the oxide films without melting of the substrate. If there is a large mismatch between the alloy surface and the oxide lattice constants, the film may be defect rich.

In general, an *oxidation* process is the reaction of a metal (or a semiconductor) with a nonmetal (chalcogenide, halogen, water or a combination) to produce a compound on the surface of the metal [42]. The reactants, a metal or semiconductor having delocalized bonds and a gas having covalent bonds, are converted into a product, an oxide having partially ionic, partially covalent bonding. When the product of the reaction is a solid, it separates the two reactants. Further growth requires that a species of metal and/or oxidant dissolve in and move through the growing oxide (see figure 2.3a). In figure 2.3a the substrate consists in a binary alloy (small

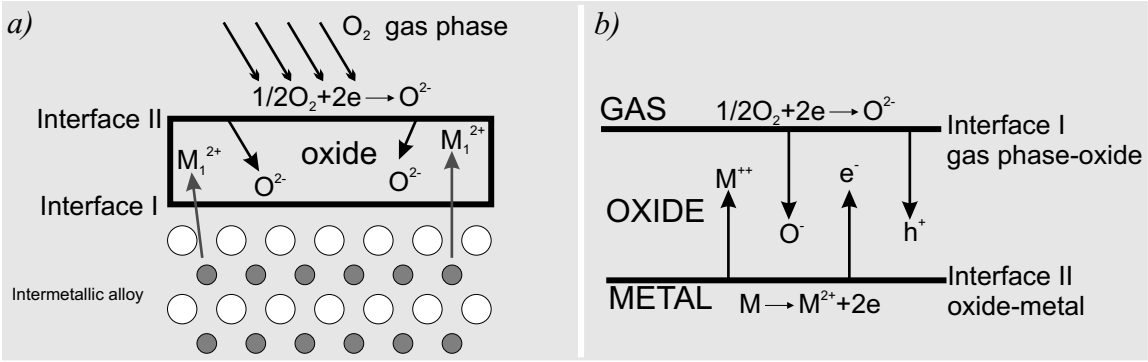

Figure 2.3: (a)Schematic representation of oxide growth on the gas-phase-oxide (I) or oxide-metal (II) interfaces; (b)Transport of ions, electrons and holes across a growing oxide film [1].

and large circles represent the two different atoms). During oxidation one of the metallic constituents moves from the substrate to the interfaces I or II and reacts

with oxygen. Oxygen ions can also move to the interface I to form an oxide. In general, it is often assumed that oxygen is in an ionic state but there is evidence that, at least in the case of silicon oxidation, the migrating species can be molecular oxygen [42]. Charge neutrality during passage of a single ionic species is achieved by the movement of electrons or holes through the oxide in the same or the opposite direction (Fig. 2.3b). Wagner's theory [43] shows that the growth of the oxide films obey a parabolic time dependence:

$$x^2 = k_p \cdot t \tag{2.4}$$

where x is the film thickness and k_p is the parabolic rate constant. Wagner's theory is based upon diffusion across the film being the slowest, and therefore, the rate-limiting step in the overall sequence of reactions. The electric field developed during film growth can be regarded as arising from ambipolar diffusion in the oxide. For example, suppose that metal ions are more mobile in the oxide than are oxygen ions, so that new oxide is formed at the oxide/oxygen interface. In general, electrons have a higher mobility than metal ions and therefore, an electric field will develop to speed up the ions and slow down the electrons until the electric currents carried by the two types of charged particles are equal. Thus, the oxide/gas interface develops a negative electrical potential with respect to the oxide/metal interface. The same is true if the film grows mainly by diffusion of oxygen ions. Wagner's theory assumes that there is no net electric current flowing across the whole film, so that local chemical equilibrium exists throughout the film and that there is no divergence in the ionic and electronic currents. Cabrera and Mott [44], in a general treatment of oxidation, also derived a parabolic rate law for oxidation limited by cation diffusion in the bulk oxide:

$$x^2 = 4\Omega D n_c t \tag{2.5}$$

where Ω is the oxide volume per metal ion, n_c is the concentration of ions at the metal-oxide interface, and D is the diffusion coefficient of ions. The concentration of metal ions at the gas-oxide interface was assumed to be zero. In the original

Cabrera-Mott theory for low-temperature oxidation it was assumed that the adsorbed oxygen produces electronic trap sites at the oxide-oxygen interface and that the electrons can freely pass through the oxide layer to populate these sites. This may occur, for example, by tunneling, impurity conduction, or Schottky emission into the conduction band of the oxide.

Chapter 3

Experimental setup

3.1 The UHV system

Ultra high vacuum (UHV) is of the utmost importance to achieve cleanliness of a sample surface and for an accurate surface characterization. In our system, the UHV is maintained by a combination of a 340 l/s turbomolecular-pump with magnetic bearing (LEYBOLD TMP340), a 200 l/s ion getter pump (LEYBOLD IZ270) and a titanium sublimation pump. The titanium sublimation pump is surrounded by a cryoshield which can be filled with liquid nitrogen. In order to achieve the UHV conditions the whole system is baked-out for 48 hours to a temperature between 150 to 170 °C. The temperature close to the STM must not exceed 150°C. The sample is fixed on a xyz and rotational (FISONS OMNIAX) manipulator, with heating facilities, liquid-nitrogen cooling and a thermocouple (W3%-Re25%). The manipulator ensures the sample displacement among the four main analysis techniques (STM, AES, LEED, EELS) as well as in the front of an evaporator and an ion sputter gun. A photo of the UHV chamber is showed in the figure 3.1.

The chamber consists of three main levels which are referred in Fig. 3.1 as planes. The STM (Besocke-type) and the cobalt evaporator are located in the first plane. The STM can be approached to the sample by using a small (FISONS) manipulator

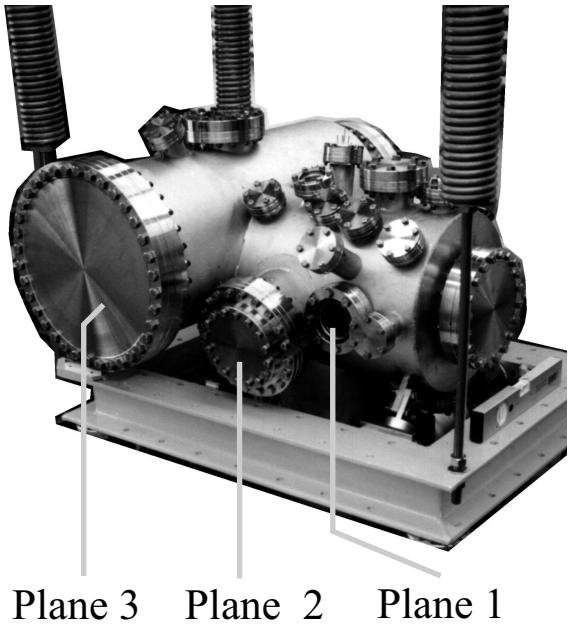

Figure 3.1: UHV chamber

or can be retracted to the upper side of the chamber when the sample has to be moved to another position. The second plane contains a three grid LEED optics (FISONS RV900) and a Cylindrical Mirror Analyzer (CMA) for AES. In the same plane, at the upper part of the chamber a quadrupole mass spectrometer is located, with which the residual gas is monitored. The mass spectrometer can also be used for Thermal Desorption Spectroscopy (TDS). The CMA, the LEED optics and the mass spectrometer can be displaced by linear translations to the appropriate positions close to the sample for specific measurements. In the third plane the EEL spectrometer is located.

An independent UHV gas line is linked to the main chamber. Gases can be admitted close to the sample surface via a capillary doser or by backfilling the chamber. Exposures vary typically from 0,05 L to 1000 L (1 L = 1 Langmuir = 10^{-6} mbar·s).

For the growth experiments an evaporator was attached to the UHV chamber. Cobalt is evaporated from a high purity rod mounted in an OMICRON EFM 3

evaporator (Evaporator with Integral Flux Monitor). A standard cleaning procedure of cobalt was used before evaporation. The evaporation proceeds by electron bombardment of the cobalt rod ($I_{emission} \approx 6mA$, U≈1 kV). The beam exit column contains an ion collector which serves as flux monitor. At a given electron emission current and acceleration voltage the ion flux is directly proportional to the flow of evaporated particles (neutrals). The evaporator was calibrated with a quartz microbalance. The amount of evaporated material determined by the quartz microbalance is given as a *nominal* film thickness in Å. The *effective* thickness of the film is determined by AES.

During the STM experiments all mechanical pumps are switched off in order to avoid vibrations and the whole apparatus is suspended by four springs fixed on the ceiling. The vacuum is maintained only by the ion-pump.

3.2 The EEL spectrometer

The EEL spectrometer is a state-of-the-art instrument developed by Ibach and coworkers [45]. Fig. 3.2 shows a schematic drawing of a double pass EEL spectrometer (HIB 1000).

The electron gun employs a repeller geometry with a LaB_6 cathode. The monochromators and analyzers are electrostatic selection units based on 127° capacitors. All the electron-optical elements (emission system, lenses, monochromators and analyzers) are optimized by numerical simulations. A detailed description of the spectrometer and the numerical simulations is found in Ref. [45]. The thermally emitted electrons are focused by the lenses A_1, A_2 and A_3 into the entrance slit of the premonochromator. After passing the two monochromators the electrons are focused by the lenses B_1 and B_2 on the sample which, together with the scattering chamber, are biased to the desired voltage to get the right primary energy. The scattered electrons, are decelerated to the pass energy of the analyzer and focused by the lenses B_3 and B_4 into the entrance slit of the first analyzer. The scattered electrons which

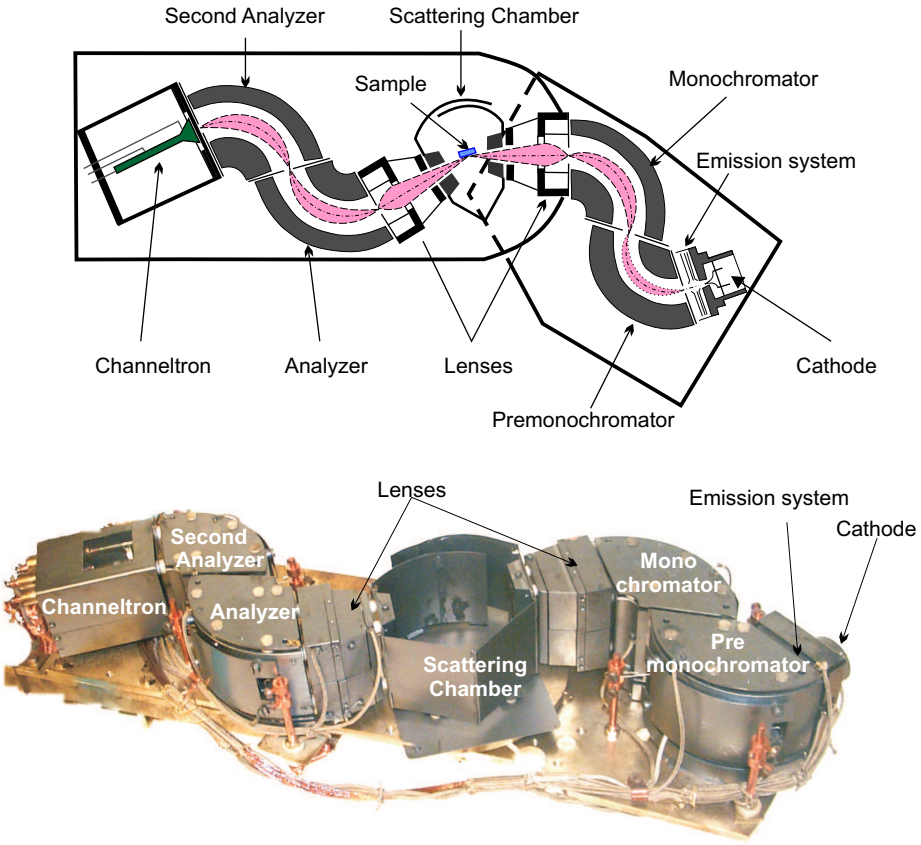

Figure 3.2: Schematic drawing of the EEL Spectrometer.

have suffered an energy loss (gain) are accelerated (decelerated) to the pass energy of the analyzer by an appropriate biasing of the all potentials on the analyzer site. The electrons are measured (counting mode) by a channeltron mounted at the exit of the second analyzer.

The spectrometer can be operated in two different modes. The first operation mode is dedicated to the measurement of surface vibration modes whose frequencies are $\leq$ 500 meV. In the dipole scattering regime the spectra are recorded in specular geometry at an incidence angle of 60° and a primary energy of incident electrons between 1 and 5 eV. The second operation mode of the spectrometer is devoted to the measurement of electronic transitions (band-gap, surface states etc.) with energy losses up to 10 eV.

3.3 The scanning tunneling microscope

The STM used in our experiments is a Besocke-type [46]. This is a modified version of the Beetle type STM that is turned upside down. A schematic drawing of our STM is shown in figure 3.3. The STM consists of four piezos, one inner piezo and

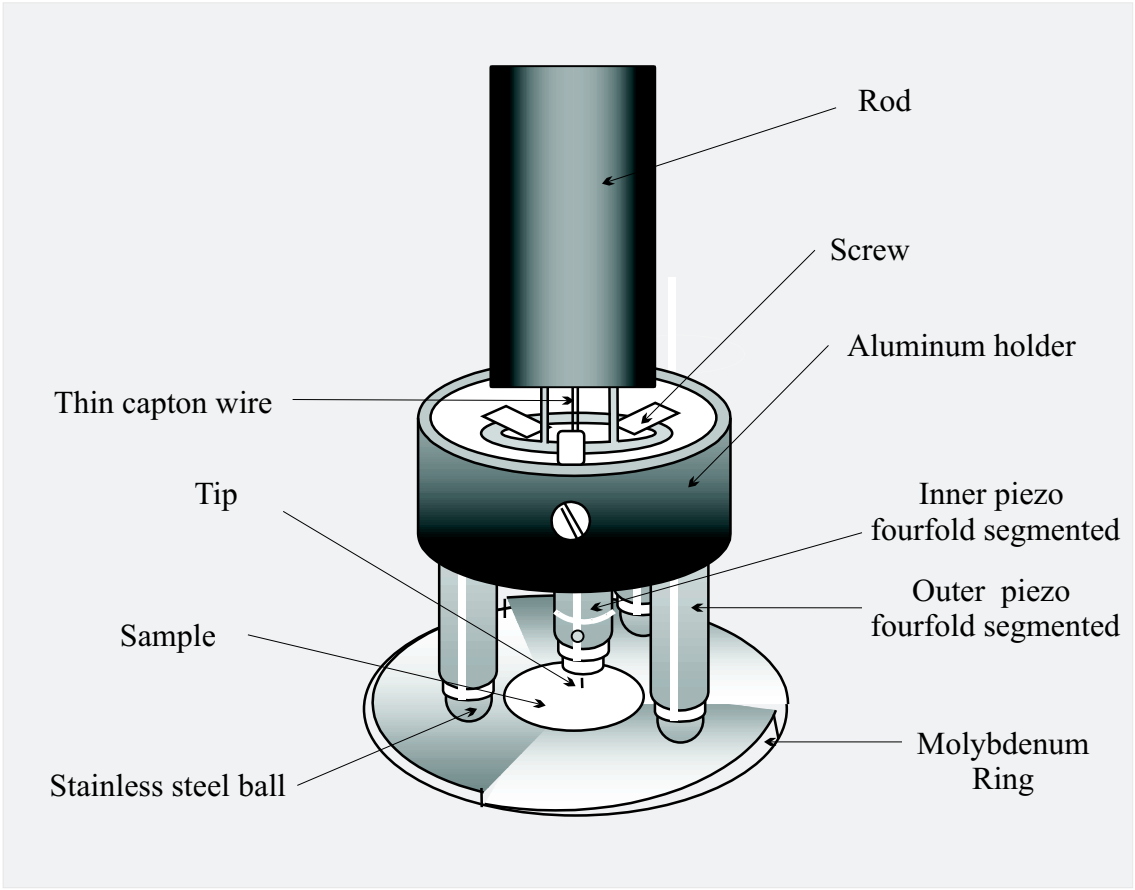

Figure 3.3: Schematic drawing of the STM.

three outer piezos. The piezos were glued to an aluminum disc using a low outgas conducting epoxy. Stainless steel balls were glued to the outer piezos, also with the conducting silver glue. As tip holder a syringe tube was used which was glued in an insulating Macor block. The Macor block was glued to the inner piezo. For both connections an insulating epoxy was used. For the wiring of the electrodes, kapton

coated copper wire with a diameter of 0.04 mm was used. The ring on which the STM is lowered, is made of molybdenum. To prevent the STM (the stainless steel balls) from sticking to the ring, the ring's surface was coated with a thin layer of Tinalox, a titanium aluminum oxide compound. The STM hangs by three screws in a rod which is fixed on the z-translator of the manipulator. By moving the Z-translator of the manipulator up and down (Fig. 3.3) the STM can be put on and picked up from the Mo-ring.

The outer electrodes of the outer piezos are fourfold segmented and used for the rough approach and for scanning. The outer electrode of the inner piezo is also fourfold segmented. It can be used not only as z-piezo, but also for scanning. The Mo ring on which the STM is lowered, has three ramps. By applying the appropriate voltages on the three outer piezos, the STM rotates and moves down or up on the ramps of the ring. The height difference between the highest and the lowest point of the slopes is 0.5 mm. The STM tip on the inner piezo has to be mounted in such a way, that scanning in possible within this range. This is made ex-situ using an optical microscope. The fine approach is performed by the lower non-segmented part of the inner piezo. Scans can be taken both by the inner piezo as well as the outer piezos. The x, y calibration of the STM is performed with atomic resolved images of a graphite surface. In the z direction the calibration was performed using a gold sample. The gold surface has atomic steps of well-known height (2.88 Å). A tungsten tip was used for the measurements in UHV. The tip was prepared by electrochemical etching of a 0.25 mm tungsten wire with 5 molar NaOH. A platinum-iridium tip was used for the measurements on graphite in air. This tip was made by mechanical polishing of a 0.25 mm platinum-iridium (25% Ir) wire.

The shielding of the wire, which carries the tunnelling current, needs special care to prevent cross-talk to the scan signals. The grounded inner electrode of the inner piezo shields the wire. Then, the wire is shielded by the stainless steel tube. Finally the tunnelling signal is carried by a shielded kapton coated copper wire.

3.4 The AES spectrometer

The AES used in our experiments is an OMICRON version using a cylindrical mirror analyzer (CMA 100). The experimental arrangement of the AES is given in figure 3.4. Primary electrons are produced by an electron gun (OMICRON EKI25) which

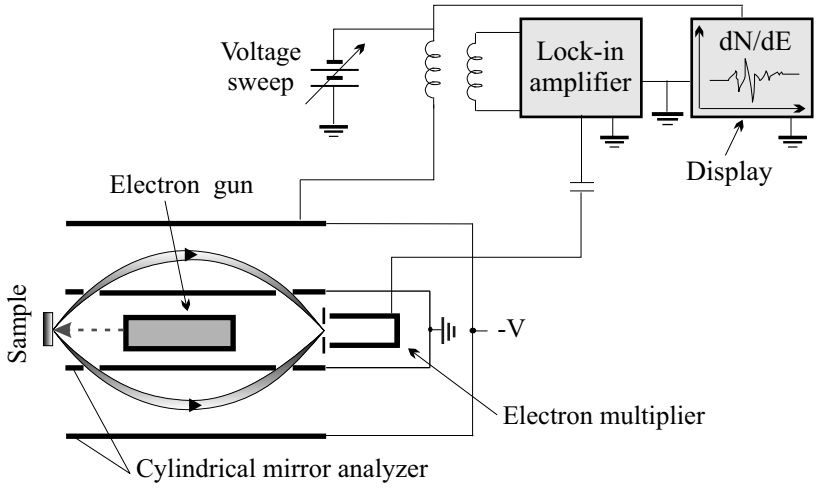

Figure 3.4: AES spectrometer

is integrated into the CMA on its central axis. A beam current of 50 μA is obtained for a filament current of $\approx$ 2.3 A at a high-voltage of 3 keV. The primary electrons make impact on the sample surface. Some of the backscattered electrons and the emitted Auger electrons pass through the aperture of the inner cylinder of the CMA and are filtered as a function of their energy and detected by a Channeltron.

Because of the small Auger signals, AES spectra are measured in the derivative mode to suppress the large background of the true secondary electrons. The differentiation is performed by superimposing a small alternating voltage $V = V_0 \sin\omega t$ on the outer cylinder voltage V and synchronously detecting the *in-phase* signal from the electron multiplier with a lock-in amplifier. On the basis of this detection mode, the energies of the Auger transitions are usually given in the reference work as the position of the minimum of the derivative spectrum dN(E)/dE [47].

3.5 The three grid LEED optics

The LEED apparatus used in our experiments is a three mesh optics version (FISONS RV900). A schematic representation is shown in Fig. 3.5.

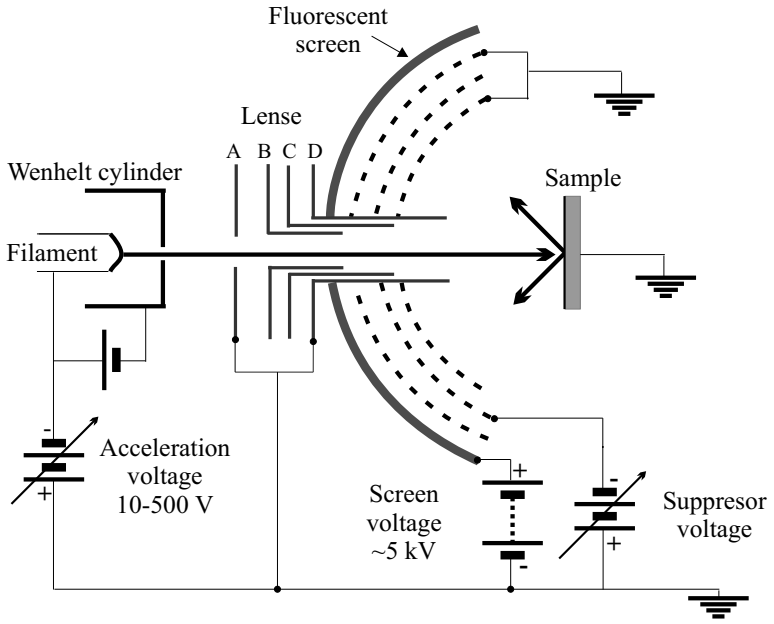

Figure 3.5: Schematic of a three-grid LEED optics [15].

Electrons are emitted by the heated filament (Thoria coated) and collimated by the Wehnelt cylinder which has a small negative bias with respect to the filament. The primary energy (10-500 eV) is determined by the acceleration voltage i.e. the voltage between the filament and the sample. The lenses B and C are used to focus the electron beam. The incident electrons are diffracted by the sample and are backscattered to the fluorescent screen. The screen is at a high positive potential with respect to the sample. The apertures A and D, the grids in front of the fluorescent screen and in front of the sample are grounded. Thus, a field free region between the sample and the screen exists. This is important to prevent electrostatic deflection of the electrons. Besides elastic scattering, inelastic scattering also occurs at the sample surface and on the grid in front of the sample, thus giving rise to electrons of lower energy. These electrons produce a relatively homogeneous

background illumination of the screen. This background is suppressed by applying a somewhat negative potential to the middle grid.

Chapter 4

Structural and physical properties of the involved materials

4.1 Aluminum oxide

One of the purposes of this work was to study the oxidation of the (100) surface of Ni_3Al and CoAl. In both cases thin aluminum oxide films are formed on the surface. The structure of films depends on the preparation conditions. In this section the properties of some Al-oxides are presented.

Al_2O_3 has at least 14 phases. The purest and the most stable is α-Al_2O_3 (Corundum). Most of the other aluminas are more or less hydrated and porous. The following decomposition sequences of metastable forms were found [48]:

— Oxide-Hydroxide

- Diaspore $\xrightarrow{450^\circ}$ α-Al_2O_3
- Boehmite $\xrightarrow{450^\circ}$ γ $\xrightarrow{600^\circ}$ δ $\xrightarrow{1000^\circ}$ θ $\xrightarrow{1200^\circ}$ α-Al_2O_3

— Trihydroxide

- Hydrargillite $\xrightarrow{250^\circ}$ χ $\xrightarrow{900^\circ}$ κ $\xrightarrow{1200^\circ}$ α-Al_2O_3

  180° $\searrow$ dry Atmosphere

  Boehmit $\xrightarrow{450^\circ}$ $\gamma \cdots\cdots$

  180° $\nearrow$ dry Atmosphere

- Bayerit $\xrightarrow{250^\circ}$ η $\xrightarrow{850^\circ}$ θ $\xrightarrow{1200^\circ}$ α-Al_2O_3

  in high-vacuum:

- Nordstrandite, Bayerite, Hydrargillite $\xrightarrow{400^\circ}$ γ $\xrightarrow{750^\circ}$ θ $\xrightarrow{1200^\circ}$ α-Al_2O_3.

Two series of phase transformations of various aluminas which do not imply dehydratation are represented below (with a=amorph):

— α-Al_2O_3+ Ions-Implantation $\longrightarrow$ a-Al_2O_3 $\xrightarrow{950^\circ}$ γ-Al_2O_3 [49]

— Al $\xrightarrow{+O_2}$ a-Al_2O_3 $\xrightarrow{900^\circ}$ γ-Al_2O_3 [50].

The properties of some alumina phases are listed in Table 4.1. All alumina phases consist of closed packed oxygen basis (hcp or fcc) lattice. On this basis lattice, the Al^{3+} ions are placed on different positions with octahedral or tetrahedral symmetry. The α-Al_2O_3 belongs to the so called ABAB... group. The oxygen ions form a hexagonal closed packed (hcp) structure and the Al^{3+} ions occupy two thirds of the octahedral positions. The γ-, γ'- and θ-Al_2O_3 belong to the ABCABC... group. In this case the oxygen atoms form a face-centered cubic (fcc) lattice. The Al^{3+} ions occupy octahedral and tetrahedral positions. The γ-Al_2O_3 has a "defect spinel" structure with 32 oxygen atoms per unit cell. The appropriate formula is $Al_{21\ 1/3}\square_{21\ 2/3}O_{32}$, where $\square$ represents the vacancies in the spinel structure.

Oxide	**Spatial Group**	**a,b,c [Å]** β	Oxygen sublattice	Occupied interstices	**Remarks**
α-Al_2O_3	hexagonal D^6_{3d}	a=4,7589 c=12,991	hcp	octahedral	Corundum
κ-Al_2O_3	hexagonal	a=9,71 c=17,86		octahedral+ tetrahedral	
γ'-Al_2O_3	cubic	a=3,95		octahedral+ tetrahedral	
γ-Al_2O_3	cubic O^7_h	a=7,911	fcc	octahedral+ tetrahedral	Spinel-Type
δ-Al_2O_3	tetragonal	a=7,96 c=11,70	fcc	octahedral+ tetrahedral	distorted Spinel-Typ
θ-Al_2O_3	monoclinic C^3_{2h}	a=2,92 b=5,64 c=11,83 β=103°	fcc	octahedral+ tetrahedral	isomorphic with β-Ga_2O_3
β-Al_2O_3	hexagonal	a=5,60 c=22,50		octahedral+ tetrahedral	

Table 4.1: Crystal structures of some alumina phases [51]

The γ'-Al_2O_3 has also a spinel structure but the unit cell is only half of the γ-Al_2O_3 unit cell. Fig. 4.1 shows a simplified spinel structure. The octahedral and one tetrahedral site of Al^{3+} as well as the fcc of O^{2-} ions are indicated. The other tetrahedra are not shown in this figure for simplicity. One corner of the tetrahedra coincide with one corner of the cube while the basal planes coincide with the octahedra's faces. The θ-Al_2O_3 has a monoclinic structure derived from the spinel through a specific arrangement of the Al ions in the interstices.

The α- γ-, γ'- and θ-Al_2O_3 are the oxide phases which we met in our work.

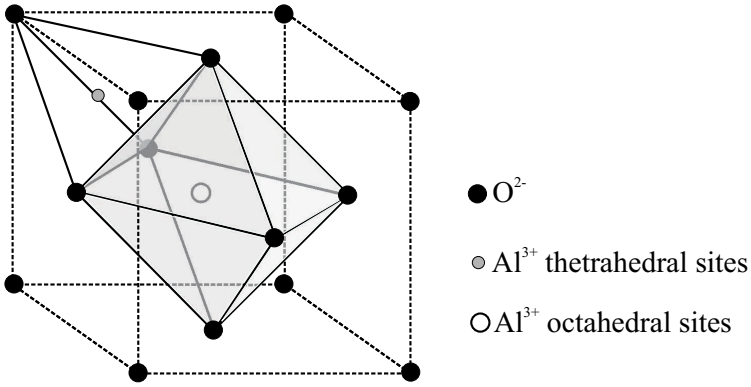

Figure 4.1: A simplified representation of the spinel structure. The fcc structure of oxygen ions is shown as well as tetrahedral and octahedral sites of the Al ions.

4.2 The intermetallic compounds Ni_3Al and CoAl

Intermetallic compounds, often called 'bulk intermetallics', differ in a number of important ways from conventional metal alloys [52]. The atoms in conventional alloys are linked with relatively weak metallic bonds, with the atomic nuclei floating in a 'gas' of electrons which are able to move relatively freely (the reason for good electrical conductivity). In contrast, the bonds in intermetallics may be partially ionic or covalent, and therefore stronger [52]. Alternatively, the bonding may be entirely metallic, but the atoms of the individual elements take up preferred positions within the crystal lattice. This condition, which is referred to as 'ordering', leads to an abrupt change in the mechanical properties of the material. These phenomena give the bulk intermetallics their characteristic properties - high melting points and great strength (particularly at high temperatures), but poor ductility. An intermetallic compound, is a particular chemical compound based on a definite atomic formula, with a fixed or narrow range of chemical composition. An example is the nickel aluminide Ni_3Al. Since the 1970s, intermetallic compounds have come into focus as high-performance materials [53].

4.2.1 Ni_3Al

The phase diagram for the Ni-Al system is shown in figure 4.2. Ni-Al exhibits a wide stability range. There are five ordered intermetallic compounds Ni_3Al, NiAl, Ni_5Al_3, Ni_2Al_3 and $NiAl_3$. The Ni_3Al is the most Ni-rich phase. The melting point of Ni_3Al is 1385°C. Its stability range [54] is rather narrow, compared to the other intermetallic phases. Ni_3Al is a prototypical, highly ordered intermetallic phase. This compound caused technological interest because of the well known yield stress anomaly for single crystals [55] at high temperatures, which is explained on the basis of dislocation cross slip [56] models.

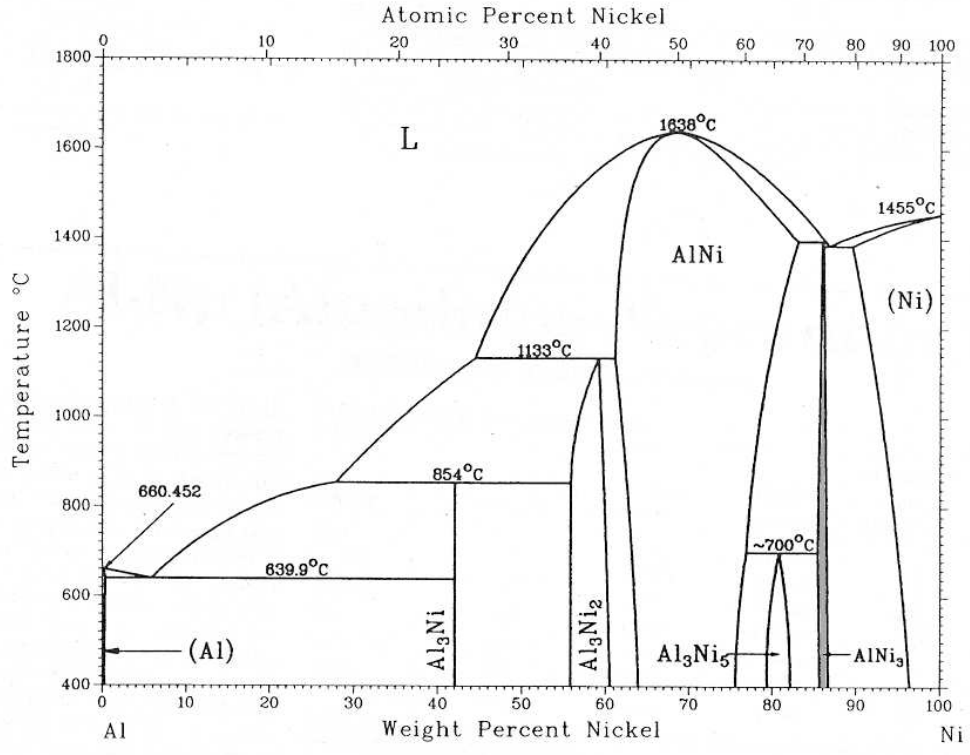

Figure 4.2: The phase diagram of the Ni-Al system [54].

Ni_3Al crystallizes in the LI_2 (Cu_3Au-type) structure, which is cubic (space group Pm3m) and contains four atoms per unit cell [57]. This is a fcc structure with Al atoms located at the cube corners and Ni atoms occupying the face centers (Fig. 4.3).

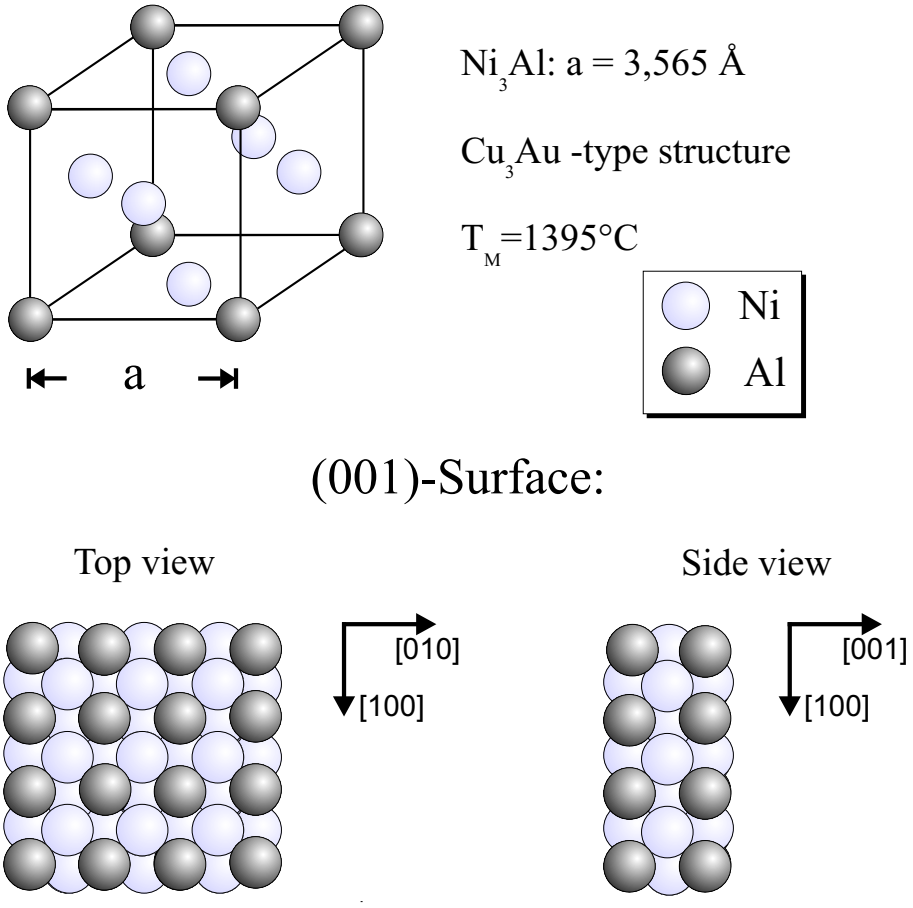

Figure 4.3: The Ni_3Al structure.

There are two possible terminations for the $Ni_3Al(100)$ surface, the first one contains 50% Ni and 50% Al (mixed layer), the second possible configuration being 100% Ni. Fig. 4.3 shows the top and the side view of the mixed layer termination. First principle calculations of the cohesive energy and LEED investigations suggested that the mixed-layer surface is more stable [57]. In ref. [57] the authors found that the second layer of atoms are at bulk positions, the top layer Ni atoms are relaxed inward by 0.05 ± 0.03 Å , and the aluminum atoms sit 0.02 ± 0.03 Å above the Ni atoms.

The surface energy values give valuable indications concerning the possible termi-

Face	Termination	EAM [58]	EDFM [59]	BSF [60]
(100)	50%Al-50%Ni	1620	2108	2852
	Ni-rich	1885	-	3168
(110)	50%Al-50%Ni	1730	2290	3117
	Ni-rich	1920	-	3964
(111)		1645	1887	2411

Table 4.2: Surface free energies of Ni_3Al (mJ/m^2).

nations of a specific surface. The calculated surface energies of relaxed (100), (110) and (111) surfaces by the Embedded Atom Method (EAM) [58], Electron Density Functional Method (EDFM) [59], and by a method developed by Bozzolo, Ferrante and Smith (BSF) [60] are shown in Table 4.2. The mixed composition truncation of the $Ni_3Al(100)$ surface has a lower surface energy that that of the pure Ni plane terminated surface in all cases. Folies and Daw [58] have calculated the surface energy and atomic relaxation of $Ni_3Al(001)$ surface using EAM. The surface relaxation was found to be small, all atoms being close to their bulk positions except for the top aluminum atoms which are relaxed outward by 0.06 Å. The BSF method gives a relaxation of aluminum atoms of 0.12 ± 0.04 Å. The EAM gives a prediction for the surface energy of pure metals typically 50% lower than experimental data [60]. According to Ref. [60] a value of surface free energy close to those obtained by the BSF method appears to be more realistic.

Ni_3Al is a weak ferromagnet with a Curie temperature of 70 K [61].

4.2.2 CoAl

The phase diagram for the Co-Al system is shown in figure 4.4. The β-phase of the Co-Al alloys (50 at.% Co and 50 at.% Al) forms a stable B_2 (CsCl-type) structure over a wide range of Al concentration [62] (the same structure as Ni-Al and Co-Ga). The unit cell contains two atoms and the lattice constant of the CoAl structure is

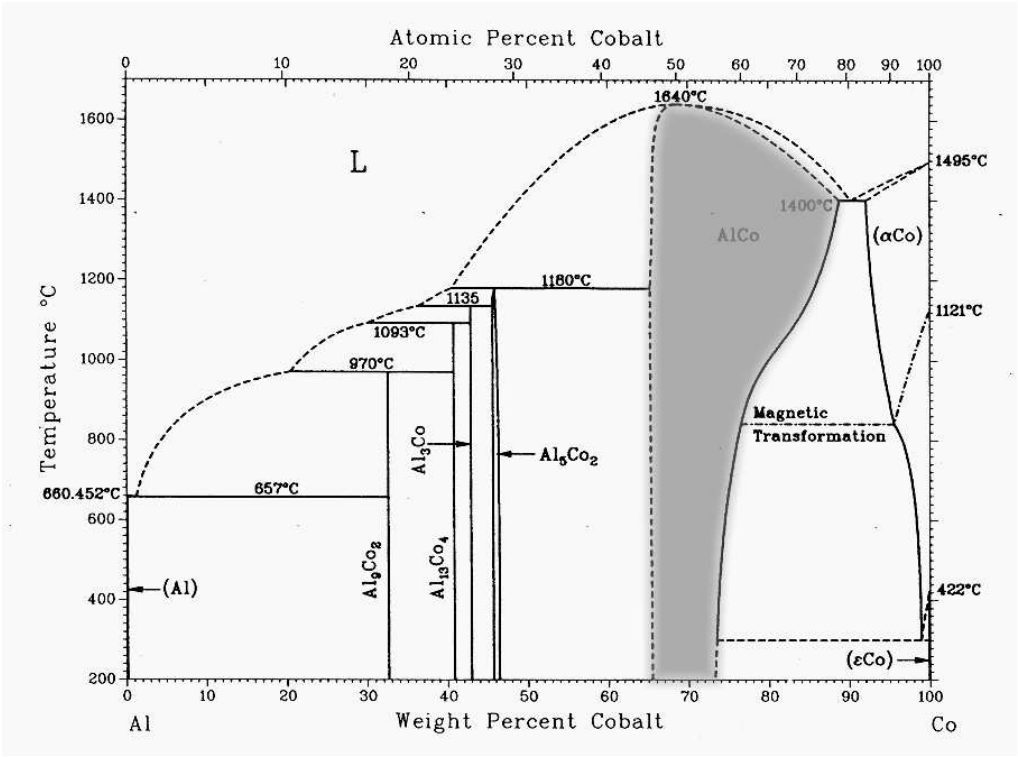

Figure 4.4: The phase diagram of the Co-Al system [54].

a = 2.862 Å [63, 64]. These systems are designated as T-B alloys. The T- and B metal atoms form interpenetrating primitive cubic lattices at the stoichiometric composition. Since the β-phases exist over a wide composition range, the T-B alloys show structural disordering resulting from a deviation of stoichiometry. At a concentration of T-metal less than 50 at. %, anomalous large vacancy concentrations are present in the sublattice of T atoms. At concentrations higher than 50 at. % T-metal atoms occupy B metal sites substitutionally and these atoms are described here as T metal anti-structure atoms (ATS). In the case of Co-Al alloys the so-called anti-structure of Co atoms plays an important role in determining the magnetic properties of these alloys. The perfectly ordered equiatomic CoAl alloy does not exhibit any magnetic behaviour [65]. The magnetic moment of cobalt vanishes because of compensation of the unpaired spin due to the charge transfer of ≈ 0.25 electrons from the Al atoms. However, as the Al concentration decreases,

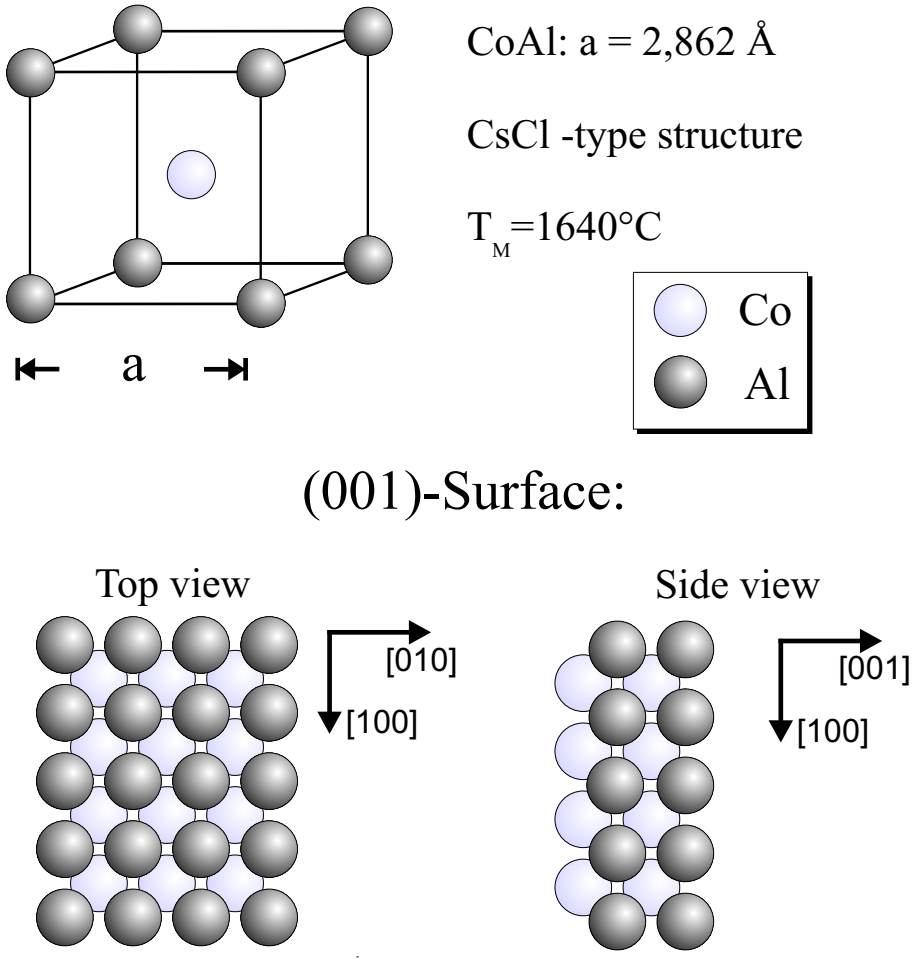

Figure 4.5: The CoAl structure.

not only the anti-structure Co atoms but also the neighboring eight Co atoms carry substantial magnetic moment [66]. Above 50 at.% Co it becomes ferromagnetic with the Curie temperature increasing up to 120 K for 57.9 at.% Co [66]. CoAl is very similar to the NiAl compound with respect to density, thermal expansion behaviour and melting temperature (1640°C) [67]. A side and top view of the (100) surface is also shown in figure 4.5. The ideal (100) plane has a quadratic unit cell with C_4 symmetry and is terminated either by an Al or by a Co layer. The planes parallel to the (100)-plane have a ABAB... stacking sequence and the distance between the layers is 1.43 Å.

Chapter 5

Cobalt growth on $Ni_3Al(100)$

This chapter presents the growth of Co on the $Ni_3Al(100)$ surface. The experiments were carried out using AES, LEED and STM. As the substrate is a key factor for the morphology of the grown film, at the beginning of this chapter a short presentation of the cleaning procedure of $Ni_3Al(100)$ surface is given. Afterwards, the experimental results of the cobalt deposition on $Ni_3Al(100)$ surface are presented.

5.1 The clean $Ni_3Al(100)$ surface

The experiments were performed in the UHV system described in Chapter 3. The base pressure of the chamber was 1×10^{-10} mbar. The $Ni_3Al(100)$ single crystal was cut by spark erosion and polished mechanically. It was oriented using a X-ray diffractometer with an accuracy of 0.1°.

The clean $Ni_3Al(100)$ surface was obtained after several cycles of argon ions sputtering (1kV; 5.4 $\mu A/cm^2$) followed by annealing at 1400 K. Fig. 5.1 shows the AES spectrum of clean $Ni_3Al(100)$. The inset of Fig. 5.1 shows the AES spectrum in the energy region between 40 and 80 eV. The AES transitions of $Ni^0(M_{2,3}VV)$ at 61 eV and $Al^0(L_{2,3}VV)$ at 68 eV are clearly resolved. In the high energy region the AES spectrum exhibits the Ni triplet at 716, 783 and 884 eV (L_3VV) and the KLL transitions of Al with the predominant transition at 1396 eV [68]. Fig. 5.2a

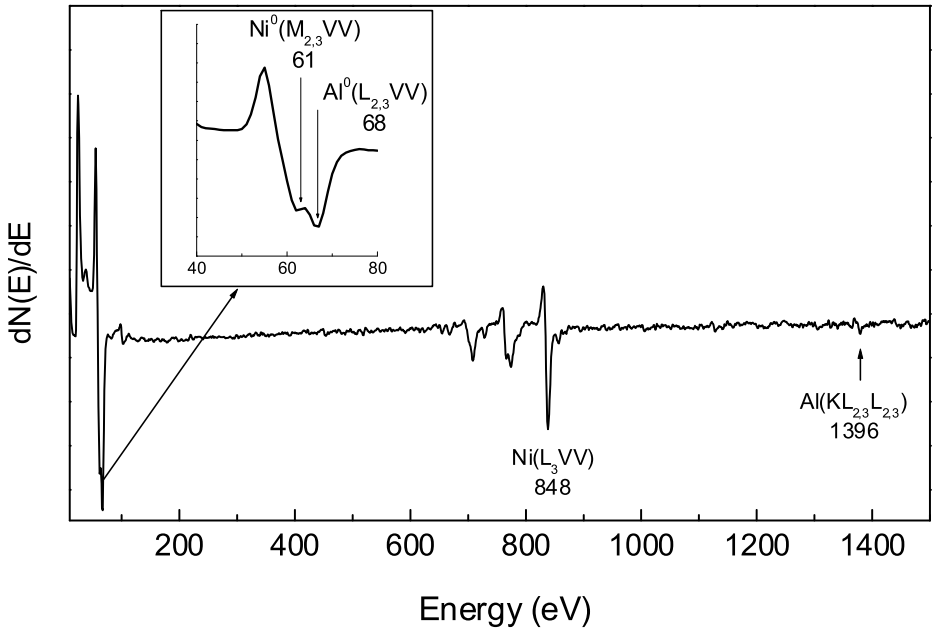

Figure 5.1: AES spectra of the clean $Ni_3Al(100)$ surface.

shows a large scan area (3392×3392 Å^2) STM image of the $Ni_3Al(100)$ surface. The image displays flat and large terraces (500 - 1000 Å) separated by steps. The height difference between two neighboring terraces was estimated by a line scan (see Fig. 5.2b). The step height is about 3.5 Å which agrees with the lattice constant of Ni_3Al and represents a double atomic step. This suggests that different terraces have always the same termination. The LEED pattern of clean $Ni_3Al(100)$ shows a (1×1) structure (Fig. 5.2c).

5.2 Growth of Co on $Ni_3Al(100)$

5.2.1 AES and LEED

Cobalt was evaporated from a rod (2 mm diameter) with a deposition rate between 0.3 and 1 ML min^{-1}. Before each deposition experiment the Ni_3Al surface was cleaned in order to remove the previous cobalt layer.

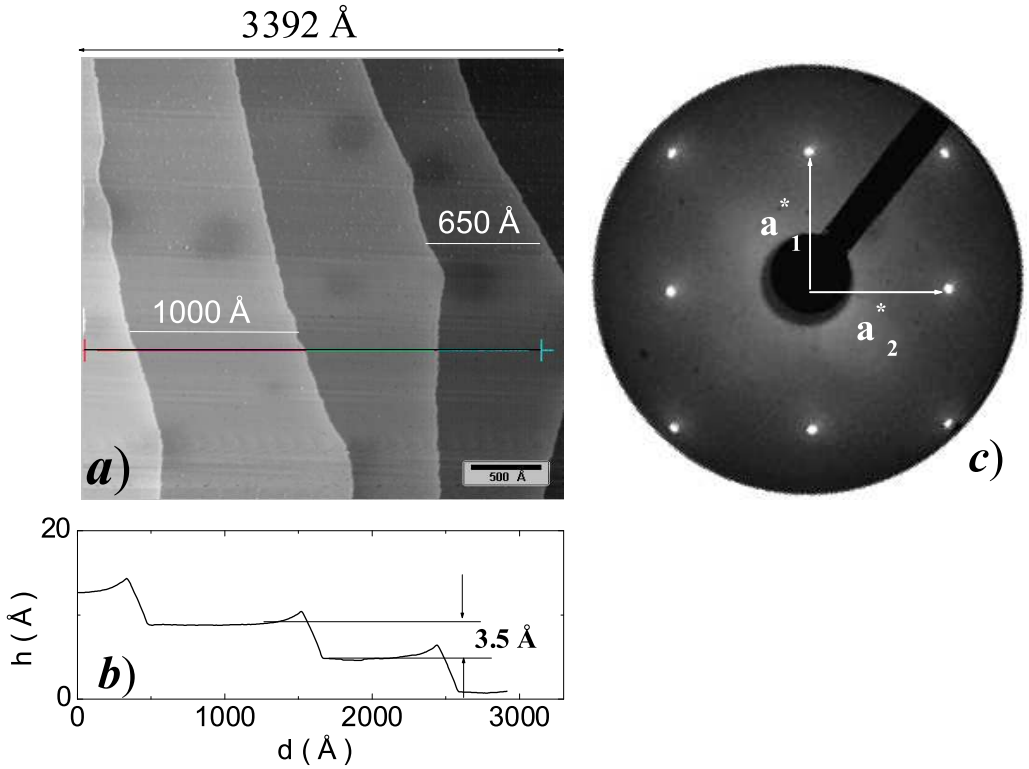

Figure 5.2: (a)The STM image of $Ni_3Al(100)$, U_t = 1.2 V; I=0.7 nA; (b) A line scan which allows the estimation of the step height; (c) The LEED pattern of the clean $Ni_3Al(100)$ surface showing a (1×1) structure (E_p= 54 eV).

Fig. 5.3a shows three Auger spectra after the deposition of Co on the $Ni_3Al(100)$ surface. At top AES spectrum of the clean $Ni_3Al(100)$ is shown as reference. The middle and the bottom AES spectra in Fig. 5.3a show the $Ni_3Al(100)$ surface after a nominal deposition of 7 and 20 Å Co, respectively. In the low energy range of these spectra it can be observed that, the Ni(61) and Al(68) AES signals gradually decreases as the Co(53) signal occurs. In the high energy range the Co transitions at 656, 716 and 775 eV appear in addition to the Ni transitions. Since the Ni(716, 783) and Co(716, 775) AES transitions overlap, we used the Ni signal at 848 eV for the estimation of the thickness of the Co film. The dependence of the peak-to-peak (p-to-p) intensity of Ni(848) as a function of the nominal Co thickness is displayed in the figure 5.3b. Analyzing the attenuation of Ni signal at 848 eV due to the Co

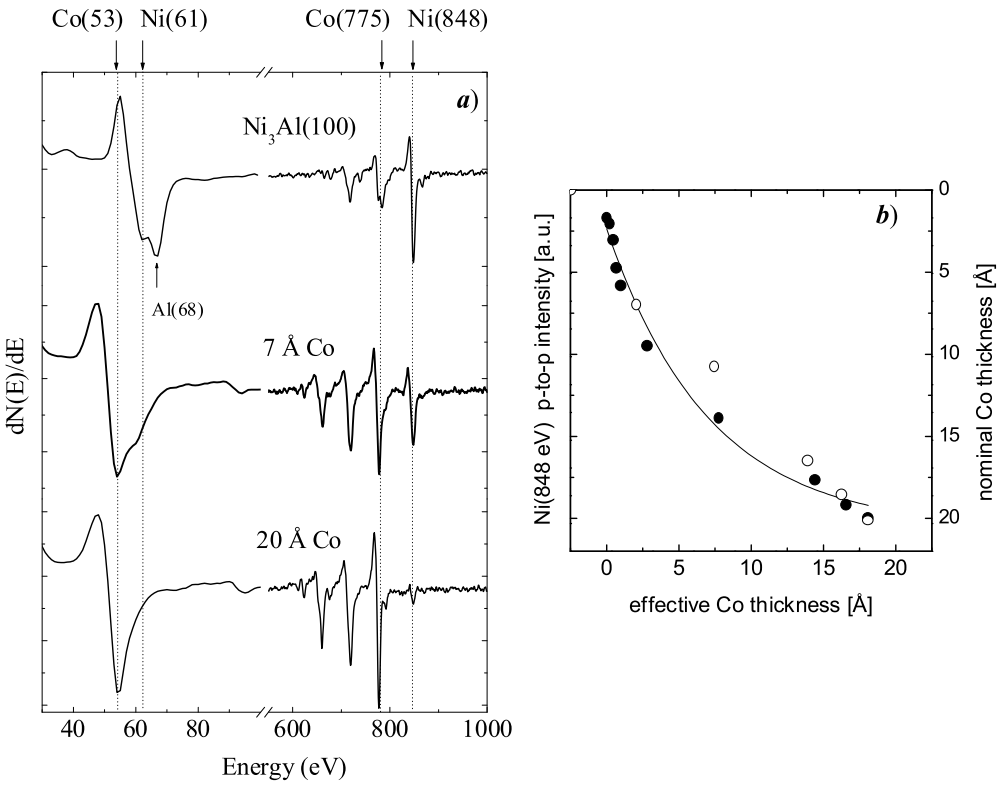

Figure 5.3: (a)Auger spectra of $Ni_3Al(100)$ surface as a function of Co deposition; (b) The p-to-p intensity of Ni(848 eV) as a function of Co deposition.

overlayer and assuming a layer-by-layer growth, a rough estimation of the Co film thickness, d, was made. We used the formula:

$$I_{Ni} = I^0_{Ni} \cdot e^{\frac{-d_{Co}}{\lambda_{Co}(E_{Ni})\cos\theta}} \tag{5.1}$$

with a mean free path $\lambda_{Co} = 14$ Å according to Ref. [69]. The thickness of the Co layer estimated in this way is ~ 4 Å for a nominal deposition of 7 Å, and ~ 18 Å for a nominal deposition of 20 Å. As will be shown, the lower value of Co thickness estimated from AES can be attributed to an island growth mode. The LEED pattern after Co deposition at 300 K exhibits only a diffuse background.

In order to study the thermal stability of the cobalt film (20 Å) on Ni_3Al we have annealed the system in steps of 100 K up to 1000 K. Fig. 5.4a shows the AES spectra of Co/Ni_3Al system taken after 20 Å Co nominal deposition at room temperature

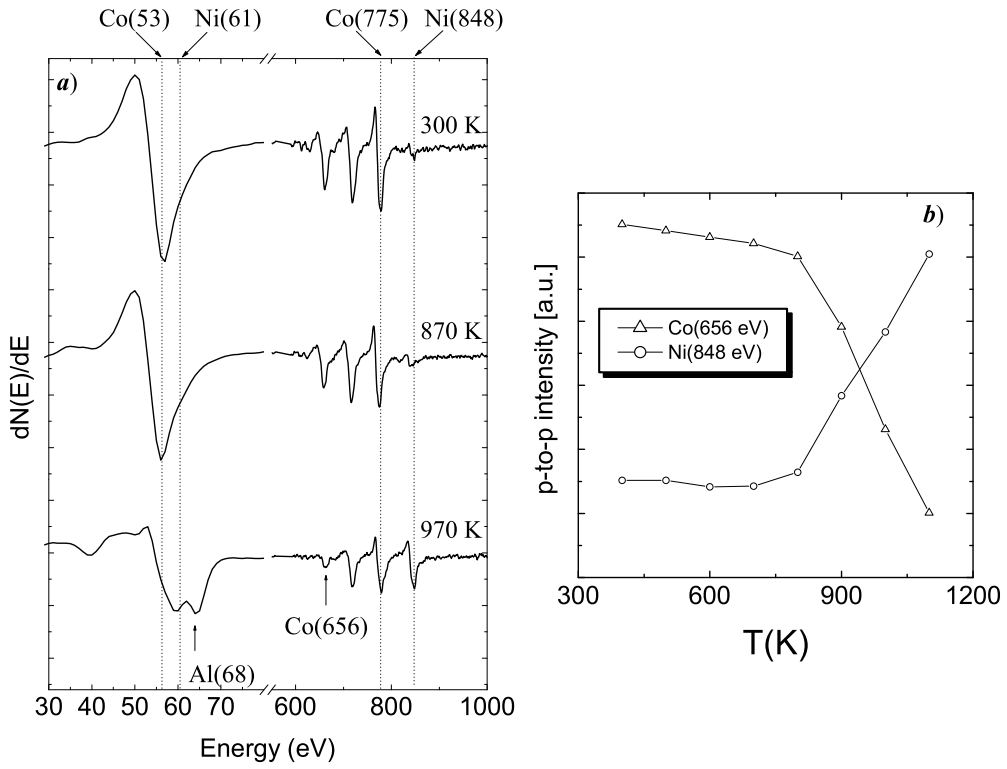

Figure 5.4: (a)Auger spectra of 20 Å $Co/Ni_3Al(100)$ after deposition at 300 K and after annealing at 870 K and 970 K; (b) p-to-p intensity of Co(656 eV) and Ni(848 eV) AES transitions as a function of annealing temperature.

(top spectrum), after annealing at 870 K (middle spectrum) and 970 K (bottom spectrum). There is almost no difference between the spectrum at 300 K and that at 870 K, only a small decrease of the Co signal in the high energy region is found. After annealing at 970 K the Co(53) signal becomes very weak while the Ni(61) and the Al(68) transitions can be clearly observed. The Ni(848) signal becomes, also, more intense while the intensity of the Co triplet is strongly decreased. This suggests that at 970 K the Co film has disappeared almost completely from the surface. Fig. 5.4b shows the Co signal at 656 eV and the Ni signal at 848 eV as a function of annealing temperature. The Co signal at 656 eV and the Ni signal at 848 were chosen because they originate entirely from the Co and Ni atoms, respectively. Up to $\sim$ 750 K the signals remain constant indicating the thermal stability of the

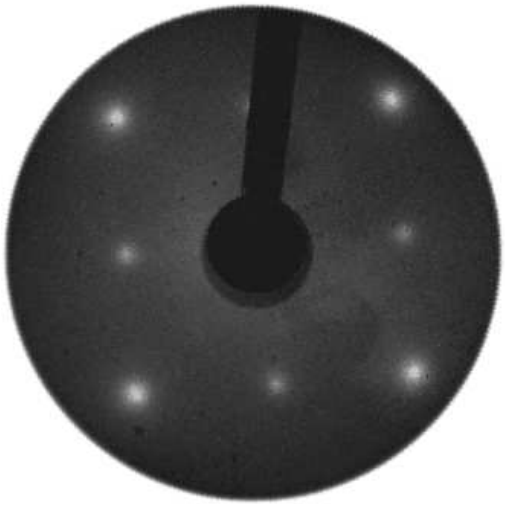

Figure 5.5: The LEED pattern of 20 Å $Co/Ni_3Al(100)$ after annealing at 700K (E_p=54 eV).

$Co/Ni_3Al(100)$ system. Above $\sim$ 750 K the Co signal decreases and at 1100 K it has vanished completely. Above $\sim$ 750 K the Ni signal increases strongly. It may be that above 750 K an Al-Ni-Co alloy is formed in the surface region. After annealing at 1100 K only the specific AES transitions of Ni_3Al are observed in the AES spectrum indicating that the Co atoms have diffused deeply into the Ni_3Al crystal.

Fig. 5.5 shows the LEED pattern of 20 Å nominal cobalt film deposited at 300 K on $Ni_3Al(100)$ surface after subsequent annealing at 700 K. Since up to 750 K the Co film is stable on the surface, the LEED pattern shown in figure 5.5 is attributed to the Co film. The LEED pattern can be explained by a c(2×2) reconstruction of the (100) surface of fcc Co. The basis vector of the c(2×2) unit mesh of fcc Co is equal to 3.56 Å, which corresponds to the lattice constant of fcc Co. The stabilization of a fcc phase was also reported for Co on Ag(001) [70] for low coverage (< 2ML). A close inspection of the LEED pattern shows that the Bragg reflections are broadened with respect to those of the clean Ni_3Al surface (see figure 5.2c). The reason could be that not the whole surface is covered with an ordered Co film and only some ordered islands are formed on the surface. This assumption is supported by the STM measurements. A very rough estimation [11] of the mean island diameter

(assuming circular islands of uniform size) gives a value of $\sim$ 100 Å.

5.2.2 The morphology of the Co/Ni_3Al(100) surface

In this section the surface morphology of Co films deposited on $Ni_3Al(100)$ is presented. The deposition temperatures were 300 K and 500 K, respectively. However,

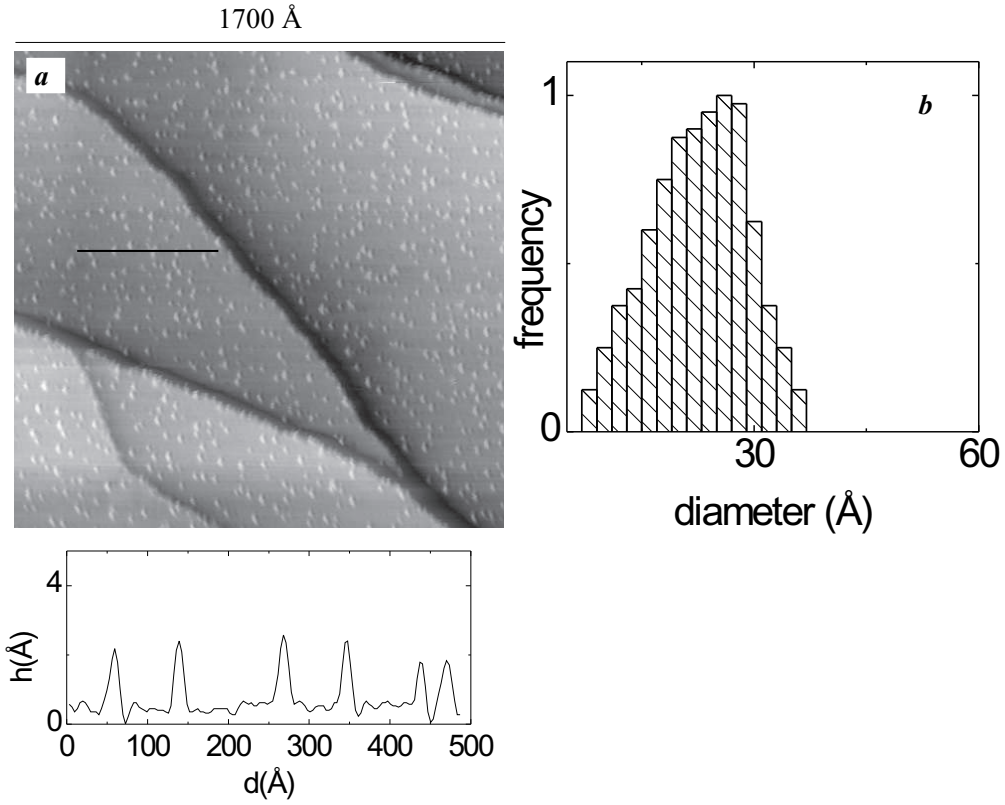

Figure 5.6: (a) STM image of 0.1 ML Co/$Ni_3Al(100)$ (U_t = 1.15 V; I_t = 1.2 nA); (b) The diameter distribution of Co islands.

due to the experimental limitations, the STM images were always taken at room temperature.

Fig. 5.6a shows a STM image with a scanned area of 1700×1700 Å^2 after deposition of 0.1 ML of Co at 300 K. Co grows in more or less circular islands with an island density of $\sim$ 2.65×10^{12} cm^{-2}. Fig. 5.6b shows the diameter distribution of the Co

islands after deposition of 0.1 ML Co at 300 K. The distribution exhibits a maximum

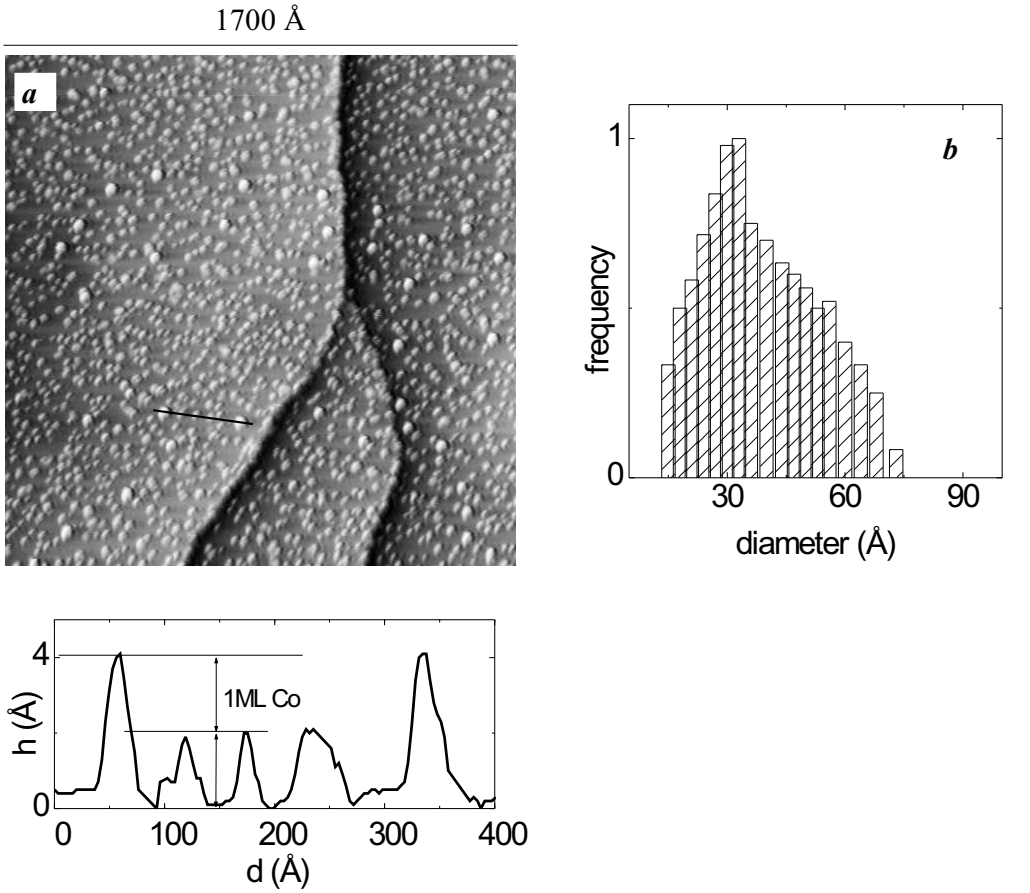

,

Figure 5.7: (a) The STM image of 0.3 ML Co/$Ni_3Al(100)$ ($U_t = 2.15$ V; $I_t = 0.7$ nA); (b) The diameter distribution of Co islands.

of the diameter centered at ~ 25 Å. The estimation of the island size can be affected by errors due to the tip convolution [71]. In order to estimate the height of the islands a line scan was performed. The line scan presented bellow the figure 5.6a shows an uniform height of the island of ~ 2 Å. The diameter of a Co atom amounts to ~ 2.8 Å. Therefore the height 2 Å corresponds to a two-dimensional growth of Co on the $Ni_3Al(100)$ surface. The two-dimensional growth can be explained by the surface free energy of Co (2709 mJ/m^2) which is close to that of the $Ni_3Al(100)$ surface calculated by BSF the method (2852 - 3168 mJ/m^2).

Fig. 5.7a shows a STM image after deposition of 0.3 ML Co. The islands den-

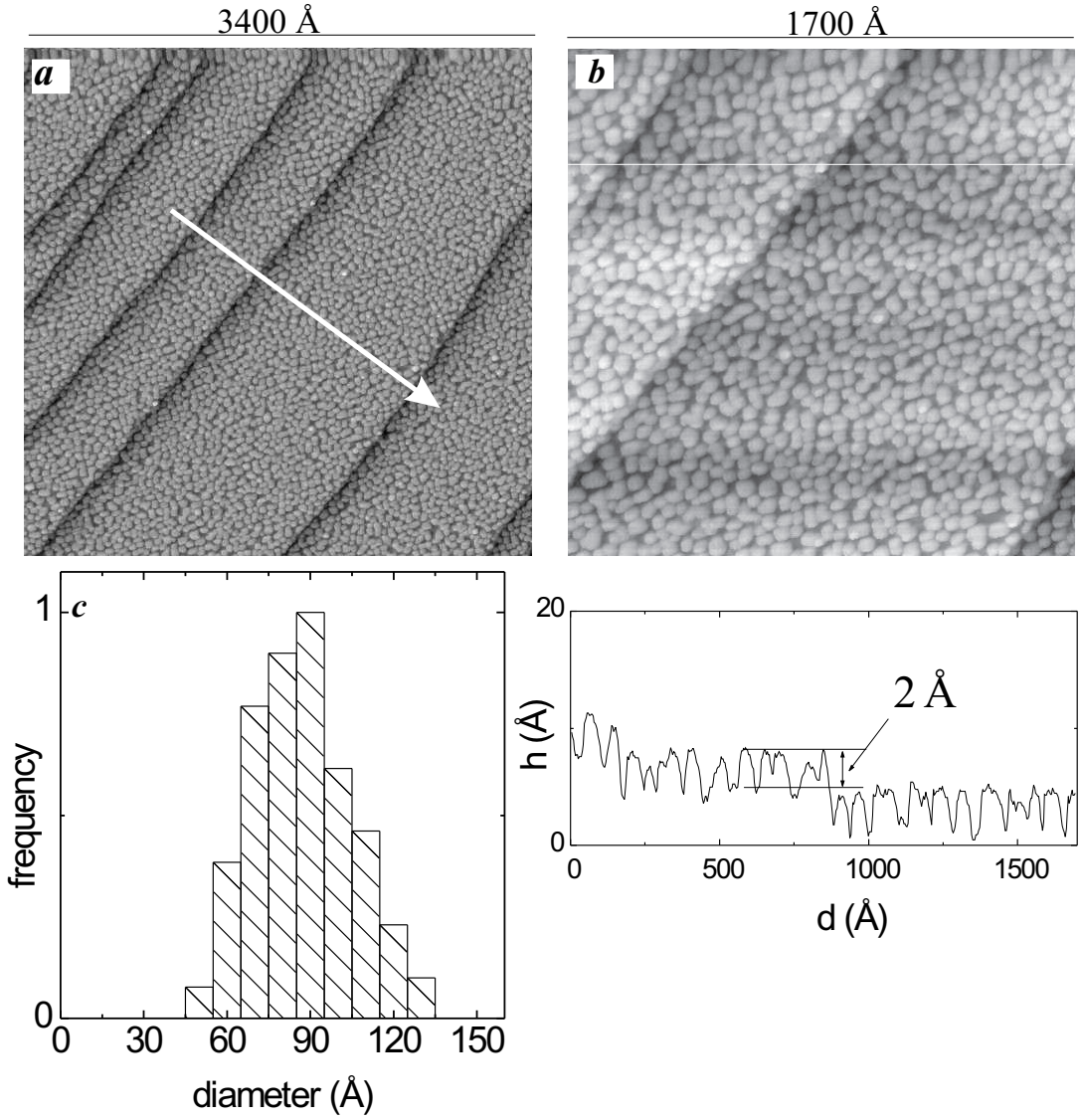

Figure 5.8: (a,b) STM images after a nominal deposition of 3.5 ML Co on $Ni_3Al(100)$ (U_t = 1.82 V; I_t=0.2 nA); (c) The island size distribution.

sity (5.18×10^{12} cm^{-2}) is increased accordingly indicating a homogeneous nucleation process. Fig. 5.7b shows the distribution of the island diameter after deposition of 0.3 ML Co. This distribution exhibits a maximum centered at $\sim$ 35 Å and a shoulder at higher values. The shoulder could be associated with islands where nucleation

in the second layer takes place. The nucleation phenomenon in the second layer is clearly observed in the linescan below the Fig. 5.7a. Two different heights at $\sim$ 2 Å and $\sim$ 4 Å are found. The height 2 Å corresponds to a two-dimensional growth, while the height of 4 Å shows that for this deposition the nucleation already starts in the second layer.

Fig. 5.8a shows a STM image with a scanned area of 3400×3400 Å^2 after a nominal deposition of 3.5 ML at 300 K. The Co islands are uniform distributed over all terraces and the step edges between the terraces are clearly observed. Fig. 5.8b shows the section of Fig. 5.8a indicated by the arrow with a scanned area of 1700×1700 Å^2. The surface displays a morphology consisting of cobalt islands and no underlying substrate can be observed. Fig. 5.8c presents the diameter distribution of the islands with a maximum around 90 Å. The linescan below the figure 5.8b shows a corrugation of 2 - 3 Å. For a nominal deposition of 3.5 ML (7 Å nominal deposition) the thickness of the Co film was estimated by AES to be $\sim$ 4 Å which corresponds to $\sim$ 3 layers of fcc Co. The STM image suggests that the film consists of Co layers which are homogeneously covered by Co islands with a mean diameter of $\sim$ 90 Å. Concerning the measured corrugation of these islands we have to note that both lateral and vertical dimensions are altered due the to so-called "tip shape limited resolution"[72]. Consequently, the apparent corrugation and island size could be slightly different from the real ones.

Afterwards, the Co/$Ni_3Al(100)$ sample was annealed to 700 K. Fig. 5.9a shows a STM image with a scanned area of 1700 × 1700 Å^2 after annealing at 700 K. A coalescence of the Co islands takes place, and large and flat islands are observed. The inset of figure 5.9b shows a schematic representation of the Co film on $Ni_3Al(100)$. On top of the Co layers large islands of Co were found. In addition some small cobalt islands with a height of $\sim$ 2 Å and a mean diameter of $\sim$ 30 Å can be observed randomly distributed on top of the large islands. The distribution of the islands area is also given in Fig. 5.9b. The small islands give the first maximum with an area of $\sim$ 1500 Å^2 . The distribution shows that the larger islands have areas with

a maximum around 8000 Å^2, i.e. by assuming a circular shape this corresponds to a mean diameter of $\sim$ 100 Å. After annealing at 700 K, the topography (morphology) of the Co/$Ni_3Al(100)$ surface is in agreement with the LEED and AES data. With AES it was found that the Co film is stable up to $\sim$ 750 K on $Ni_3Al(100)$. This suggests that only a re-arangement of Co on the surface takes place. After annealing

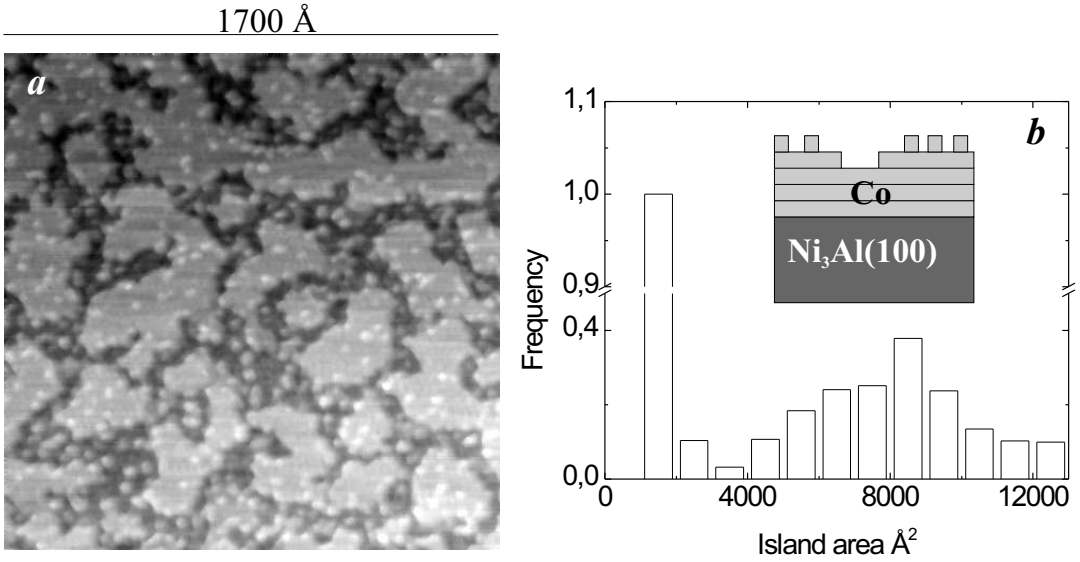

Figure 5.9: (a) STM image of 3.5 ML of Co deposition on $Ni_3Al(100)$ after annealing at 700 K, U_t = 1.5 V; I_t=0.2 nA.; (b) The island size distribution after annealing at 700 K; inset: the schematic representation of the Co film configuration after annealing.

at 700 K, a LEED pattern was found which corresponds to a c(2×2) reconstruction of the (100) surface of fcc Co. The mean diameter of the Co domains was estimated to be $\sim$ 100 Å. This is in agreement with the STM findings where large islands with an area of $\sim$ 8000 Å^2 are found. Therefore, the large and flat Co islands obtained after annealing at 700 K, allow the formation of the Bragg reflections which are observed very clearly in figure 5.5.

As our experiments revealed, kinetic factors are playing an important role. The deposition at room temperature leads to a non-equilibrium configuration of the

deposited film consisting of small islands. The increase of inter-diffusion during annealing drives the system into a more stable energetic configuration which consists of large two-dimensional islands, as it is schematically shown in the inset of figure 5.9d.

The evolution of islands obtained after deposition at 300 K to large, flat islands after annealing at high temperature resembles the phenomenon found for Fe deposited on Ag(100)[73].

- *Deposition at 300 and 500 K*

Fig. 5.10 shows two STM images of 0.3 ML of Co deposited on $Ni_3Al(100)$ at 300 and 500 K, respectively. In the case of cobalt deposition at 300 K, the island density (5.18×10^{12} cm^{-2}) is much higher than that of the islands obtained by deposition at 500 K (0.94×10^{12} cm^{-2}). Accordingly, the island mean diameter increases with

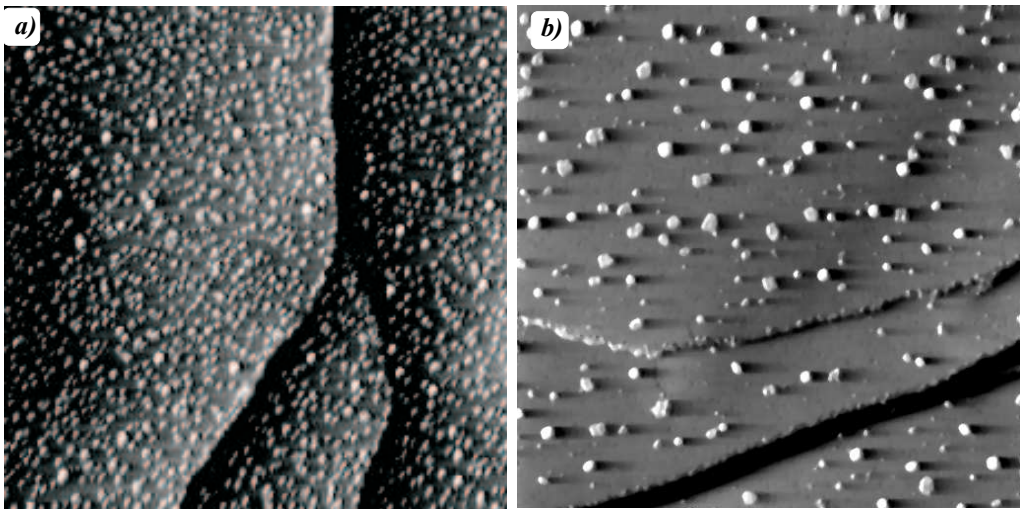

Figure 5.10: STM image of : a) 0.3 ML Co deposited on $Ni_3Al(001)$ surface at 300 K (1700×1700 Å^2; $U_t = 0.76$V; $I_t = 0.6$ nA); b) 0.3 ML Co deposited on the $Ni_3Al(100)$ surface at 500 K (1700×1700 Å^2; $U_t = 1.42$ V; I_t=0.6 nA).

increasing of deposition temperature from $\sim$ 30 Å to $\sim$ 80 Å. As mentioned before, at 300 K and 0.3 ML Co, nucleation takes also place in the second layer of the islands. At 500 K, the line-scan (not shown here) indicates that Co grows only

two-dimensionally and the decrease of the island density is due to an increase in island size. According to the *mean-field nucleation theory* [71] this can be explained by an increase in the diffusion coefficient. A large diffusion coefficient means a higher probability for a new deposited atom to find an island before it is involved in a nucleation process with another free adatom, and also a higher mobility of small islands which can coalesce [74]. Consequently, at higher temperature, the growth process is favored with respect to nucleation. On the other hand the line scan reveals a two-dimensional growth of cobalt islands. Consequently, if at room temperature the energy barriers at the step edges of islands still prevent the adatoms from jumping down, at 500 K they overcome this barrier.

5.3 Summary

At low coverage (0.1 ML) and 300 K, the cobalt deposited on the $Ni_3Al(100)$ surface shows two-dimensional growth. For deposition of 0.3 ML, the nucleation also takes place in the second layer. Cobalt (0.3 ML) deposited at 500 K shows larger islands with respect to the deposition at room temperature, and no nucleation in the second layer occurs. This is attributed to a higher diffusion coefficient. The surface of 3.5 ML Co deposited at 300 K displays a morphology of islands with a mean diameter of ~ 90 Å. This configuration is unstable with regard to annealing which drives the system into an equilibrium configuration of large and flat islands. After annealing at 700 K the fcc structure is stabilized, and the cobalt grows with the (100) plane parallel to the substrate. The cobalt film is stable on the $Ni_3Al(100)$ surface up to 750 K, when it starts to diffuse into the substrate. At 1100 K Co disappears completely from the surface via diffusion into the surface.

Chapter 6

The oxidation of $Ni_3Al(100)$

In this chapter the growth of the Al_2O_3 films on the (100) surface of Ni_3Al is presented. Alumina (Al_2O_3) is of great interest in various application areas such as heterogeneous catalysis, coatings, microelectronics and thin-film devices [75]. It exists in several phases, as was shown in section 4, the most notable of which are α-Al_2O_3 (Corundum) and the γ-Al_2O_3 phases.

Bulk alumina or other oxide samples cannot be easily investigated by STM or conventional electron spectroscopic methods, because they are insulating and produce charging effects. This drawback can be overcome by employing thin oxide films grown on a suitable substrate as model systems [1]. Ni-Al compounds, in various stoichiometry, are well known as suitable alloys for the preparation of thin alumina films through direct oxidation [1, 76, 77, 38, 78]. The formation of Al_2O_3 is thermodynamically favored, having a heat of formation (ΔH_f = -1675.7 kJ·mol^{-1}) higher than the corresponding value for NiO (ΔH_f = -240 kJ·mol^{-1}) [79]. It is known also from XPS measurement that only Al atoms are oxidized while Ni atoms remain unaffected [80, 81]. In this chapter the oxidation of the $Ni_3Al(100)$ surface will be presented. The chapter is organized as follows: In section 6.1, the oxidation of $Ni_3Al(100)$ at 300 and 1100 K, studied by AES is presented. Section 6.2 deals with the vibrational properties of the Al_2O_3 film grown on $Ni_3Al(100)$ surface. Section 6.3 shows the LEED investigations results. The morphology of the aluminum oxide film

obtained by STM is presented in the section 6.5. In section 6.6 the results obtained after oxidation of the $Ni_3Al(100)$ surface, in a pressure range $\geq 5\times 10^{-7}$ mbar, are discussed. In section 6.7 the main results are reviewed.

6.1 The oxidation of $Ni_3Al(100)$ studied by AES

The $Ni_3Al(100)$ surface and its cleaning procedure have been already described in section 5.1. In this section we discuss the oxidation of $Ni_3Al(100)$ studied by AES. The oxidation experiments were performed by backfilling the UHV chamber with

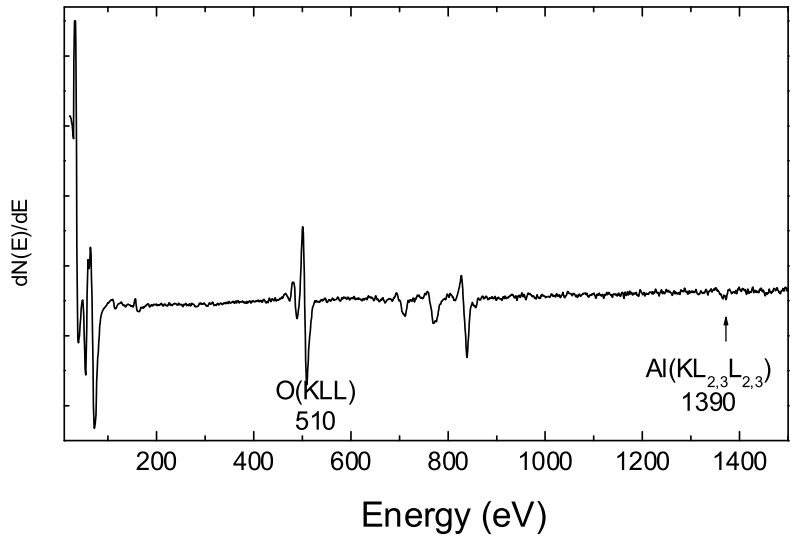

Figure 6.1: AES spectrum of $Ni_3Al(100)$ after oxidation at room temperature with 2000 L O_2 ($p < 10^{-7}$ mbar).

O_2 at different pressure ranges at 300 and 1100 K. Fig. 6.1 shows the AES spectrum of $Ni_3Al(100)$ after oxidation at room temperature with 2000 L O_2. In addition to the Ni and Al AES transitions, the O(KLL) transition is observed. Fig. 6.2a shows the evolution of the AES transition in the energy range between 30 and 100 eV for oxidation at 300 K at different oxygen exposures. The intensity of the Al^0 signal at 68 eV decreases after an exposure of only 5 L O_2. A new transition at $\sim$ 43 eV

occurs which is attributed to the formation of Al^{3+} ions. By increasing the oxygen exposure to 500 and 2000 L O_2, the AES signal increases and also a small signal at $\sim$ 37 eV appears which is also characteristic for the Al^{3+} ions. The development

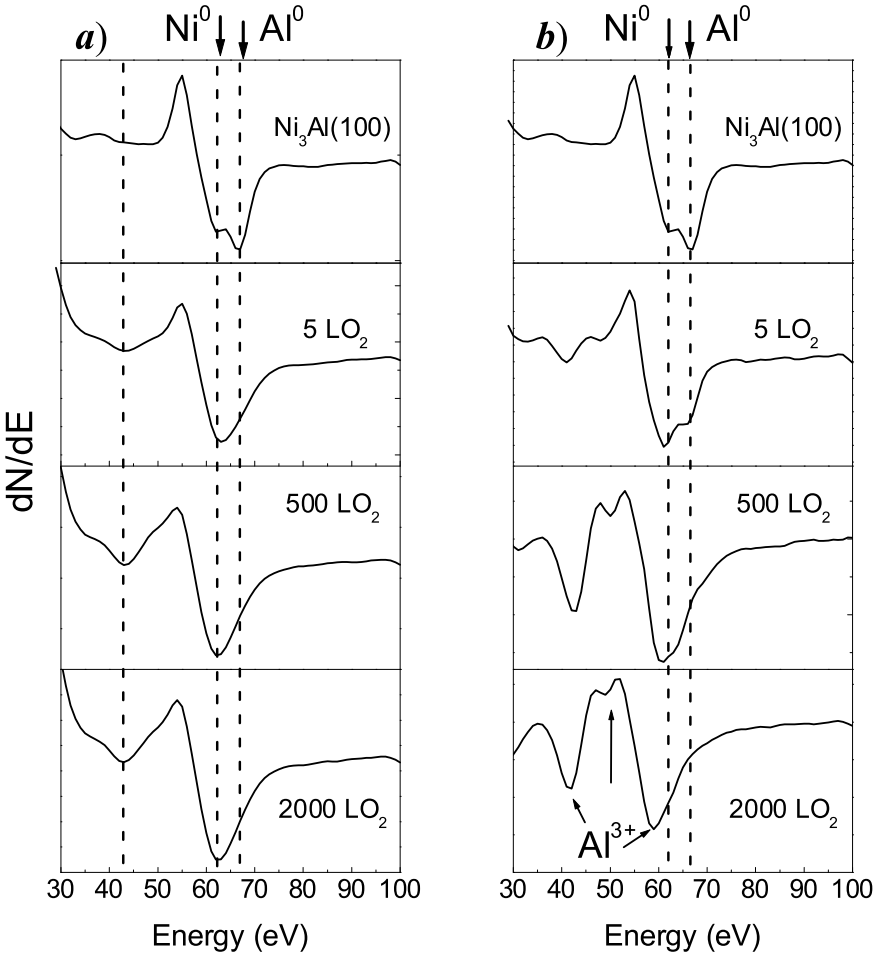

Figure 6.2: AES spectra as a function of oxygen exposures; (a) for oxidation at 300 K; (b) for oxidation at 1100 K.

of these two Al^{3+} signals at 37 and 43 eV indicates the oxidation of Al atoms in the surface region. Even in the room temperature oxidation regime, the thermal activation is sufficient to account for ion generation and movement [42]. Fig. 6.2b shows the evolution of Auger transitions during oxidation of the sample at 1100 K as a function of O_2 exposure. Already at very low exposure three new transitions

at 41, 49 and 59 eV appear. They are characteristic for Al^{3+}. This indicates that the Al atoms are involved in the oxidation process [82]. However, at low exposure the metallic Al^0 AES transition at 68 eV is still visible. This is consistent with an island growth mechanism of oxide which was also observed in STM experiments (see section 6.5). The island growth mode was also found by Bardi et al. with low energy ion scattering (LEIS) [81]. For the same exposure at 300 K it is not possible to observe clearly an Al^0 signal at 68 eV. May be at 300 K, the amorphous oxide is uniformly distributed over the surface, while at 1100 K the formation of Al-oxide islands allows a large part of Ni_3Al surface to remain oxide-free. However at 1100 K, for an oxygen exposure of 2000 L O_2, the signal at 68 eV can no longer be observed, which suggests that the whole surface is covered with oxide. After oxidation at 1100 K, the Al(KLL) transition at 1396 eV is shifted to 1390 eV which corresponds to the Al^{3+} (KLL) transition.

For further investigation of oxidation, we acquired oxygen uptake curves at 300 and 1100 K by analyzing the p-to-p ratio of the O (510 eV) intensity and the Ni(848 eV) intensity transitions as well as the p-to-p ratio between O (510 eV) intensity and Al(1390 eV) intensity. During the adsorption steps the oxygen partial pressure was adjusted between 3×10^{-8} and 1×10^{-7} mbar. The uptake curves for the adsorption at 300 and 1100 K are shown in Fig. 6.3. After a high initial growth rate, the thickening rate drops. At 300 K, the I_O /I_{Ni} ratio increases up to an exposure of 1000 L and then it remains constant at a value of 0.55. The behaviour at 1100 K is different, no saturation can be observed. For oxidation with 2000 L oxygen at 1100 K the ratio I_O /I_{Ni} amounts to ~ 1.2. This means that more oxygen is adsorbed on the surface due to a higher probability of aluminum segregation to the surface, at this temperature. The contribution of the thermal energy to the oxidation process is evidenced in this way. Another question which we want to address is: do we obtain a stoichiometric Al-oxide, and does it change with exposure? Fig. 6.3b shows the ratio between the p-to-p signal of oxygen (I_O) and aluminum (I_{Al}) at $\sim$ 1390 eV. For increasing oxygen exposure up to $\sim$ 250 L the ratio increase and for higher exposure

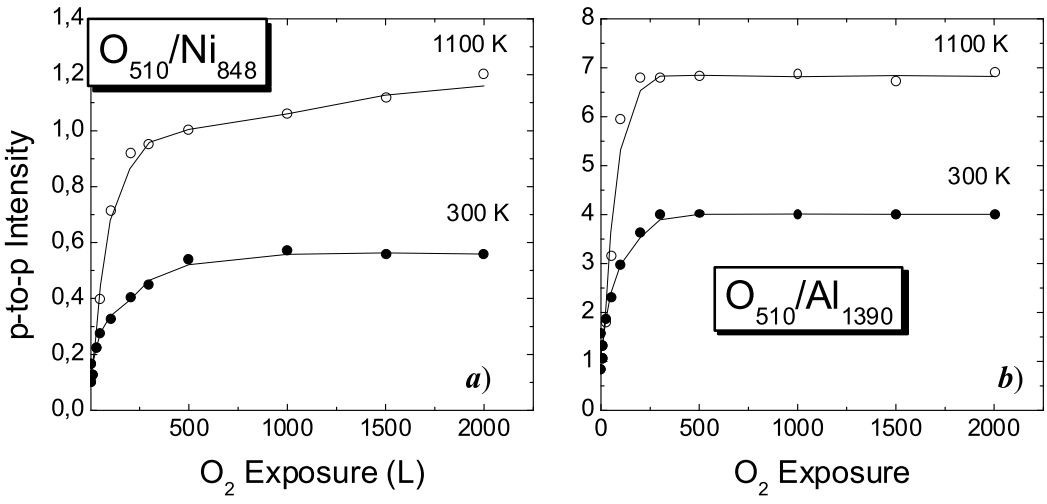

Figure 6.3: Oxygen uptake curves of oxidation at 300 and 1100 K; (a) $I_{O(510\ eV)}/I_{Ni(848\ eV)}$; (b) $I_{O(510\ eV)}/I_{Al(1396\ eV)}$ ($p < 10^{-7}$ mbar).

it remains constant in both cases. Above $\sim$ 250 L O_2, at 300 K the ratio amounts to $\sim$ 4, while at 1100 K a value of about 7 is found.

A rough estimation of the film thickness d was performed by analyzing the attenuation of the Ni(848 eV) signal due to the Al_2O_3 overlayer. We have used the formula:

$$I_{Ni} = I^0_{Ni} \cdot e^{\frac{-d_{Al_2O_3}}{\lambda_{Al_2O_3}(E_{Ni})\cos\theta}} \tag{6.1}$$

with a mean free path $\lambda_{Al_2O_3}$= 19 Å according to Ref. [83]. θ= 42° represents the acceptance angle of the CMA. The oxide film grown at 300 K with 2000 L O_2 has a thickness of $\sim$ 5 Å. The I_O /I_{Ni} ratio amounts to 0.55, while I_O /I_{Al} is $\sim$ 4. The thickness of oxide films grown with 2000 L oxygen adsorption at 1100 K is estimated to 10 Å $\pm$ 1 Å. For this thickness the I_O/I_{Ni} ratio is 1.2, while I_O /I_{Al} is $\sim$ 7.

At 300 K, the oxidation leads to the formation of an amorphous Al_2O_3 (a-Al_2O_3) film (see section 6.2 and 6.3) which has a thickness of 5 Å (at saturation). Therefore, some Al atoms from the substrate always contribute to the I_O /I_{Al} ratio and this value is below the expected value of stoichiometric Al_2O_3. At 1100 K we have to distinguish between two cases: at low exposure (< 250 L) some Al-oxide islands are

formed and a large part of the surface is oxide-free. In this case Al atoms from the oxide-free surface contribute also to the Al-signal and consequently the I_O /I_{Al} ratio is smaller than the stoichiometric value. However, when the whole surface is covered with Al-oxide at a final thickness of $\sim$ 10 Å(see Fig. 6.3b) the I_O /I_{Al} ratio should represents the correct value within the Al_2O_3 layer. This occurs for exposure above 250 L O_2 where the I_O /I_{Al} ratio is constant and amounts to $\sim$ 7, a value very close to that of stoichiometric Al_2O_3 [47].

6.2 The vibrational properties of Al_2O_3 films grown on $Ni_3Al(100)$

Fig. 6.4 shows two EEL spectra of $Ni_3Al(100)$ oxidized at 300 K with 1 and 1000 L O_2. The spectra exhibit two broad losses located at ν_a = 635 and ν_b = 850 cm^{-1}

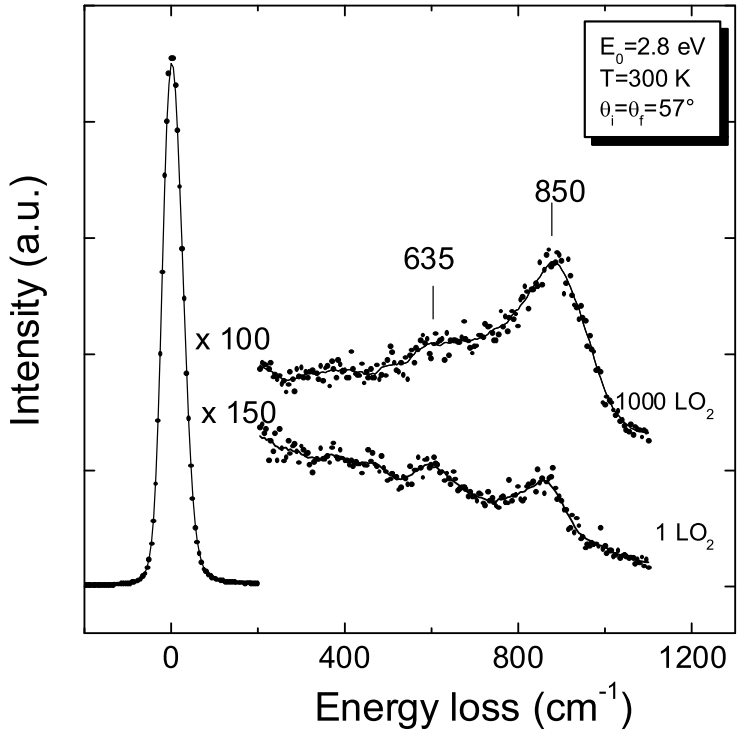

Figure 6.4: EEL spectra of the oxidized $Ni_3Al(100)$ at room temperature.

which are characteristic for amorphous Al_2O_3. With increasing oxygen exposure

	Frequencies of the losses (cm^{-1})				T(K)
a-Al_2O_3/NiAl(100)[82]		635		850	300
a-Al_2O_3/NiAl(110)[84]	419	621		847	300
a-Al_2O_3/NiAl(111)[37]		630		822	300
a-Al_2O_3/Ni_3Al(111)[85]		629		810	300
a-Al_2O_3/Ni_3Al(100)*		635		850	300
a-Al_2O_3/CoAl(100)*		650		890	300
θ-Al_2O_3/NiAl(100)[82]	420	603	718	896	1200
θ-Al_2O_3/CoAl(100)*	415	630		905	1000
γ-Al_2O_3/NiAl(110)[84]	425	635		880	1000
γ'-Al_2O_3/NiAl(111)[37]	427	637		887	1000
γ'-Al_2O_3/Ni_3Al(111)[85]	440	648		910	1000
γ'-$Al_2O_3Ni_3Al$(100)*	415	640		875	1100
α-Al_2O_3/NiAl(100)[82]			638	913	>1300
α-Al_2O_3/NiAl(111)[37]			630	911	>1100
α-Al_2O_3/CoAl(100)*			630	905	>1200
bulk-Al_2O_3[86]	500			800	
a-Ga_2O_3/CoGa(100)[41]	400		690		300
β-Ga_2O_3/CoGa(100)[87]	305	455	645	785	700

Table 6.1: The characteristic frequencies of the energy losses for some Al_2O_3 and Ga_2O_3 oxide phases on surfaces of intermetallic alloys (* present work).

the intensity of the loss at 850 cm^{-1} increases and at 1000 L O_2 it becomes much larger than that at 635 cm^{-1}. At saturation, the ratio of the relative intensities is $I(\nu_a)/I(\nu_b)$=2:3. The spectrum taken after an exposure of 1000 L O_2 is similar to those reported for amorphous Al_2O_3 films grown on Al(111) [88], NiAl(111)[37],

NiAl(100)[82], $Ni_3Al(111)$ [85]. Depending on the substrate, the frequencies of the losses are shifted to lower or higher values, but the loss structure is similar and was attributed to an amorphous Al_2O_3 (a-Al_2O_3) formed on the surface. Amorphous Al_2O_3 has a short range order and can be described as clusters of randomly oriented oxygen fcc lattices, with Al cations sitting in tetrahedral interstices [82]. Therefore,

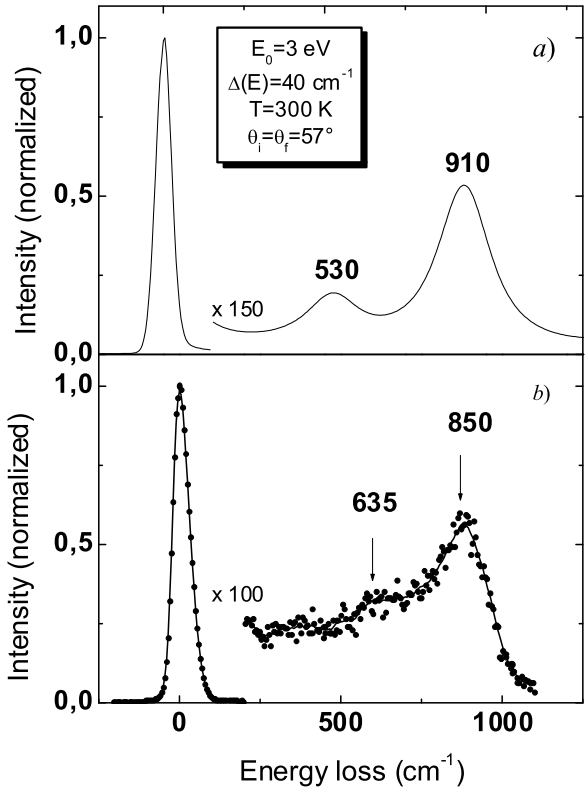

Figure 6.5: Comparison of (a) calculated and (b) experimental EEL spectra of amorphous alumina grown on $Ni_3(100)$.

it should rather be labelled vitreous instead of amorphous, which suggests a complete lack of order [82]. The table 6.1 shows an overview of the characteristic frequencies of the losses found in EELS experiments for amorphous and well-ordered Al_2O_3 and Ga_2O_3 grown on various substrates. As it is shown in this table, for amorphous Al_2O_3 (a-Al_2O_3) layers, always two losses are found in the frequency ranges between 620 and 640 cm^{-1} and between 810 and 850 cm^{-1}. There is only one exception, for

n	$\omega_{TO,k}$ cm^{-1}	S_k	$\gamma_k/\omega_{TO,k}$	$\omega_{LO,k}$ cm^{-1}
a-Al_2O_3 [49]				
ϵ_∞=2.8				
1	422	3.75	0.402	537
2	721	1.46	0.245	959
γ-Al_2O_3				
ϵ_∞=2.9				
1	357	2.52	0.202	403
2	536	2.38	0.189	669
3	744	0.34	0.076	783
4	807	0.17	0.054	917
$\hbar\omega_p$ =7.4 eV;				
γ =0.03 [89]				

Table 6.2: The values of the parameters used in the calculations of the EEL spectra.

Al_2O_3 formed at 300 K on NiAl(110), the EEL spectrum exhibits three losses [84]. This suggests that at 300 K a mixture of domains of a-Al_2O_3 and γ-Al_2O_3 coexists on NiAl(110). For a-Al_2O_3 (a-Ga_2O_3) only two modes are expected due to the solely tetrahedral coordination of the Al^{3+} (Ga^{3+}) ions. Two IR active modes are also predicted by the group theory. Thus we deduce that the spectra shown in fig. 6.4 originate from an amorphous aluminum oxide layer. To underpin the assumption of a-Al_2O_3 we have compared the measured spectrum with calculations for a model of an amorphous aluminum oxide layer on Ni_3Al. The parameters for a-Al_2O_3 [49] are given in Table 6.2. The calculations were done for different oxide thicknesses. The best agreement with the experimental spectrum is obtained for a thickness of $\sim$ 5 Å, in good agreement with the value determined from AES measurements. The spectra shown in Fig. 6.5 exhibits a good agreement between calculation and measurement regarding the relative intensities. However, the frequencies of the

calculated spectrum are shifted with respect to those of the experimental ones. While the frequency of the ν_b mode is shifted by about 60 cm^{-1} to a lower value, the

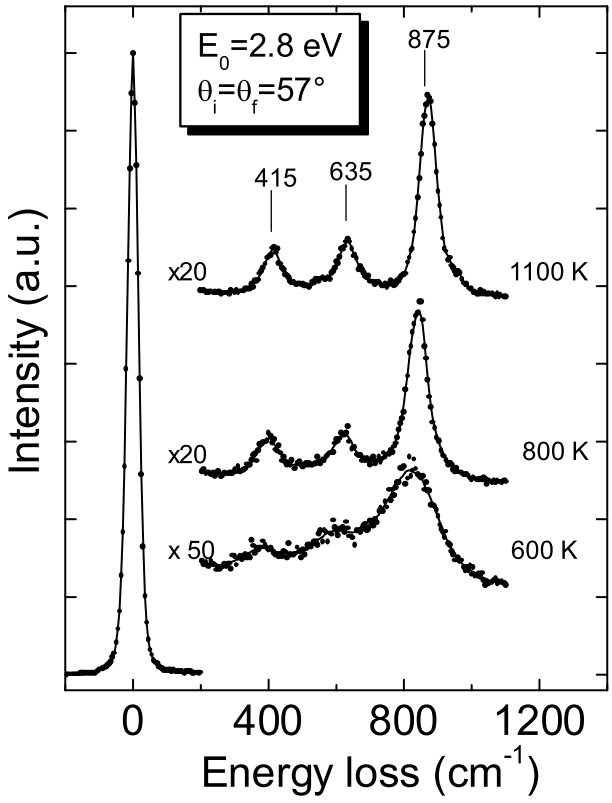

Figure 6.6: EEL spectra of the oxidized $Al_2O_3/Ni_3Al(100)$ as a function of annealing temperature. The sample was oxidized at 300 K with 2000 L O_2, I_O/I_{Ni}=0.55.

lower one (ν_a) is shifted with about 100 cm^{-1} to a higher frequency compared to the calculation. This may be due to different Al-O-Al bond angles and lengths within the AlO_4 tetrahedra. A similar effect was found for O/Si(111) [90]. Another reason could be the failure of the dielectric theory in producing the correct frequency of the surface phonons in the case of ultra-thin films (less than $\sim$ 2nm) [18].

After oxidation at room temperature with 2000 L O_2 the sample was annealed gradually, in steps of 100 K, up to 1100 K. Each annealing step lasted for about two minutes. Before the EELS measurements the sample was allowed to cool down to room temperature. As was already shown, the oxidation at room temperature leads

to losses at 635 and 850 cm^{-1}. After annealing at 600 K three new losses at 475, 635 and 875 cm^{-1} develop (Fig. 6.6). After annealing to 800 and 1100 K, the intensity of

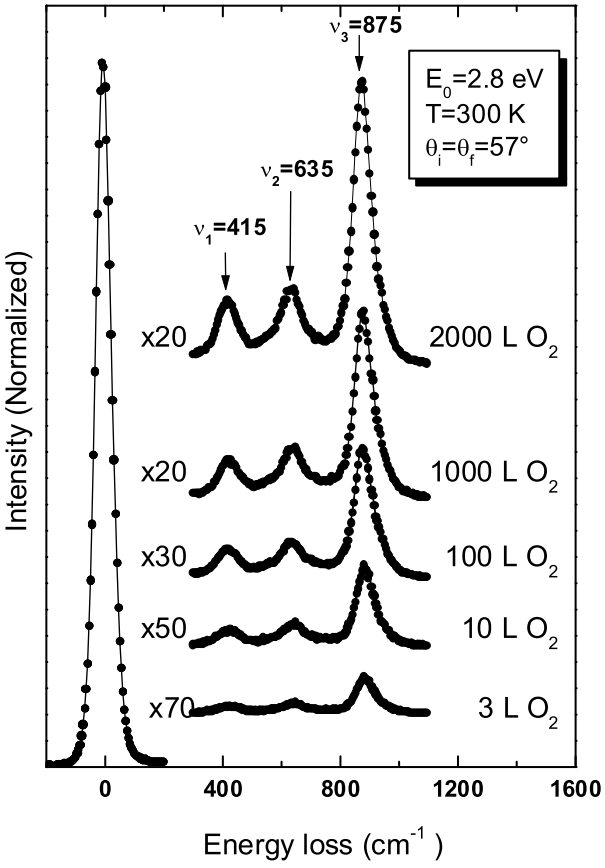

Figure 6.7: EEL spectra of the oxidized $Ni_3Al(001)$ at 1100K as a function of oxygen exposure (I_O/I_{Ni}=1.2 for 2000 L O_2).

the losses strongly increases (the magnification factor decreases from 100 at 300 K to 20 at 1100 K) and the FWHM of the peaks decreases. This shows that during annealing an ordering of the oxide film occurs. The three intense losses observed in the EEL spectra are attributed to the Fuchs-Kliewer (FK) phonon modes of a well-ordered Al_2O_3 layer. This indicates a transition from a-Al_2O_3 to a different phase of the oxide film, which involves an alteration of the occupation probability of the tetrahedral and octahedral sites in the aluminum sublattice. In γ-, γ'- and θ-Al_2O_3, the Al ions occupy both sites (tetrahedral and octahedral), whereas in a-Al_2O_3 only

the tetrahedral sites are occupied. Such intense FK modes are typical for insulating

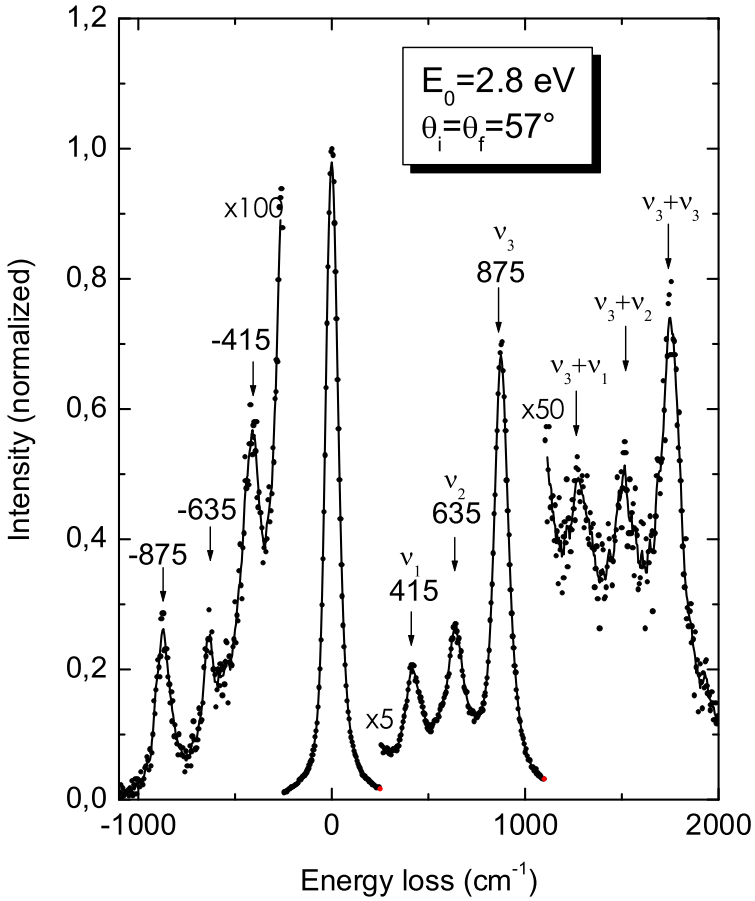

Figure 6.8: EEL spectrum of $Al_2O_3/Ni_3Al(100)$ after oxidation at 1100 K with 2000 L O_2. Three losses ν_1, ν_2 and ν_3 and the corresponding gains at -415, -635 and -875 cm^{-1} are observed. In addition the multiple excitation $\nu_3+\nu_1$, $\nu_3+\nu_2$ and $\nu_3+\nu_3$ are displayed.

or semiconductor thin layers [87]. For all the examples shown in Table 6.1 of well-ordered Al_2O_3 which are grown at elevated temperature on different substrates three optical modes (FK-phonons) are found in the frequency range of 420 - 440 cm^{-1} (ν_1), 602 - 650 cm^{-1} (ν_2), and 880 - 910 cm^{-1} (ν_1).

The group theory predicts for well ordered (γ-, γ'- and θ) aluminum oxide films 4 IR active modes. For example, in the case of θ-Al_2O_3/NiAl(100) and β-Ga_2O_3/CoGa(100)

(which are isomorphic) four FK modes are found (see table 6.1). However for our film, the fourth mode (between the 635 and 875 cm^{-1} modes) was not detected. It may be, the intensity is very small due to a specific structure of the aluminum oxide or its frequency is shifted to higher or lower values and consequently it is superposed with those of the strong neighbor losses. The fourth loss was also not observed in the case of γ'-Al_2O_3/$Ni_3Al(111)$ [85]. The high degree of order of the oxide film is confirmed by the LEED and STM investigations which will be presented in the next sections.

Fig. 6.7 shows the EEL spectra of $Ni_3Al(100)$ surface after oxidation at 1100 K as a function of oxygen exposure. Already for an exposure of 3 L O_2 three losses at 415, 640 and 875 cm^{-1} can be observed. With increasing oxygen exposure the intensity of the three losses increases and the FWHM decreases. The frequencies of these losses are equal to those observed after annealing an a-Al_2O_3 film to 1100 K, which suggests that the same Al_2O_3 phase is formed on the surface. The frequency of the vibrational losses are close to those obtained for γ'-Al_2O_3 grown on NiAl(111) (losses at 427, 637 and 887 cm^{-1}) [37]. Becker et al. [85] found a similar spectrum in the case of γ'-Al_2O_3 on $Ni_3Al(111)$ with the losses at 440, 647 and 909 cm^{-1}. Fig. 6.8 shows an EEL spectrum of $Ni_3Al(100)$ after oxidation at 1100 K with the losses ν_1, ν_2 and ν_3 and the corresponding multiple losses at $\nu_3+\nu_1$, $\nu_3+\nu_2$ and $\nu_3+\nu_3$ and gain peaks ($-\nu_1$, $-\nu_2$ and $-\nu_3$). The intensity of the losses and gain peaks at - 415, - 635 and - 875 cm^{-1} is related to the Boltzmann statistics: $I_g = I_l \exp(-\hbar\omega/kT)$(g:gain, l:loss).

In order to confirm the Al_2O_3 phase of the film, EEL spectra were calculated on the basis of the dielectric theory and were compared to the experimental spectra. The calculations were performed using a program [17] which allows to simulate the EEL spectrum for electrons specularly reflected at the surface. The parameters used for the simulation of the EEL spectra of well-ordered γ-Al_2O_3 are taken from reference [49] and they are listed in Table 6.2. The Ni_3Al substrate is represented through a Drude term with $\omega_p = 7.4$ eV [89]. The calculations were performed for

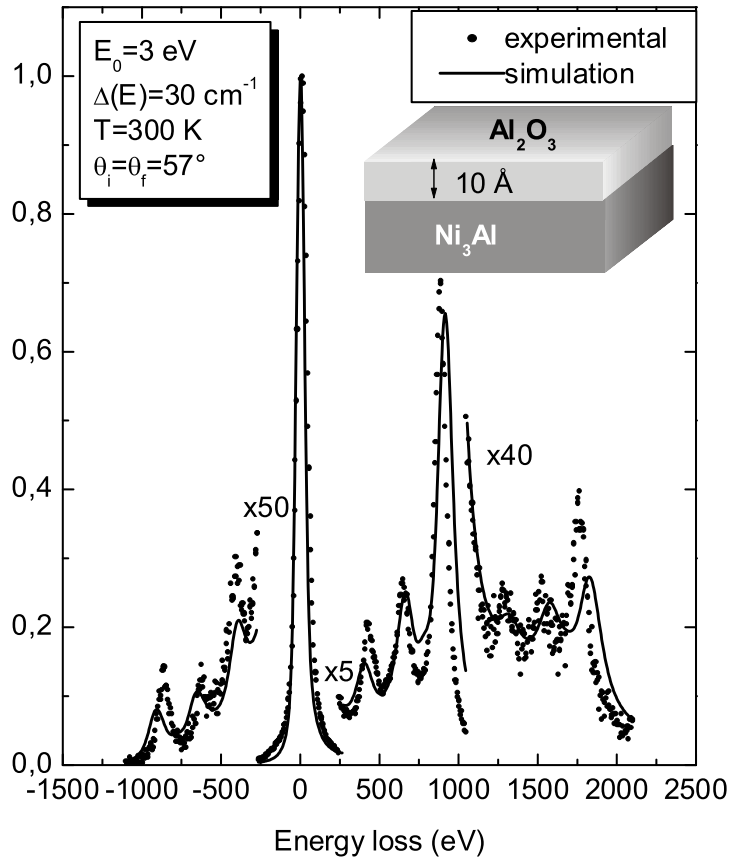

Figure 6.9: Comparison of the calculated (solid line) and experimental (dots)EEL spectra of γ'-Al_2O_3/$Ni_3Al(100)$; the best agreement was achieved for a layer thickness of 10 Å. Inset: a model of the Al_2O_3 on top of $Ni_3Al(100)$.

different oxide thickness. The calculated spectrum is represented in Fig. 6.9 (solid line). All losses are nicely reproduced concerning the relative loss intensity and loss energy. The three visible modes are the ω_+ branches within the thin oxide layer close to the ω_{LO} bulk values. The ω_- branches are screened by the metallic substrate. The best agreement between the calculated and the measured spectra has been achieved for a thickness of 10 Å of oxide film. This value has to be considered only as an approximate, taking into account the number of parameters used for calculation. However, it is very close to the thickness estimated from AES data.

6.3 The structure of the Al_2O_3 layer grown at 1100 K on $Ni_3Al(100)$

Starting from the (1×1) pattern of the clean surface the spots became more and more diffuse with increasing oxygen exposure at 300 K. At the saturation level the

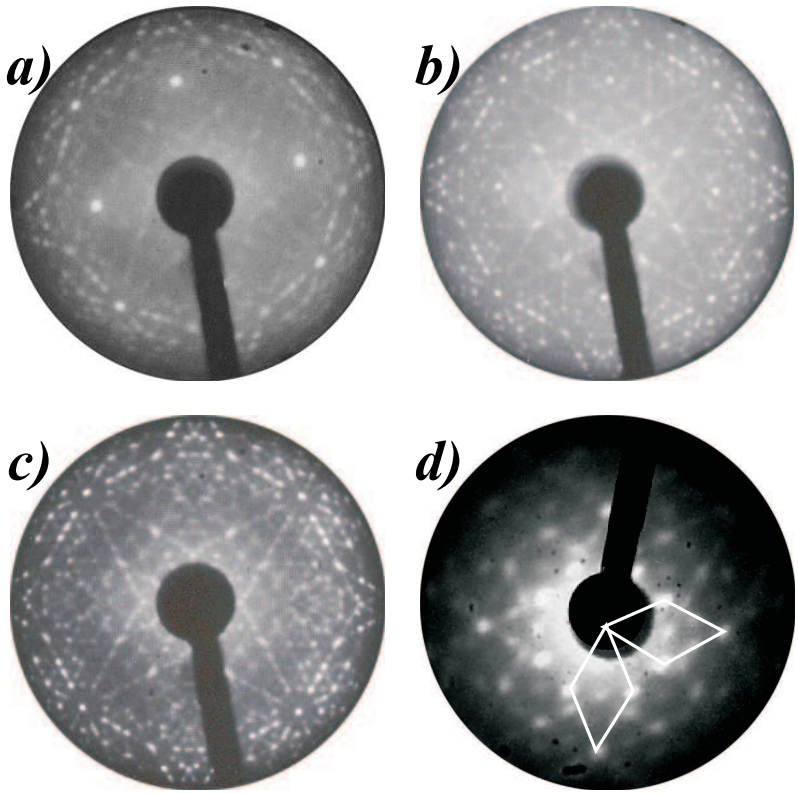

Figure 6.10: (a)LEED pattern of the $Ni_3Al(100)$ surface after oxidation at 1100 K at: (a) 1 L O_2 (E_p=65 eV); (b) 20 L O_2 (E_p=65 eV); (c) 2000 L O_2 (E_p=65 eV); (d) same condition as (c) (E_p=10 eV).

substrate spots vanish completely and the LEED screen exhibits diffuse illumination. The surface seems to be highly disordered and has lost long-range order at least on the first few layers. After annealing the oxidized sample at 1100 K a LEED pattern with very sharp spots appears, which implies that we are dealing with a well-defined, long-range ordered structure. A similar LEED pattern is obtained

when the $Ni_3Al(100)$ surface is directly oxidized at 1100 K. Fig. 6.10a shows the LEED pattern of the $Ni_3Al(100)$ surface oxidized at 1100 K with 1 L O_2. At this exposure the substrate spots are still clearly visible.

After oxidation with 20 L O_2 (Fig. 6.10b) the intensity of the substrate spots is diminished, however they are still recognizable. This is consistent with the island growth mechanism observed in STM (see section 6.5). At 2000 L O_2 the substrate LEED spots are not visible and the LEED pattern exhibits only the oxide pattern (Fig. 6.10c). At low exposure, the LEED pattern originates from oxide islands and from areas of the substrate free of oxide, while at higher exposure, when the substrate is completely covered with oxide, the pattern is given entirely by the oxide. A similar LEED pattern was observed by Bardi et al. [81] and was explained by a quasi-hexagonal structure with a lattice constant of about 3 Å and the substrate unit cell with a lattice constant of 3.57 Å (see fig. 6.11a, b; the basis vectors of the substrate are denoted by $\vec{a}_1$ and $\vec{a}_2$, and the basis vectors of the oxide with $\vec{c}_1$ and $\vec{c}_2$). Most of the extra-spots were attributed to multiple diffraction effects. The agreement of the lattice constant estimated from LEED with the length of the basis vectors along the (111) plane of γ'-Al_2O_3 suggests that the oxide grows with the (111) plane parallel to the substrate surface plane. The structure of the γ'-Al_2O_3 is derived from that of γ-Al_2O_3 and it has half of the unit cell of γ-Al_2O_3 [91, 92, 81]. A part of the spots in figure 6.10c may be indexed in terms of a hexagonal oxygen unit mesh with a lattice constant of 3 Å. The unit vector length of 3 Å is approximately twice the value of the O^{2-} radius (1.4 Å). This implies that the top layer of the alumina film consists of compact hexagonal planes of oxygen ions.

Our analysis give a slightly different interpretation of the LEED pattern, which does not excludes but fulfills Bardi's interpretation. The reason is the observation of a LEED pattern at 10 eV (Fig. 6.10d), where a twelvefold ring structure can be recognized. This pattern can not be explained only on the basis of a hexagonal structure with a lattice constant of $\sim$ 3 Å whose diffraction pattern can not be observed at such a low energy.

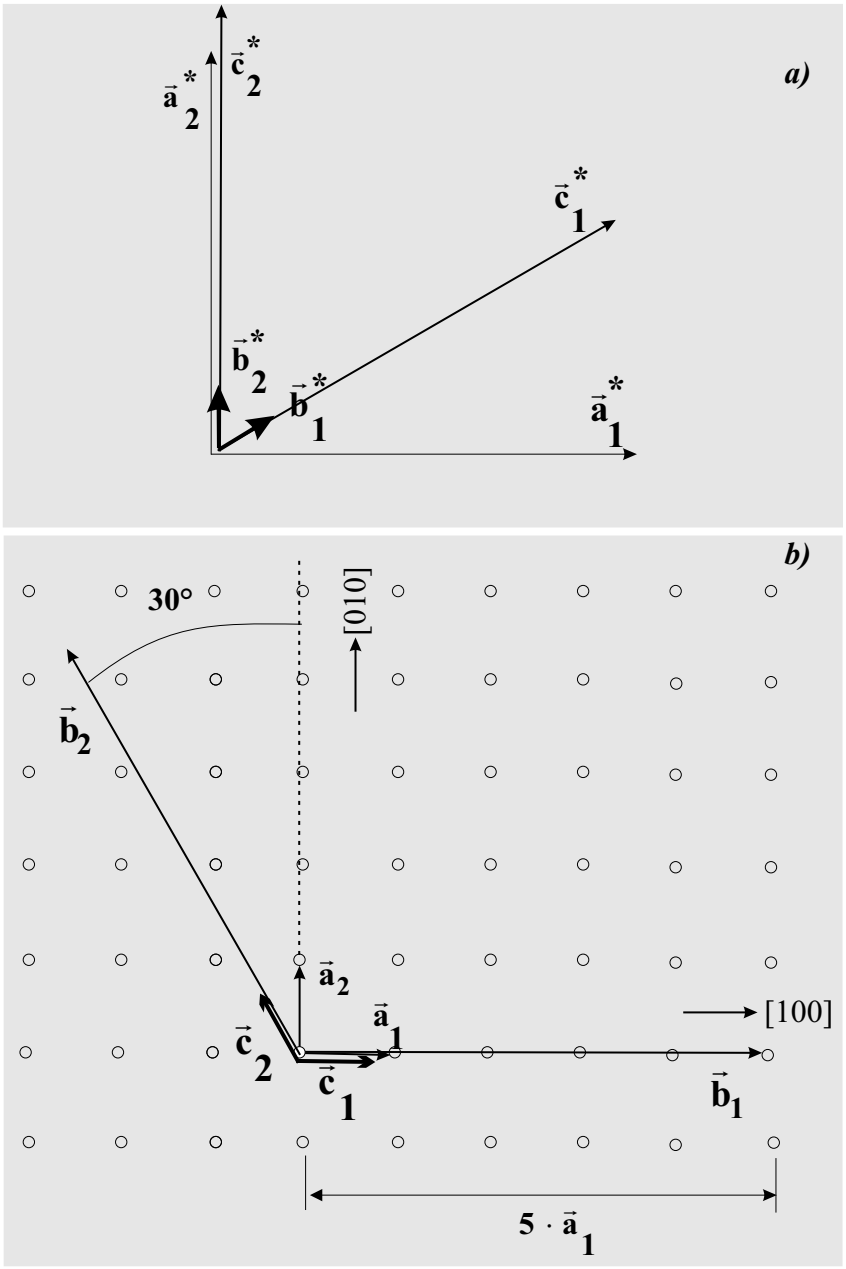

Figure 6.11: (a) The reciprocal vectors of the substrate ($\vec{a}^*_1$, $\vec{a}^*_2$), of the superstructure ($\vec{b}^*_1$, $\vec{b}^*_2$) and of the oxygen lattice ($\vec{c}^*_1$, $\vec{c}^*_2$); b) The real space representation; ($\circ$) represents the atoms in the first layer of $Ni_3Al(100)$; $\vec{a}_1$, $\vec{a}_2$ are the basis vectors of the substrate; $\vec{b}_1$, $\vec{b}_2$ are the basis vectors of the superstructure; ($\vec{c}_1$, $\vec{c}_2$) are the basis vectors of the oxygen lattice.

The LEED pattern in figure 6.10d is explained by a hexagonal structure with two domains which are rotated by 90° with respect to each other. The basis vector of the hexagonal structure amounts to $\sim$ 18 Å. The unit mesh of the hexagonal structure in the reciprocal space is sketched in figure 6.10d by the rhombs. Fig. 6.11a shows the relative orientation of the basis vectors of the substrate ($\vec{a}_1^*$, $\vec{a}_2^*$), of the superstructure ($\vec{b}_1^*$, $\vec{b}_2^*$) and of the compact hexagonal oxygen lattice vectors ($\vec{c}_1^*$, $\vec{c}_2^*$) in the reciprocal space. Fig. 6.11b shows the basis vectors of the superstructure ($\vec{b}_1$, $\vec{b}_2$) and the basis vectors of the substrate ($\vec{a}_1$, $\vec{a}_2$). In addition the basis vectors of the compact hexagonal oxygen top layer, ($\vec{c}_1$, $\vec{c}_2$), used also by Bardi et al. are indicated. For clarity only the basis vectors for one domain are sketched. The lattice constant found for the superstructure (18 Å) coincides almost with a multiple of the lattice constant of the substrate, i.e 5×3.57=17.85 Å. If we consider, for example, one basis vector of the superstructure ($\vec{b}_1$) lying in the [100] direction of the substrate the lattice mismatch amounts to 1%. The coincidence is not surprising because the alumina film is ultra-thin and therefore a coincidence structure of a slightly distorted hexagonal structure of the alumina film and the substrate seems to be favorable. In the direction of the second unit mesh vector of the hexagonal superstructure ($\vec{b}_1$) no coincidence with the substrate is found. The matrix which relates the superstructure periodicity to that of the substrate is:

$$\begin{pmatrix} \vec{b}_1 \\ \vec{b}_2 \end{pmatrix} = \begin{pmatrix} 5 & 0 \\ -2.52 & 4.36 \end{pmatrix} \cdot \begin{pmatrix} \vec{a}_1 \\ \vec{a}_2 \end{pmatrix} \tag{6.2}$$

where the $\vec{b}_1$ and $\vec{b}_2$ are the basis vectors of the superstructure and $\vec{a}_1$ and $\vec{a}_2$ the vectors of the substrate. The vectors ($\vec{c}_1$ and $\vec{c}_2$) are related to those of the substrate by:

$$\begin{pmatrix} \vec{c}_1 \\ \vec{c}_2 \end{pmatrix} = \begin{pmatrix} 0.84 & 0 \\ -0.42 & 0.72 \end{pmatrix} \cdot \begin{pmatrix} \vec{a}_1 \\ \vec{a}_2 \end{pmatrix} \tag{6.3}$$

For the second domain of the alumina film, which is rotated by 90° with respect to the first one, a similar coincidence in the [010] direction exists with the same

lattice mismatch of ~ 1 %. The origin of this coincidence structure could be a reconstruction of the $Ni_3Al(100)$ surface induced by the alumina layer on the top of it. Most of the alumina surface phases have a hexagonal or nearly hexagonal surface mesh. The unit vector lengths range from 2.9 to 3.1 Å which is approximately twice of the value of the O^{2-} ionic radius. This suggests that the observed unit meshes always correspond to compact hexagonal planes of oxygen ions. The lattice constant of the quasi-hexagonal structure, 18 Å, almost coincides with a multiple (6×3 Å=18 Å) of the unit vectors of a hexagonal surface mesh (hexagonal plane of oxygen ions) of alumina. Thus, the surface of the alumina film could be reconstructed to give a quasi-hexagonal superstructure. Several surface reconstructions of alumina have been observed: e.g., depending on the thermal treatment, the surface of α-$Al_2O_3(0001)$ is reconstructed [93]. A similar situation could also occur in the case of the oxidation of $Ni_3Al(100)$.

6.4 The band-gap of $Al_2O_3/Ni_3Al(100)$

Fig 6.12 (a) and (b) show the loss features up to 10 eV for films of amorphous and well-ordered alumina grown on $Ni_3Al(100)$, respectively. The spectra were recorded using a primary energy of 32 eV. In order to gain intensity, a relatively poor energy resolution and long integration times were chosen. The elastic beam, and the vibrational losses are not shown (i.e. losses below 0.2 eV). The spectrum of the a-Al_2O_3 shows a shoulder at 0.7 eV and a broad loss feature with an onset of ≈ 3.2 eV. In the case of the well-ordered Al-oxide, the broad feature starts at ~ 4.3 eV. The increase of the background is due to the excitations of electrons from the valence band (VB) into the conduction band of the oxide. The loss probability is proportional to the joint density of states, disregarding the matrix elements effects [82]. Using a very coarse approximation of parabola around the maximum (minimum) of the valence (conduction) band the loss probability is proportional to $\Theta(\hbar\omega - E_g)\sqrt{\hbar\omega - E_g}$ (with the Heavyside step function Θ). Fitting our data with

this function yields $E_g \approx 3.2$ eV for a-Al_2O_3 and $E_g \approx 4.3$ eV for the well-ordered oxide film. The band-gap of the bulk γ-Al_2O_3 has a value of 8.7 eV [94]. The energy

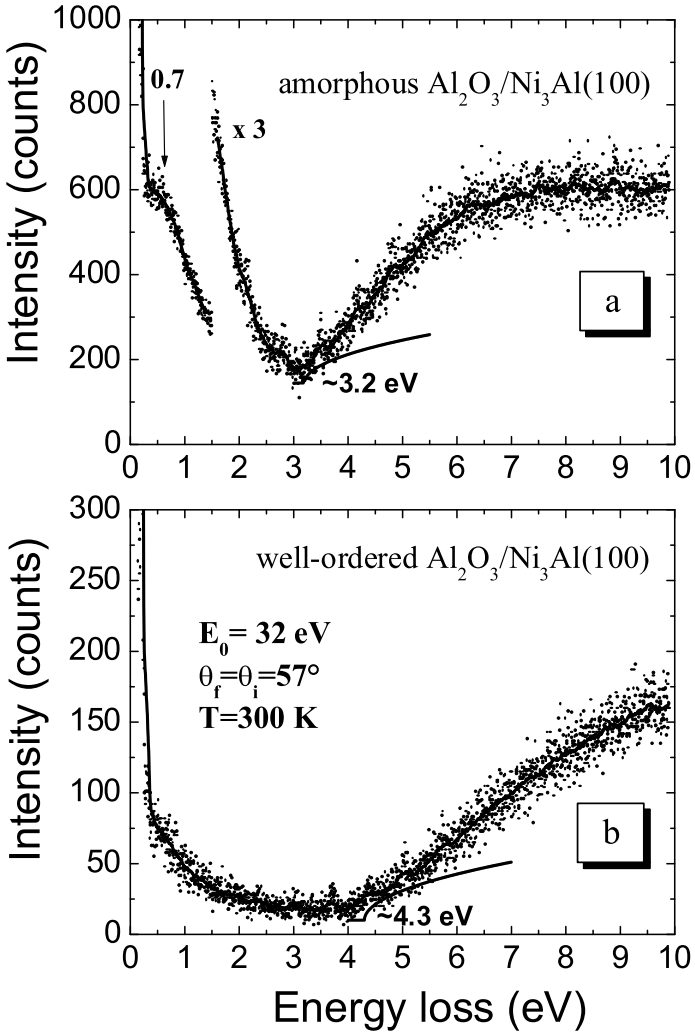

Figure 6.12: The band gap of $Al_2O_3/Ni_3Al(100)$: (a) for a-Al_2O_3 formed at 300 K; (b) for Al_2O_3 prepared at 1100 K.

band-gap which we found for the amorphous and well-ordered Al_2O_3 has a lower values with respect to the bulk. In order to understand the decreasing of band-gap value, we have to make some remarks concerning the interband transitions. For an one-electron model, neglecting the relaxation effects in photoemission transition or excitonic effects in interband transitions, the interband transition can be described

as an electronic excitation from bound state (valence or core) to an unoccupied state located in the conduction band [95]. The onset of the broad energy losses in an EEL spectrum can be associated with an interband transition. If the energy losses are lower than the energy gap, this can be interpreted as electronic transitions between valence band and unoccupied states located in the band-gap [96]. The band-gap of thin alumina film was a subject of discussion particularly in the case of thin Al_2O_3 films [97, 96]. The decrease of the energy band-gap value reported for thin α-alumina [93, 98] and γ-alumina [97] was explained in terms of the appearance of a metallic characteristic in the alumina surface layers [93] or due to some defects levels located in the band-gap [96]. Such defect states were found also in Al_2O_3 film grown on Al(111) and they were related to intermediate Al oxidation states [99]. This hypothesis is supported also by DOS calculations of Ciraci et. al. [100] which obtained empty energy levels located in the band-gap supposing the existence of ideal vacancies in Al_2O_3. In ref. [96] the authors show that the band-gap for thin γ-Al_2O_3 film is dramatically reduced up to 2.6 eV. The appearance of the empty levels induced by defects located in the band-gap is considered as a reason for the decrease of the band-gap value. The dangling Al spz bonds at the surface are also responsible for the existence of a discrete level located below the conduction band minimum energy. Taking in the account this small value of band-gap the authors do not consider anymore the γ-Al_2O_3 thin film as an insulator, but as a new phase with different properties characterized by the decrease of the ionicity of the oxygen sites. In the case of the reconstructed surface of α-Al_2O_3(0001) [93] the band-gap is also found to be smaller than it's bulk value. In this case no empty levels are detected in the band-gap. In the case of θ-Al_2O_3 formed on NiAl(001), the authors [101] have found a band-gap value of about 7.4 eV which is also diminished with respect to the value for the bulk. In our studies a broad loss feature in the EEL spectra starts at about 3.2 eV for the amorphous Al-oxide and at 4.3 eV for the well-ordered Al-oxide. In case of an ideal, defect-free crystalline insulator, the intensity should increase abruptly at the energy gap. In contrast, in our experiments

these sharp edges are not present. However, the energy levels induced by defects, which are located in the band-gap, diminish the band-gap energy. In amorphous semiconductors, it was also found, that a distribution of tail states encroaches into the otherwise empty band-gap region [102]. The analysis shows that tail states are localized by the site disorder and they are responsible for many of unique properties exhibited by amorphous semiconductors [103, 104].

6.5 The morphology of $Al_2O_3/Ni_3Al(100)$

In this section we present the STM experiments performed on Al_2O_3 grown on $Ni_3Al(100)$. The STM provides informations about the surface topography in real space, which is important in order to understand the growth mode of thin alumina film. The STM images were acquired in the constant-current topography (CCT mode). All STM images were recorded in a differential mode to ensure image reproduction of different topographic heights at reasonable grey levels. The analysis of the images (line scans etc.) was made after integration. Since Al_2O_3 is a wide band-gap insulator tunnelling into empty or from filled states of the oxide film is, in principle, only possible by using a sufficiently large bias voltage [105, 106]. As shown in section 6.4, the band-gap of thin Al_2O_3 is about 4.3 eV. If we assume the Fermi level E_F to be located near to the center of the band gap, direct electronic contribution from the oxide are expected for U $\leq$ -2 or U $\geq$ 2V [107]. However, during the STM experiments it was evidenced that the oxide can be imaged also for smaller voltage. One can suppose that the surface states located in the band-gap are responsible for tunneling, as it was pointed out in the case of β-Ga_2O_3/CoGa(100) [107]. In our STM experiments the sample is grounded. A positive bias of the tip leads to the tunnelling from the filled states of the sample (e.g. valence band of oxide) to the empty states of tip, while negative voltage leads to the tunnelling from the filed states of tip to the empty states of the sample (e.g. conduction band of oxide).

Figure 6.13a shows a STM image with a scanned area of 510×510 Å^2 of the $Ni_3Al(100)$

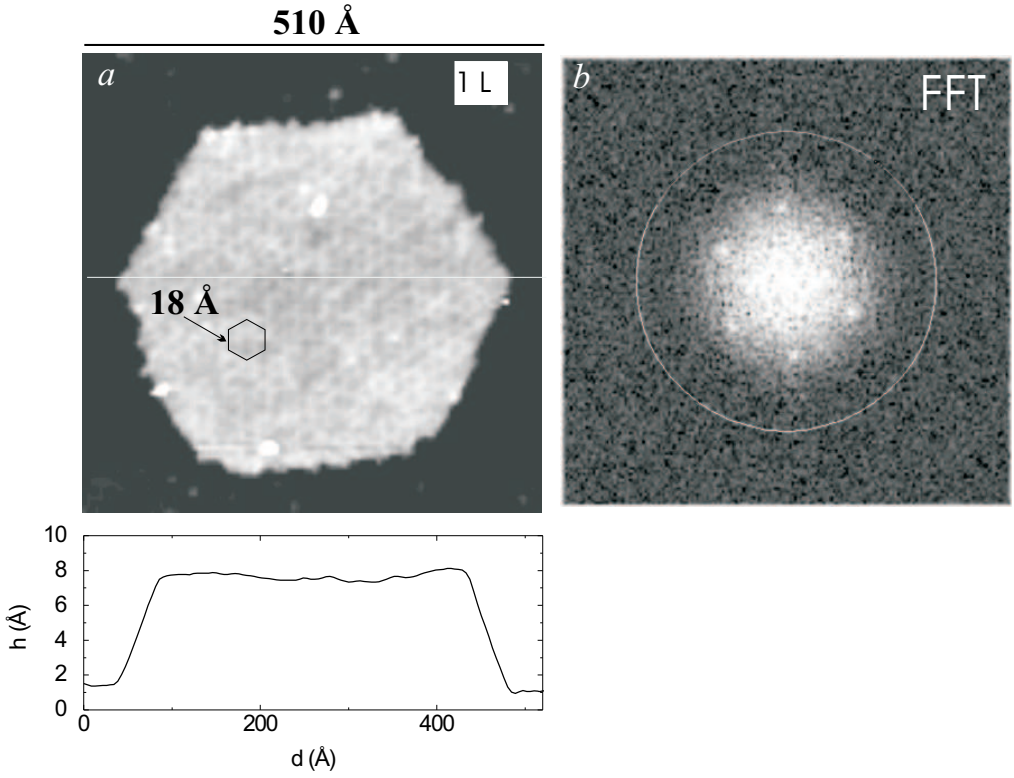

Figure 6.13: (a) STM image of $Ni_3Al(100)$after exposure to 1 L O_2 at 1100 K ($U_t = 2$ V; $I_t = 0.3$ nA); On the Al_2O_3 island a hexagonal superstructure is visible. (b) Fast-Fourier transform of the island image confirming the hexagonal superstructure.

surface oxidized with 1 L O_2. One oxide island with hexagonal shape can be observed. The side length of the hexagon amounts to $\sim$ 200 Å. The line scan taken over the island reveals an apparent height of about 6 Å. As it was pointed out in the case of β-Ga_2O_3/CoGa [107] the determination of the height from STM images when one scan over different species (metal-oxide-metal) has to be critically interpreted. The height in STM is given by the gray level contrast which depends on the density of states at the Fermi level. Consequently, the determination of the height for domains with different electronic structures does not reproduce necessarily the geometric height [108, 109]. In addition, the apparent height of the film shows a clear bias dependence [106, 110] and depends also on the current [109], as well as on the distance between the tip and the sample [111]. On the top of the island

a quasi-hexagonal superstructure with a periodicity of $\sim$ 18 Å can be recognized. This result is in agreement with the LEED pattern (fig. 6.10c and d) which was explained by a hexagonal superstructure with a lattice constant of 18 Å. Fig. 6.13b shows a Fast-Fourier transform of the STM image on the top of the island which confirms the quasi-hexagonal structure. A similar superstructure was observed in

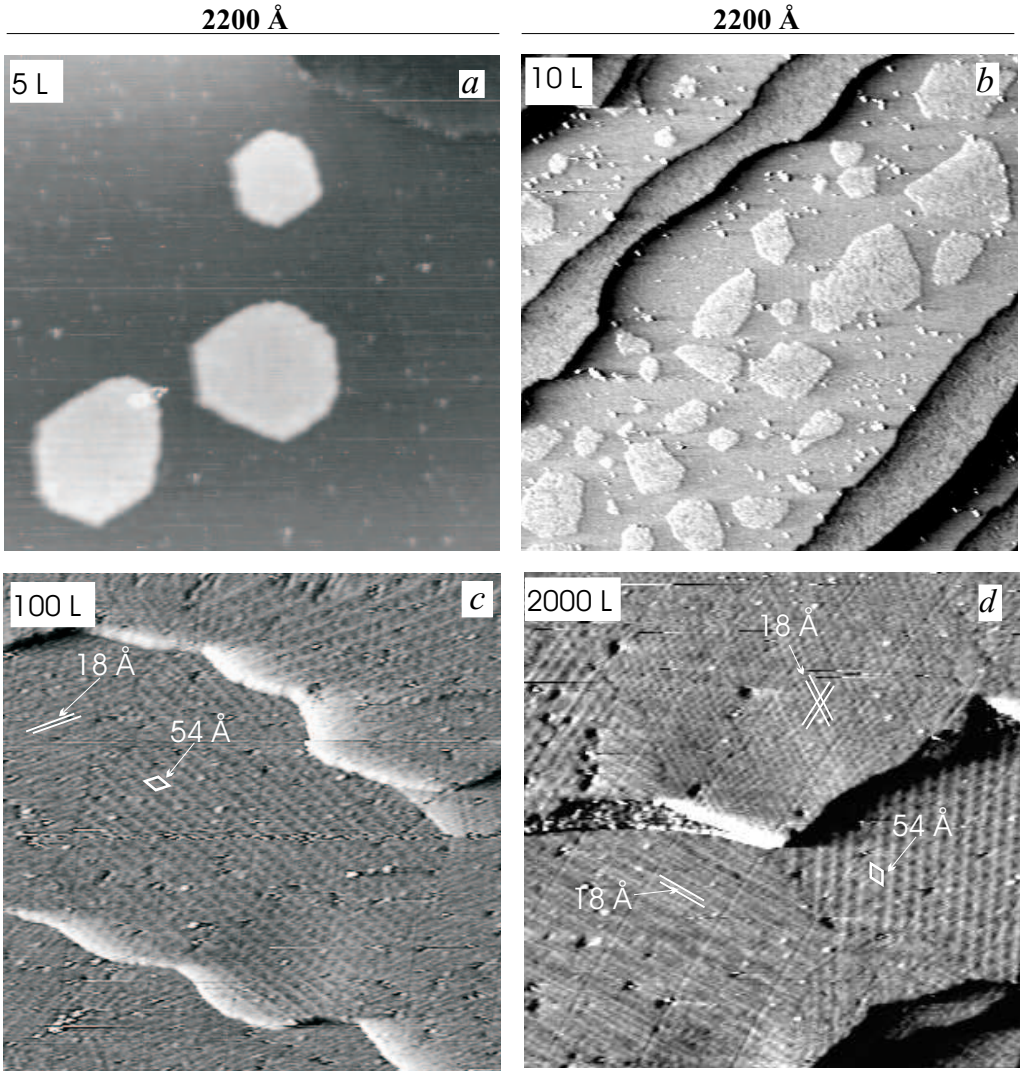

Figure 6.14: STM images of $Ni_3Al(100)$ after oxidation at 1100 K with (a) 5 L O_2 (U_t = 2 V; I_t = 0.3 nA); (b) 10 L O_2 (U_t = 2 V; I_t = 0.3 nA); (c) 100 L O_2 (U_t = 2.5 V; I_t = 0.2 nA) and (d) 2000 L O_2 (U_t = -4.5 V; I_t = 0.2 nA).

STM experiments performed on Al_2O_3 grown on $Ni_3Al(111)$ [85]. In the case of $Al_2O_3/Ni_3Al(111)$ the authors have identified the superstructure as a Moiré pattern which is a modulated pattern resulting from the superposition of the oxide structure with that of the substrate. In this case, the islands have a triangular shape which is associated with the substrate symmetry that allows a specific configuration of domains.

Fig. 6.14 shows STM images of $Ni_3Al(100)$ oxidized with various O_2 exposure at 1100 K. Fig. 6.14a-d show different scanned areas on the surface. The reason for this is that for oxidation at 1100 K, the STM has to be removed from the sample and after cooling the sample to 300 K the same position on the sample cannot be found.

In Fig. 6.14a is shown a STM image with a scanned area of 2200 $\times$2200 Å^2 after oxidation at 1100 K with 5 L O_2. Three islands with hexagonal-shape are visible on the same terrace. The density of islands increases after oxidation with 10 L O_2. In this case not all islands have a hexagonal shape. It may be, they are formed through a coalescence of the former hexagonal islands (Fig. 6.14b). After oxidation with 100 L O_2 the whole surface is covered with oxide and no isolated islands are visible (Fig. 6.14c). The surface shows large terraces with steps with a height ($\sim$ 3 - 4 Å) close to that of the substrate. This could be interpreted as a homogeneously

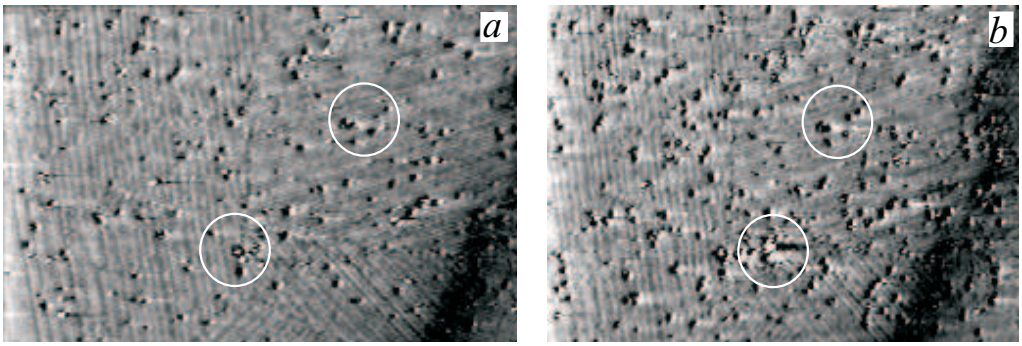

Figure 6.15: Two successive STM constant current (4V, 0.2nA) images of a region of the $Al_2O_3/Ni_3Al(100)$ (1700$\times$800 Å). The $Ni_3Al(100)$ was exposed to 2000 L O_2.

growth of the oxide film on different terraces. In addition to the superstructure with the periodicity of $\sim$ 18 Å (indicated by the parallel streaks) observed at low exposure (fig 6.13b), another hexagonal superstructure, with a lattice constant of $\sim$ 54 Å is visible. Both superstructures are visible not only on different terraces but also on the same terrace as it is shown in Fig. 6.14c. Further oxidation at 1100 K with 2000 L O_2 does not change very much the surface morphology (Fig. 6.14d). The two superstructures, found already after the oxidation with 100 L O_2, are visible. We have already mentioned that the lattice constant b_1 of the hexagonal superstructure coincides with a multiple (6×3 Å) of the basis vector c_1 of the compact hexagonal plane of oxygen ions in the γ'-Al_2O_3 lattice. May be this is accidental, but the basis vector of the second superstructure (54 Å) is also a multiple (18×3 Å) of c_1 and therefore also a multiple (3×18 Å=54 Å) of b_1.

Another peculiarity is faced during the STM scanning of the Al_2O_3 surface with a relatively high bias voltage of the tip. Fig. 6.15a and b shows the same place of the surface after successive scanning. The number of dark hole-like defects in Fig. 6.15b (second scanning) is much higher than in Fig. 6.15a (first scanning). The density of defects after the first scanning is 2.5×10^{11} defects/cm^2 and 4.2×10^{11} after the second scanning. Close examination of the pictures shows that new defects appear mostly in the vicinity of already existing defects. Similar STM induced voids were obtained on $Al_2O_3/Ni_3Al(111)$ [112]. The void formation was explained by dielectric breakdown.

6.6 The oxidation at 1100 K in the 10^{-6} mbar pressure range

The oxidation of $Ni_3Al(100)$ at 1100 K was carried out also at a higher oxygen pressure (5×10^{-6} mbar). A comparison with the results at 10^{-7} mbar shows, for the same exposure, a more advanced growth. This can be observed very clearly in

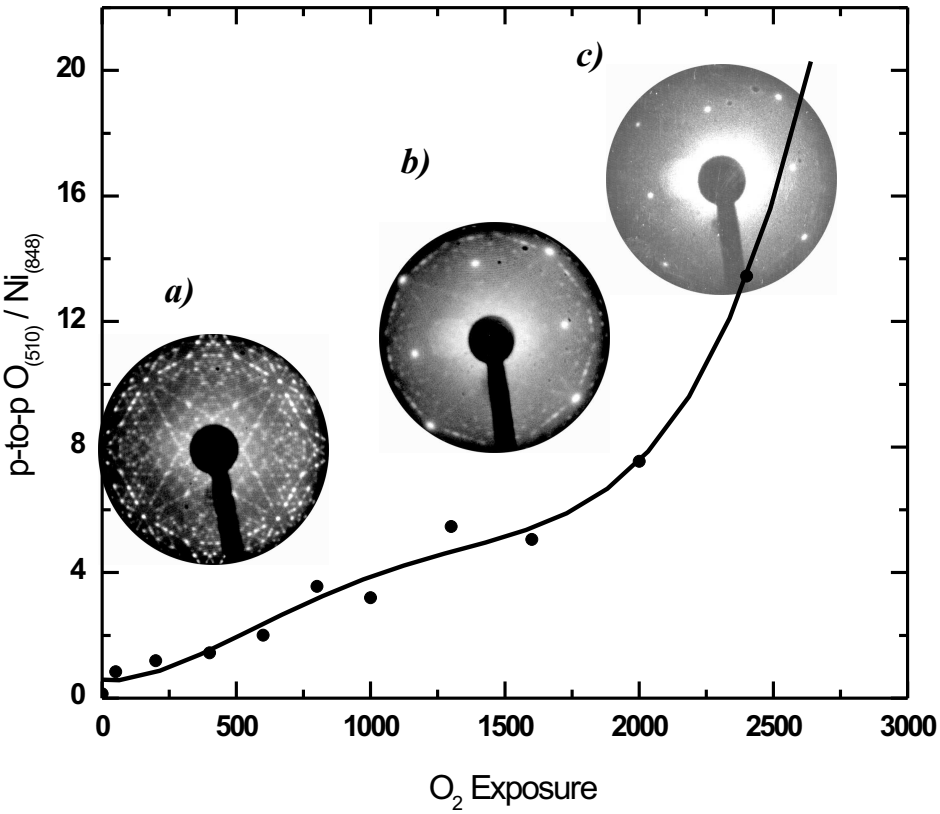

Figure 6.16: (a)The $I_{O(510)}/I_{Ni(848)}$ p-to-p intensity as a function of oxygen exposure for the $Ni_3Al(100)$ oxidation at 1100 K (p=5×10^{-6} mbar). The LEED pattern (a, b, c) for corresponding oxygen exposure are also shown.

the $I_{O(510)}/I_{Ni(848)}$ p-to-p ratio as a function of O_2 exposure (Fig. 6.16). This ratio increases rapidly with oxygen exposure. After an exposure of 1000 L O_2 the I_O/I_{Ni} ratio has a value 3.2 for 5×10^{-6} mbar, while for oxidation at 10^{-7} mbar a value of 1 was found. After 2000 L O_2 the corresponding values are 7.5 for oxidation at 5×10^{-6} mbar and 1.2 at 10^{-7} mbar.

The evolution of the LEED pattern during oxidation at high pressure at 1100 K is also different with respect to that at lower pressure. During oxidation at 1100 K with an oxygen pressure of $\leq 10^{-7}$ mbar the LEED pattern of the oxide remain almost unchanged (fig. 6.10a-c). With increasing oxygen exposure the only change in the LEED pattern consist in disappearance of the spots due to the substrate.

Exposing the sample at 1100 K to oxygen at 5×10^{-6} mbar, the LEED pattern is gradually changed as a function of O_2 exposure. Up to $\sim$ 500 L O_2 the LEED pattern (fig. 6.16a) is identical to that obtained for oxidation in a pressure range $\leq 10^{-7}$ mbar (fig. 6.10c). Between the $\sim$ 500 and $\sim$ 2000 L O_2 the LEED pattern changes gradually to a (1×1) structure with a quadratic unit mesh (Fig. 6.16b and c). The lattice constant of the quadratic structure from Fig. 6.16c is $\sim$ 3.6 Å. This suggests that the oxidation at 1100 K with 2000 L O_2 leads to the formation of a γ'-Al_2O_3 film which grows with the (100) plane parallel to the surface of $Ni_3Al(100)$.

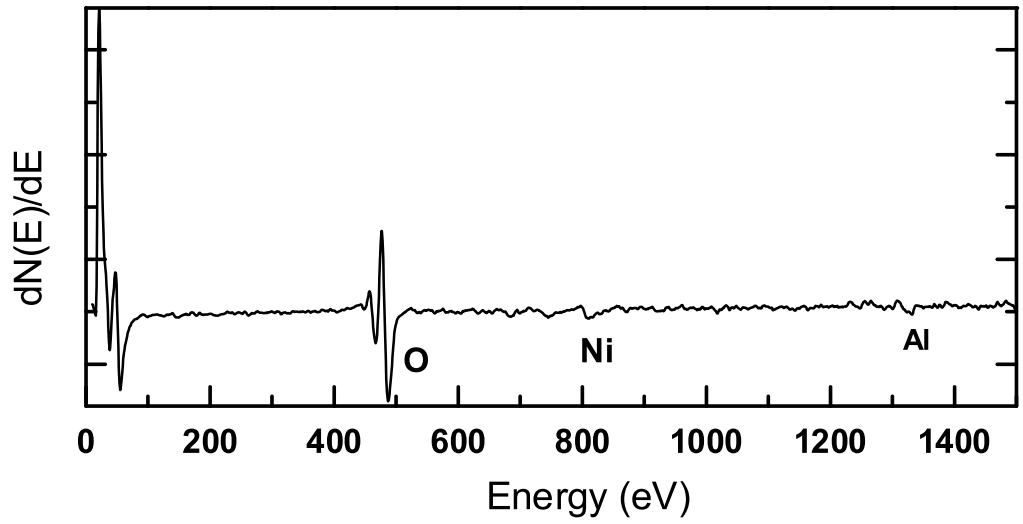

Figure 6.17: The Auger spectrum of $Ni_3Al(100)$ oxidized at 1100 K with 2000 L O_2 (p=5×10^{-6} mbar).

Fig. 6.17 shows the AES spectrum of $Ni_3Al(100)$ after exposure to 2000 L O_2 at 1100 K for a O_2 pressure of 5×10^{-6} mbar. The O(510) AES signal is very high and the Ni(848) signal is strongly reduced by the oxide film. After a higher exposure the p-to-p $I_{O(510)}/I_{Ni(848)}$ ratio increases very much and above $\sim$ 2400 L the Ni signal is vanished completely and therefore, the I_O/I_{Ni} has no meaning anymore.

Fig. 6.18a shows the $I_{O(510)}/I_{Al(1390)}$ ratio of $Ni_3Al(100)$ surface oxidized at 1100 K,

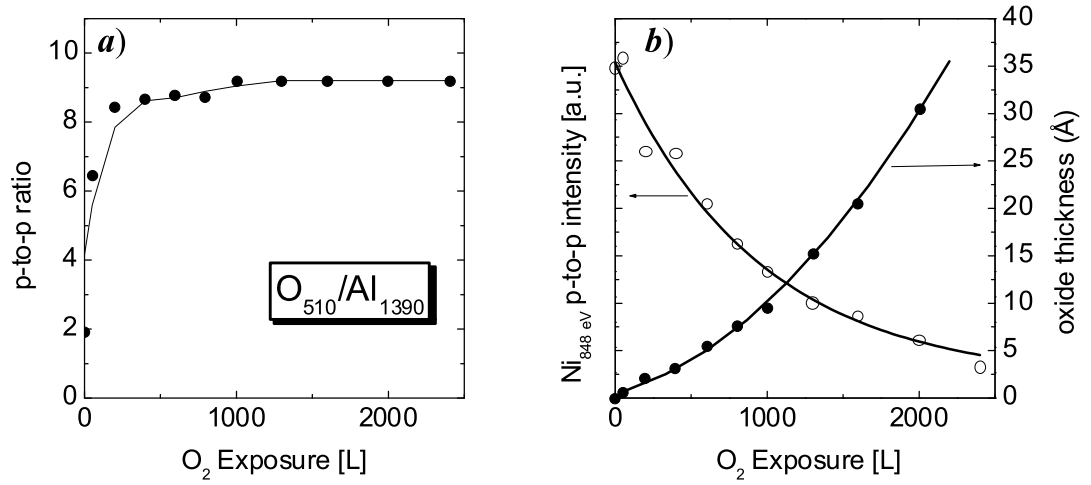

Figure 6.18: (a) $I_{O(510)}/I_{Al(1390)}$ ratio of $Ni_3Al(100)$ surface oxidized at 1100 K (p = 5 × 10^{-6} mbar) as a function of oxygen exposure (b) The Ni(848) p-to-p intensity as a function of oxygen exposure (○); The dependence of the oxide thickness as a function of oxygen exposure (●).

in high pressure range (p = 5 ×10^{-6} mbar) as a function of oxygen exposure. It can be observed that after a rapid increase the $I_{O(510)}/I_{Al(1390)}$ ratio is constant with a value of ∼ 9.2 after exposure at 2000 L O_2. This value is slightly higher with respect to the stoichiometric value of ∼ 7 which was obtained for oxidation in the pressure range of 10^{-7} mbar. This could be attributed to a small oxygen excess in the case of the film obtained in higher oxygen pressure range. From the attenuation of the Ni(848) signal (Fig. 6.18b) we have estimated the thickness of the oxide film after different O_2 exposure, using the equation 6.1. Above 50 L O_2 the oxide thickness shows a parabolic dependence with oxygen exposure (see Fig. 6.18b). As the oxygen exposure is directly related with the time one can conclude that the growth of the oxide films obeys a parabolic time dependence in accordance with Wagner's theory (see section 2.3).

$$x^2[\mathring{A}] = 2.49 \times t[s] \tag{6.4}$$

where x represents the thickness of the oxide film and the parabolic rate constant

$k_p = 2.49$.

After an exposure of 2000 L O_2 a value of $\sim$ 30 Å was found, which is about three times larger with respect to the thickness of the oxide film which was obtained in the pressure range $\leq 10^{-7}$ mbar. Consequently, one can conclude that the growth of alumina film is enhanced in the case of oxidation in higher pressure range. Actually, this is not so surprisingly, because for oxidation in air at 1300 K of NiAl [113] and at 1100 K of CoGa [114], thicknesses of the oxide films up to 250 nm are reported. However, we have to point out that the effects found in the oxygen pressure range 5×10^{-6} mbar could be reproduced only two times with a fresh $Ni_3Al(100)$ surface. Afterwards only the oxide growth reported in the 10^{-7} mbar pressure range was found. An adequate explanation for this effect cannot be given. We can only speculate that, may be, the concentration of Al in the surface region is changed after several oxidation and cleaning cycles.

6.7 Summary

-Oxygen pressure range 10^{-7} mbar

The oxidation of the $Ni_3Al(100)$ surface was studied with EELS, AES, LEED and STM. The structure and the phase of the grown oxide films depends mainly on the oxidation temperature. At room temperature the oxygen adsorbs dissociatively on $Ni_3Al(100)$ leading to the formation of a thin amorphous aluminum oxide layer ($\sim$ 5 Å). Annealing at 1100 K leads to a well ordered γ'-Al_2O_3 film. Oxidation directly at 1100 K leads also to the formation of a well ordered γ'-Al_2O_3.

The thickness of the oxide prepared at 1100 K is $\sim$ 10 Å. The STM experiments performed on $Ni_3Al(100)$ surface directly oxidized at 1100 K show an island growth mode of the oxide. The oxide islands have a quasi-hexagonal shape, which exhibits a quasi-hexagonal superstructure with a periodicity of $\sim$ 18 Å. The completely covered surface shows, in addition to the superstructure with a lattice constant of 18 Å, another hexagonal superstructure with a lattice constant of 54 Å.

The band-gap of ultrathin amorphous and well-ordered Al_2O_3 formed on $Ni_3Al(100)$ are strongly diminished with respect to the bulk values. The lowering of band-gap values of thin alumina films on Ni_3Al is explained with the existence of defects induced states located in the band-gap region.

-*Oxygen pressure range* $\geq$ $5\times$ 10^{-7} *mbar*

The oxidation in a higher O_2 pressure range leads to a thicker oxide layer which shows a (1×1) structure for an exposure ≥2000 L O_2.

Chapter 7

Growth of cobalt on the $Al_2O_3/Ni_3Al(100)$ surface

Metal-oxide interfaces, metal coatings or dispersed metals on oxide supports play an important role in many technological areas. One of them is heterogeneous catalysis, where supported metal catalysts are used to increase the activity or to control the selectivity of reaction processes. Furthermore, ultra thin Al_2O_3 layers are used in permanent magnetic RAM devices [115, 116] as a tunneling barrier between the ferromagnetic materials based on the tunneling magnetoresistance effect (TMR) [2, 3]. Up to now, most studies were performed on TMR structures with a layer of amorphous alumina as insulating barrier between the ferromagnetic layers. However, from a fundamental point of view, i.e. the understanding of the physics of spin dependent tunneling, a transport study through an amorphous insulator is hardly accessible in a theoretical approach. Therefore, many groups have tried to grow epitaxial single-crystal tunnel junction in which the oxide layer is also crystalline (MgO) [117, 118]. As it was shown in Chapter 6, on the $Ni_3Al(100)$ surface a thin Al_2O_3 film grows, which is amorphous when prepared at 300 K and which becomes well-ordered (crystalline) at higher oxidation temperature. By deposition of a ferromagnetic layer (e.g. Co) on top of $Al_2O_3/Ni_3Al(100)$ a three-layer system

is formed, which, below the Curie temperature of Ni_3Al($\sim$ 77 K) can be considered as a TMR-model system.

In this chapter, the deposition of Co at 300 K on $Al_2O_3/Ni_3Al(100)$ is presented. Section 7.1 deals with the thermal stability of the Co film on $Al_2O_3/Ni_3Al(100)$ system. Section 7.2 describes the vibrational properties of the $Co/Al_2O_3/Ni_3Al(100)$ system. Section 7.3 describes the vibrational properties of the $Co/Al_2O_3/Ni_3Al(100)$. The chapter ends with a short summary.

7.1 Thermal stability of the Co film on $Al_2O_3/Ni_3Al(100)$

A thin Al_2O_3 film was prepared by the oxidation of the $Ni_3Al(100)$ surface at 1100 K with 2000 L O_2. The detailed procedure of preparation and the characterization of the oxide layer is described in Chapter 6. Cobalt was deposited by thermal evaporation from a cobalt rod. The pressure during evaporation was $\sim 5 \times 10^{-10}$ mbar. First , the Co growth on the surface of $Al_2O_3/Ni_3Al(100)$ is discussed.

Fig. 7.1 shows AES spectra of $Al_2O_3/Ni_3Al(100)$ in the energy region between 400 and 1500 eV as a function of the amount of Co deposited at 300 K. The spectrum at the bottom is used as a reference. It was taken after oxidation of $Ni_3Al(100)$ surface with 2000 L O_2. The spectrum exhibits AES transitions of O(510 eV), Ni(716, 783, 848 eV) and Al(1390 eV). After a nominal deposition of 3 Å the Co triplet at 656, 716 and 775 eV appears in addition. The transitions at 716 and 775 eV overlap with those of Ni at 716 and 783 eV. Thus, in the spectrum only the Co transition at 655 eV is observed in addition. With the increase of the Co nominal deposition up to 30 Å the O, Ni and Al signals are attenuated. From the attenuation of the O signal and by assuming a layer-by-layer growth (which is questionable in this case) the effective thickness of the Co layer is estimated to be: $\sim$ 2 Å for a nominal deposition of 3 Å, $\sim$ 6 Å for a nominal deposition of 10 Å, $\sim$ 11 Å for a nominal

deposition of 18 Å and $\sim$ 18 Å for a nominal deposition of 30 Å.

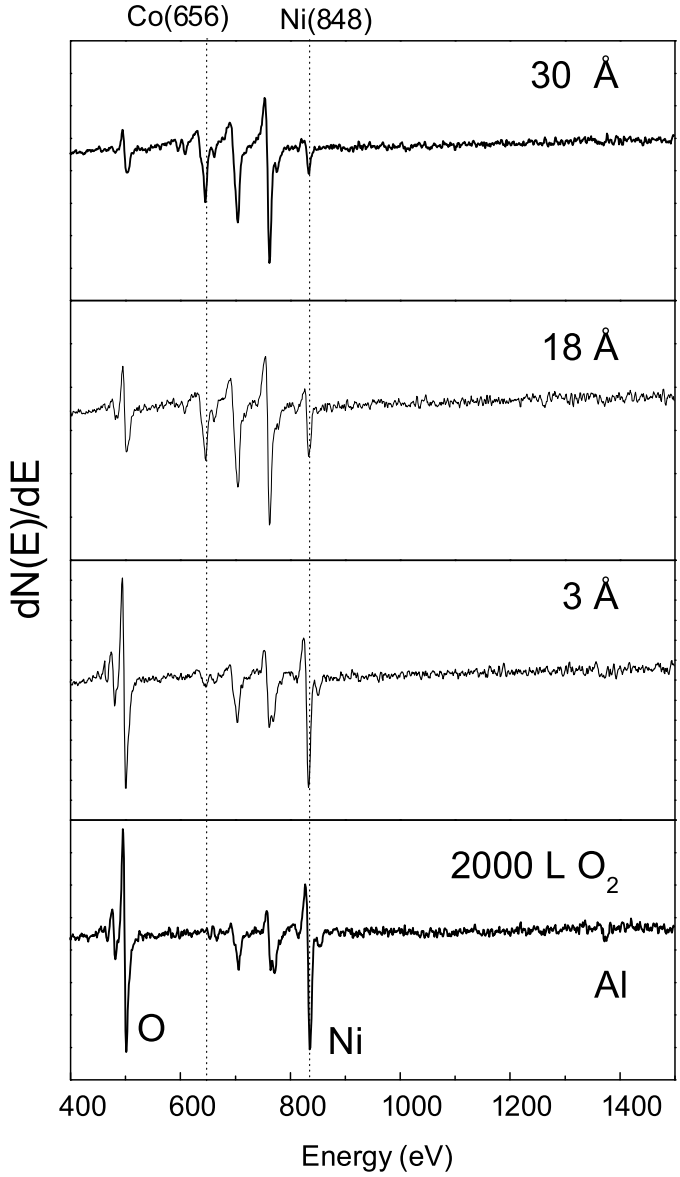

Figure 7.1: AES spectra of $Al_2O_3/Ni_3Al(100)$ as a function of Co deposition at 300 K.

In order to study the thermal stability of the deposited Co film the sample was annealed in steps of 100 K up to 1000 K. The annealing process was monitored using AES.

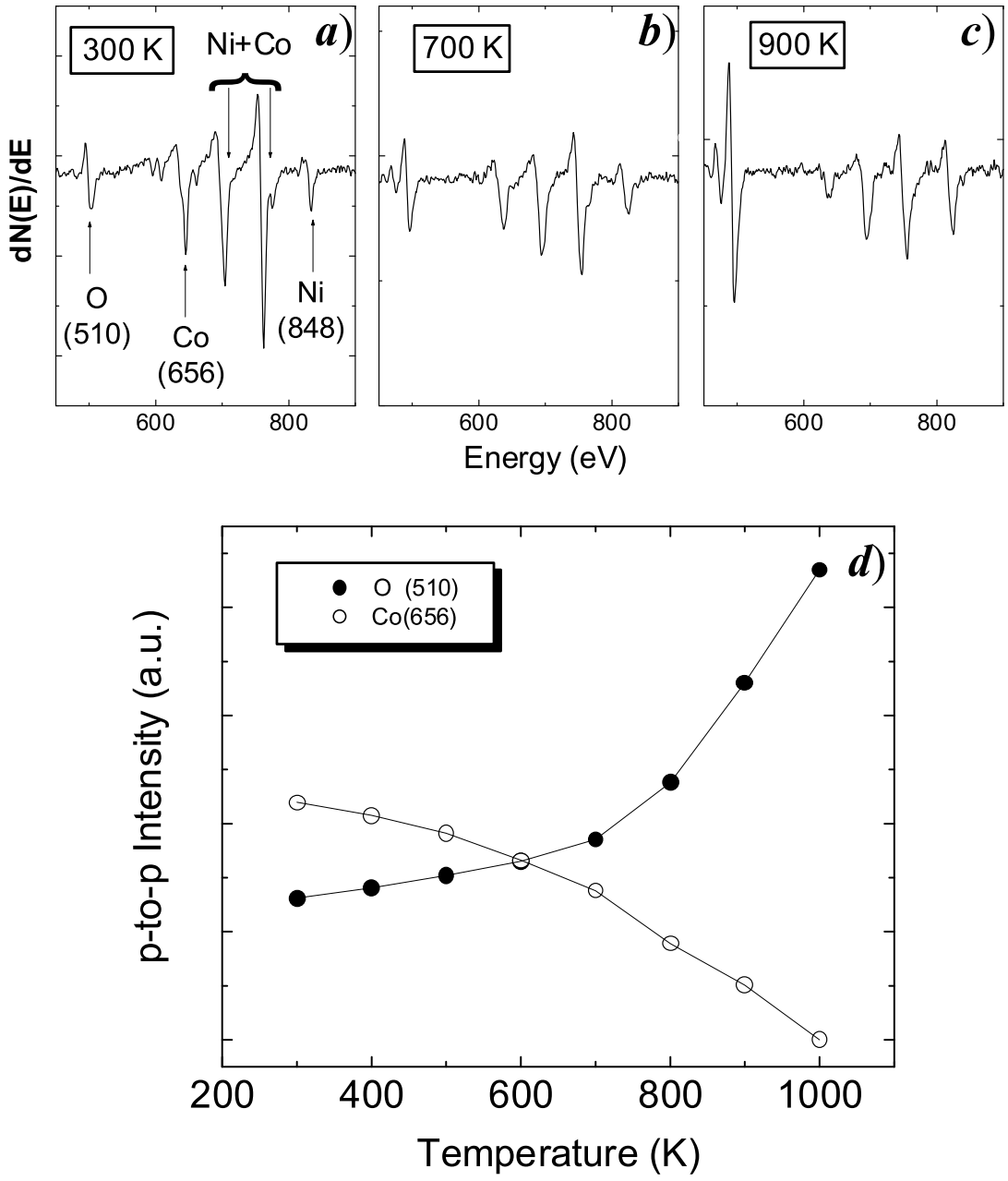

Figure 7.2: AES spectra of $Co/Al_2O_3/Ni_3Al(100)$ (a) after a nominal deposition of 30 Å Co at 300 K ; (b) after annealing at 700 K; (c) after annealing at 900 K; (d) shows the p-to-p intensity of the O(510 eV) and Co(656 eV) signals as a function of annealing temperature.

Fig. 7.2a shows the Auger spectrum of 30 Å Co film deposited at 300 K on Al_2O_3 grown on $Ni_3Al(100)$. The spectrum exhibits AES transitions of O(510 eV), Ni(716, 783, 848 eV) and Co(656, 716, 775 eV) triplets. Whereby the Ni signals at 716 and 783 eV overlap with the Co signals at 716 and 775 eV. Fig. 7.2b and c show AES spectra after annealing at 700 and 900 K, respectively. With increasing temperature the intensities of the Ni transitions increase, while the intensity of the Co decreases. The decrease of the Co signals indicates that Co starts to disappear from the surface during annealing. Fig. 7.2d shows the p-to-p intensity of the O(510) and Co(656) signals as a function of annealing temperature. The O(510) signal is slowly increasing up to $\sim$ 700 K and afterwards a faster increase is found. The Co(656) signal decreases slowly up to $\sim$ 700 K and than the decrease is faster. By annealing up to 700 K the morphology of the Co film seems to be only slightly changed. After annealing at 1000 K the Co signals disappears from the AES spectrum suggesting that the Co film is not present on the surface anymore. Since desorption at this temperature can be excluded, diffusion of Co through the oxide into the substrate is the most plausible explanation. The diffusion of Co through the Al_2O_3 film into the substrate was also found in the case of Al_2O_3/NiAl(110) [119].

For a nominal deposition of 3 Å Co, the LEED pattern of $Al_2O_3/Ni_3Al(100)$ is still visible, which suggests that there are still Co-free areas on the surface and that Co grows as three-dimensional clusters. However, the intensity of Bragg reflections of the oxide is lowered and a diffuse background appears. For higher Co deposition no ordered LEED pattern is observed and the screen exhibits only a diffuse illumination.

7.2 The vibrational properties of $Co/Al_2O_3/Ni_3Al(100)$

Fig. 7.3 shows the EEL spectra of $Al_2O_3/Ni_3Al(100)$ as a function of Co deposition at 300 K. The bottom spectrum shows the characteristic Fuchs-Kliewer losses at

415, 635 and 850 cm^{-1} of $Al_2O_3/Ni_3Al(100)$. For a nominal deposition of 1 and 3 Å

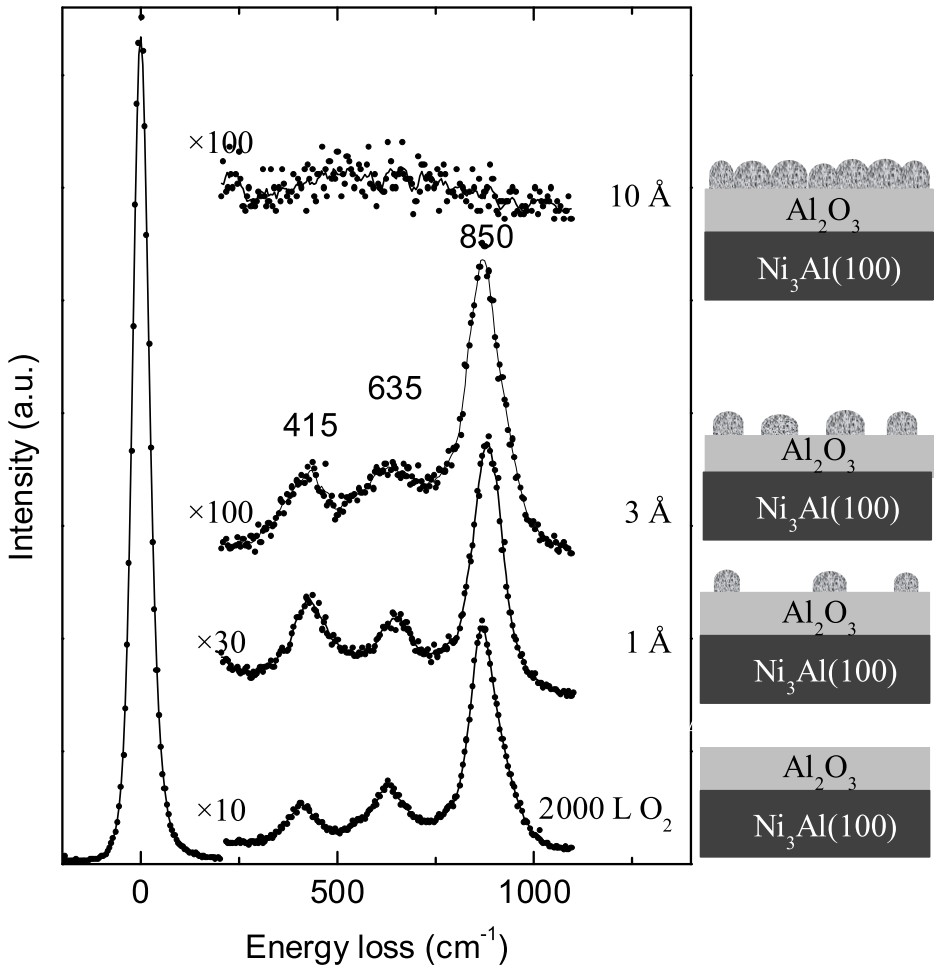

Figure 7.3: (a)EEL spectra of $Al_2O_3/Ni_3Al(100)$ as a function of Co deposition at 300 K.

the intensity of the losses is lowered with 30% and 70 %, respectively. At a nominal deposition of 10 Å no losses are observed in the EEL spectrum. This highlights the metallic behaviour due to the cobalt layer, which screens the dipoles of the oxide. Another conclusion can also be drawn: for a nominal deposition of 1 and 3 Å, the Co grows as three-dimensional clusters on the alumina surface, which do not cover the entire oxide surface. Therefore, the intensity of the FK phonons of alumina is not completely quenched. The decrease of the intensity of the FK losses results

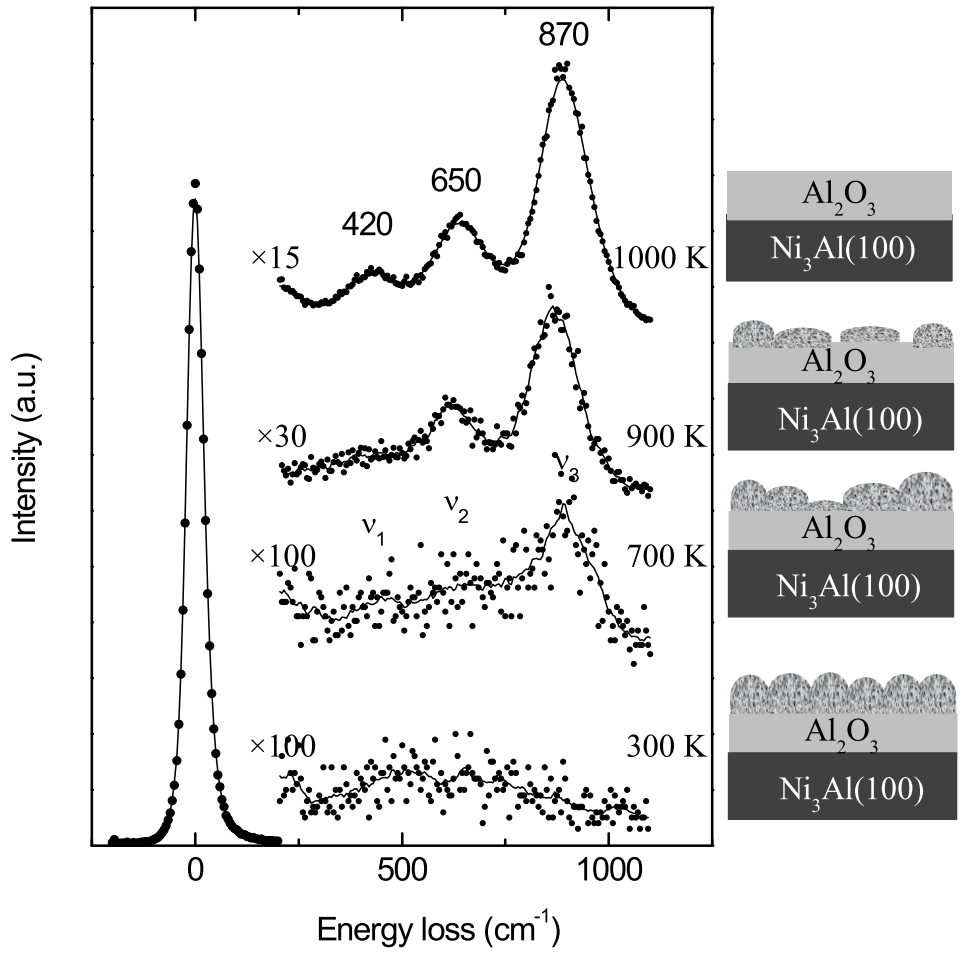

Figure 7.4: EEL spectra of $Co/Al_2O_3/Ni_3Al(100)$ as a function of annealing temperature.

from the decrease of Co-free oxide areas. By electron impact, the Co clusters are not charged with electrons, i.e. the incoming electrons tunnel through the oxide into the substrate. The evolution of Co deposition is schematically represented on the right side of the EEL spectra. This scheme suggests that the surface is completely and homogeneously covered with Co only above a nominal deposition of 10 Å Co.

Fig. 7.4 shows EEL spectra of 30 Å nominal deposition of Co on $Al_2O_3/Ni_3Al(100)$ at 300, 700, 900 and 1000 K. As was shown, already after 10 Å Co deposition at 300 K the FK modes of the oxide are completely screened by the Co film. After 30 Å the modes are, of course, even better screened. After annealing at 700 K,

the EEL spectrum exhibits the three characteristic losses (ν_1, ν_2 and ν_3) of Al_2O_3. The intensity of these losses is very small in comparison with that of the clean "freshly" prepared Al_2O_3 layer on $Ni_3Al(100)$; e.g. in fig. 7.4 the intensity of the most intense mode at 870 cm^{-1} (ν_3) is about 20 times smaller than that of the clean Al_2O_3 layer. Also, the intensity ratios of the losses $\nu_1 : \nu_2 : \nu_3 \sim 100 : 36 : 15$ is similar to those for the clean Al_2O_3 on $Ni_3Al(100)$ ($\nu_1 : \nu_2 : \nu_3 \sim 100 : 27 : 17$). Thus, annealing at 700 K, induces only a change in the morphology of the Co film. The perfect screening is revoked and and this implies that the electron beam sees Co-free Al_2O_3 areas. Further annealing at 900 K leads to an increase of the intensity of the three losses found at 420, 650 and 870 cm^{-1}. The intensity of these losses is much higher (see the multiplication factor) with respect to that obtained after heating at 700 K and the FWHM is smaller. After annealing at 1000 K the three FK modes of $Al_2O_3/Ni_3Al(100)$, with approximately the same intensity in comparison with that of the FK modes of the clean Al_2O_3 film, are observed. The frequencies of the losses are only slightly higher with respect to those of the clean, fresh prepared $Al_2O_3/Ni_3Al(100)$. This indicates that the cobalt film is disappeared from the surface and the Al_2O_3 layer is again "visible" by EELS.

7.3 The morphology of the $Co/Al_2O_3/Ni_3Al(100)$ surface

The morphology of the $Co/Al_2O_3/Ni_3Al(100)$ surface at 300 K and during the annealing process was investigated by STM.

Fig. 7.5a shows a STM image after a nominal deposition of 0.1 Å Co on the ordered alumina film.

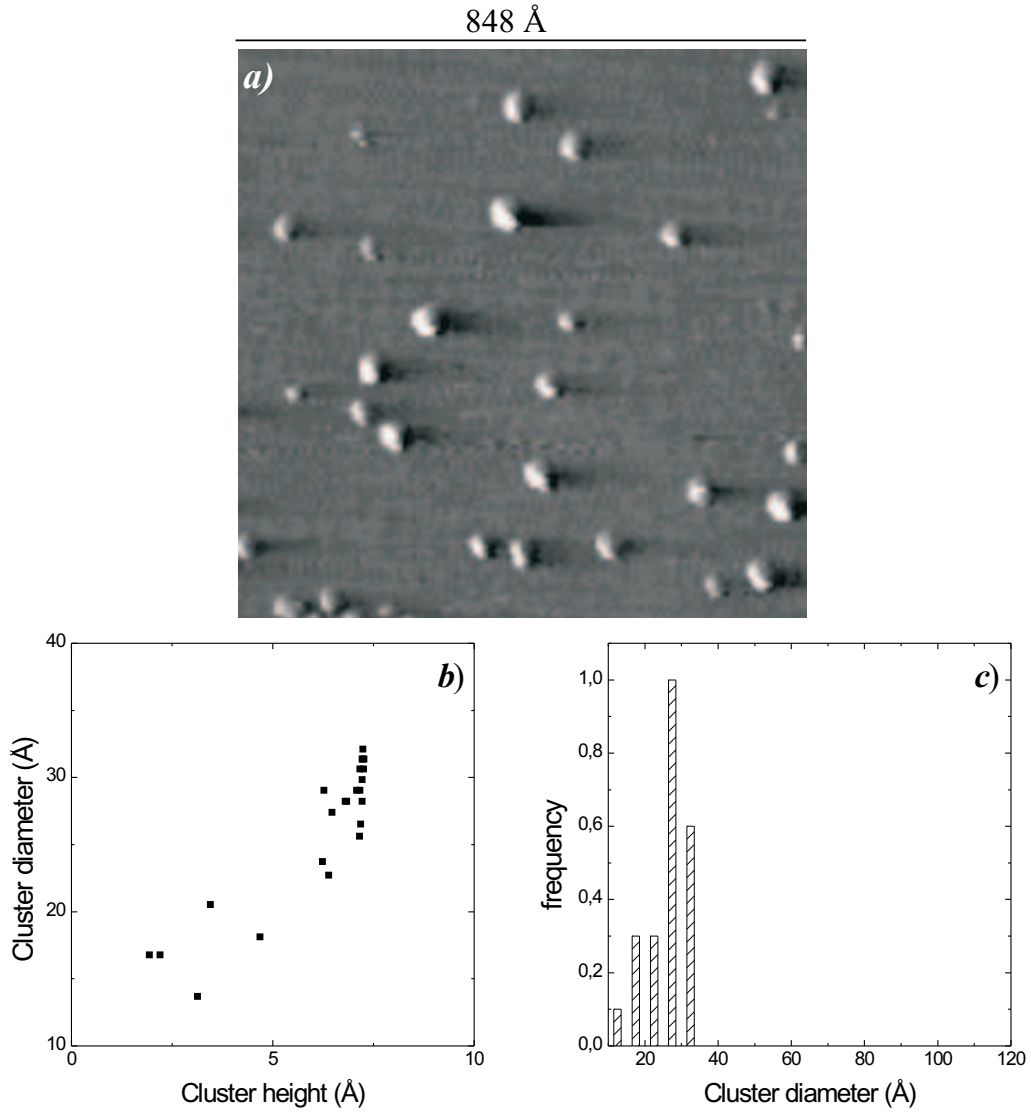

Figure 7.5: (a) STM image of nominal 0.1 Å Co deposited onto $Al_2O_3/Ni_3Al(100)$ at 300 K; U_t = - 1 V, I_t = 0.3 nA; (b) The dependence of particle height versus particle diameter; (c) The normalized diameter distribution of the Co clusters.

The corresponding particle height dependence versus particles diameter is given in fig. 7.5b. Already at this coverage, particle (clusters) with a height up to 6 Å are grown on the surface.

The normalized diameter distribution of clusters is shown in Fig. 7.5c, showing a maximum around 30 Å. The surface coverage with Co clusters is about 3 % and

cluster density on the terraces is $\sim 1 \times 10^{12}$ cluster/cm^2.

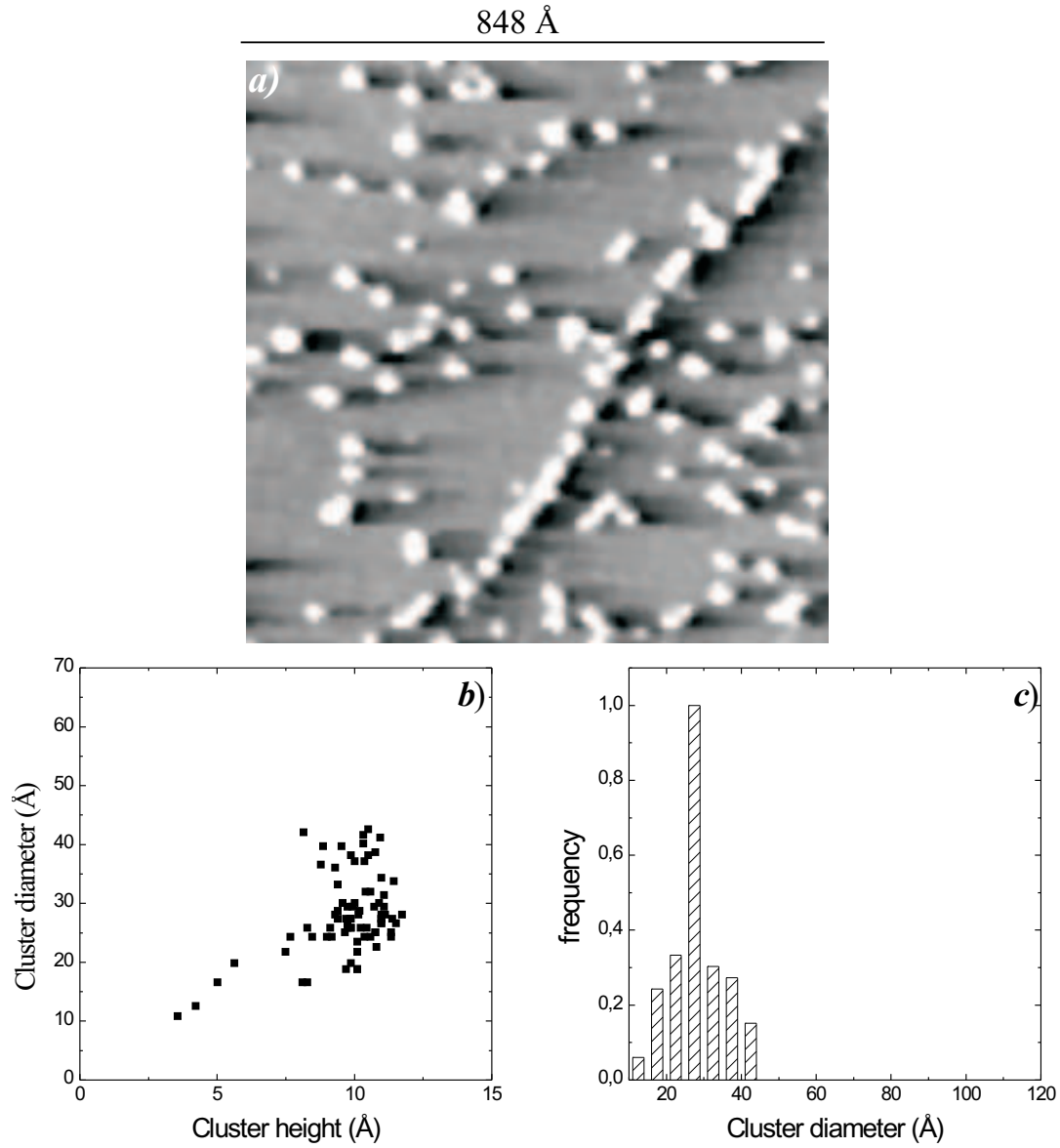

Figure 7.6: (a) STM image of nominal 0.5 Å Co deposited onto $Al_2O_3/Ni_3Al(100)$; U_t = - 3.86 V, I_t = 0.3 nA; (b) The dependence of particle height versus particle diameter; (c) The normalized diameter distribution of clusters.

Fig. 7.6a shows a STM image with a scanned area of 848 × 848 Å^2 after a nominal deposition of 0.5 Å Co on the alumina.

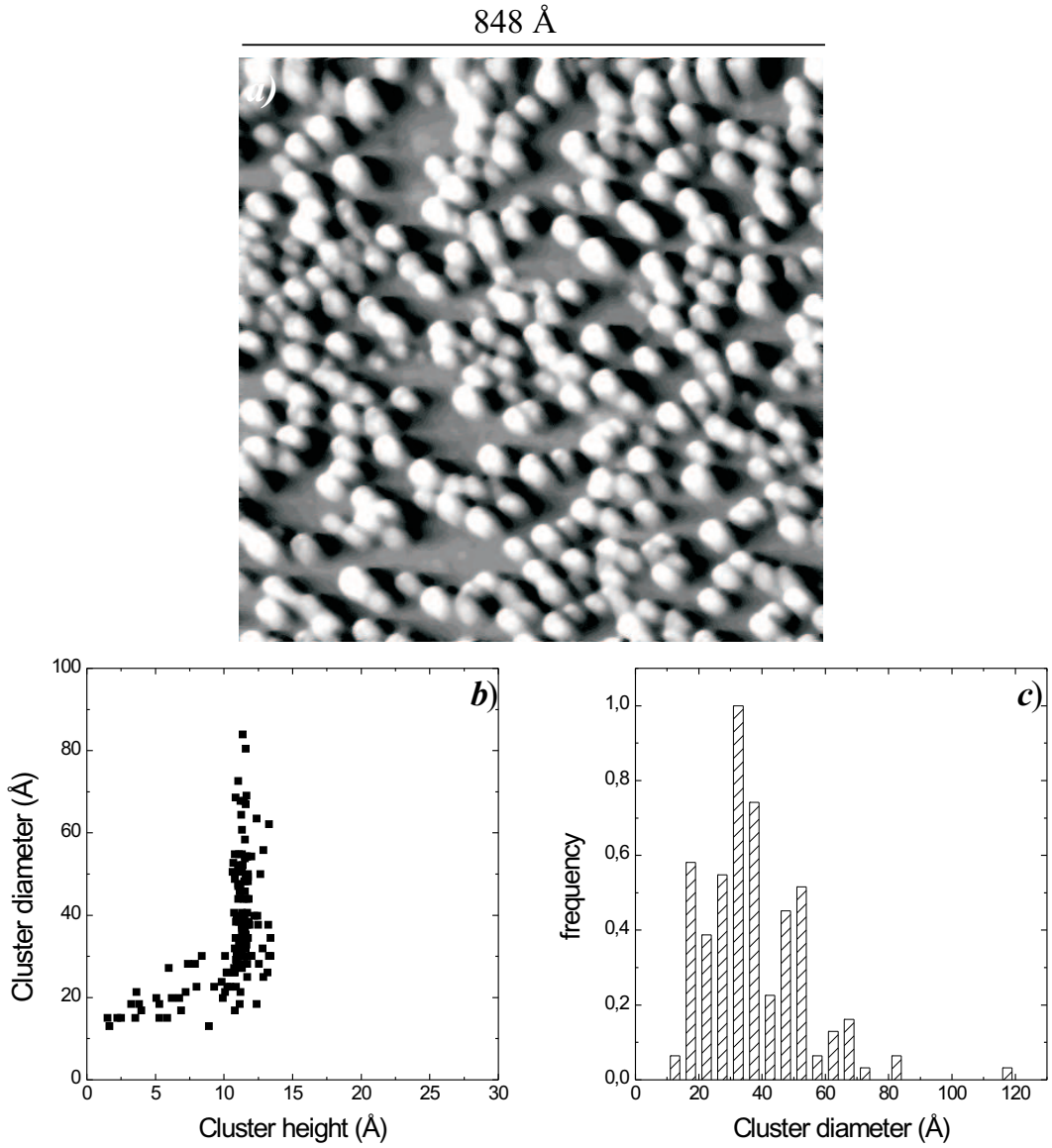

Figure 7.7: (a) STM image of nominal 2 Å Co deposited onto $Al_2O_3/Ni_3Al(100)$; U_t= - 3.76 V, I_t = 0.3 nA; (b) The dependence of particle height versus particle diameter; (c) The normalized diameter distribution of clusters.

At this stage the clusters have a height up to 10 - 12 Å (fig. 7.6b) with a mean diameter of $\sim$ 30 Å (Fig. 7.6c). 11% of the surface is covered with Co, showing a particles density of 3.5 $\times 10^{12}$ cluster/cm^2. A strongly decorated step is visible. This shows that steps act as nucleation centers.

Fig. 7.7a shows a STM image with a scanned area of 848 × 848 Å^2 after a nominal deposition of 2 Å Co. The clusters have a height up to 12 Å. The diameter of the clusters shows a broad distribution (fig. 7.7c) with a maximum centered at 35 Å. Larger clusters with a mean diameter of ∼ 70 - 80 Å indicate that coalescence of some of the clusters took place. The particle density in this case is 6 × 10^{12} cluster/cm^2. About 60 % from surface is covered with Co clusters. For a nom-

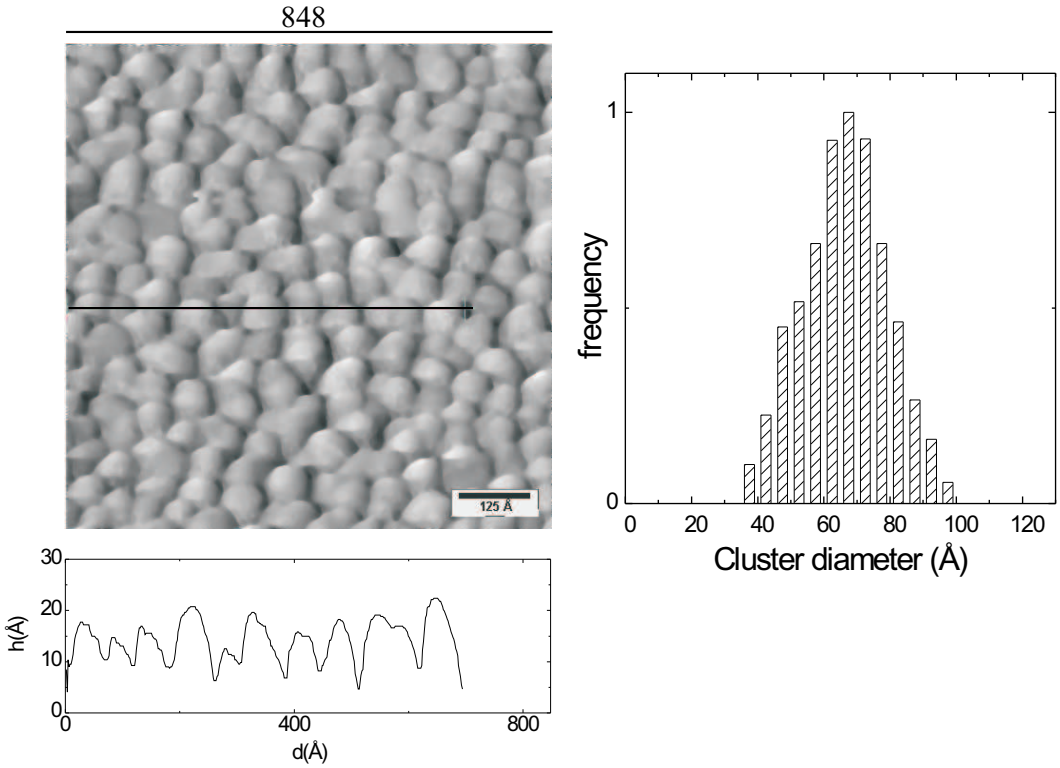

Figure 7.8: (a) STM image and line scan of 30 Å nominal Co deposited onto $Al_2O_3/Ni_3Al(100)$; U_t = 0.5 V, I_t = 0.3 nA; (b) The normalized diameter distribution of clusters.

inal deposition of 30 Å the diameter distribution of the clusters shows a maximum at ∼ 85 Å(see Fig. 7.8b). The clusters percolate showing a roughness of about 10 Å as it is revealed by the line scan bellow the Fig. 7.8. The island density is in this

case 6×10^{12} cluster/cm^2. Unfortunately, for Co on $Al_2O_3/Ni_3Al(100)$ it was not possible to get atomic resolution of the top of the Co clusters.

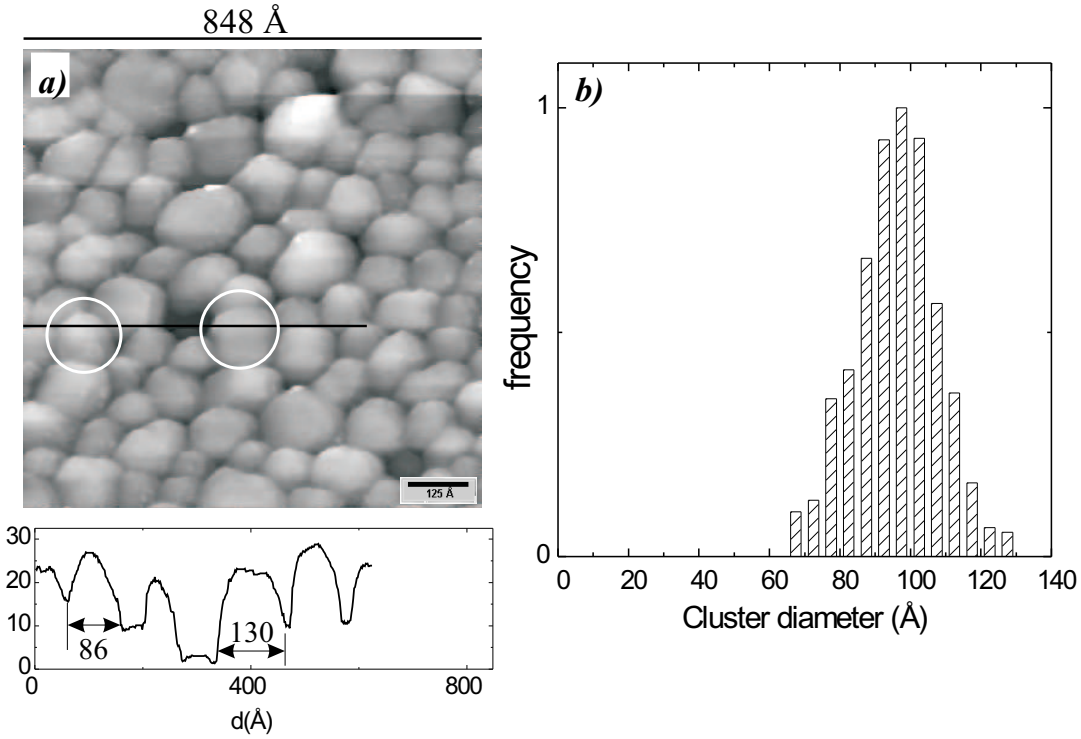

Figure 7.9: (a) STM image of 30 Å $Co/Al_2O_3/Ni_3Al(100)$ after annealing at 700 K ($U_t = 0.25$ V, $I_t = 0.15$ nA); (b) The normalized diameter distribution of the clusters.

For Pd deposited on $Al_2O_3/Ni_3Al(100)$ it was possible to image individual clusters with atomic resolution [119]. On the top of the facets, the hexagonal arrangement of the (111) surface was identified.

The morphology of 30 Å Co film was also investigated as a function of annealing temperature. As we shown before, the sample was annealed in steps of 100 K up to 1000 K.

Fig. 7.9a shows a STM image of the 30 Å Co film after annealing at 700 K. Compared to 300 K, the particle diameter are much larger, i.e. bigger clusters are formed by coalescence. At 700 K, the distribution of the clusters diameter shows a maximum at $\sim$ 100 Å (see the Fig. 7.9b). The clusters indicated by circles have diameters of

$\sim$ 90 Å and $\sim$ 130 Å. The appearance of holes about 20 Å deep with a diameter of $\sim$ 60 Å suggest that at this temperature a diffusion of Co clusters through the oxide film sets in. After annealing the Co film at 900 K dramatic changes take place both

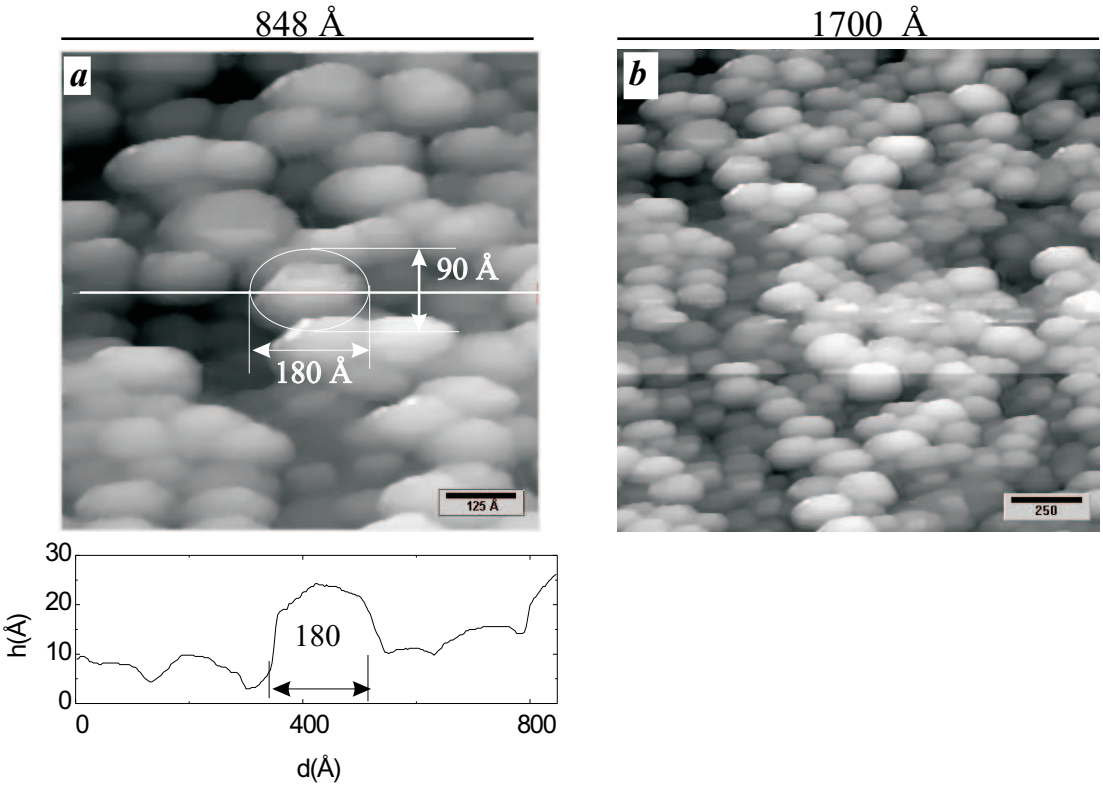

Figure 7.10: (a) STM image of 30 Å $Co/Al_2O_3/Ni_3Al(100)$ after annealing at 900 K (U_t = 0.25, I_t = 0.15); (b) Large area STM image of 30 Å $Co/Al_2O_3/Ni_3Al(100)$ after annealing at 900 K (U_t = 0.45 V, I_t = 0.15 nA).

in the roughness of the film and in the cluster size (fig. 7.10a and b). Conglomerates of large clusters with sizes of the order of 150 Å are visible, while the roughness of the film increased from 10 Å at room temperature to 20 - 25 Å. The clusters have an elongated shape with length of $\sim$ 180 Å and a width of $\sim$ 90 Å (see the cluster indicated by a ellipse in figure 7.10a). Fig. 7.10b shows a large scan area of the cobalt film after annealing at 900 K. The increase of the roughness can be clearly

observed.

7.4 Summary

Co grows at room temperature on $Al_2O_3/Ni_3Al(100)$ as three dimensional clusters (Volmer-Weber growth mode). From thermodynamic point of view this is explained due to the much larger surface free energy of Co (2709 $mJ \cdot m^{-2}$) [120] than that of alumina ($\sim$ 690 $mJ \cdot m^{-2}$) [121]. Already at very low Co deposition (nominal 0.1 Å) 3D-island with a height of $\sim$ 6 Å are found. Further nominal deposition of 0.5 and 2 Å Co leads to larger and higher clusters. Up to a nominal cobalt deposition of 3 Å the surface is not completely covered with Co. This is shown: (a) by EELS which still exhibits the three characteristic FK losses of Al_2O_3; (b) by LEED, where the Bragg reflections of the oxide are still observed and (c) by STM, where Co free areas are clearly observed. Above a nominal deposition of 10 Å the Co film covers the alumina layer completely and homogeneously which leads to a screening of the oxide dipoles. For a nominal deposition of 30 Å Co at 300 K, large Co clusters with a mean diameter of $\sim$ 85 Å are found. The film has a roughness of $\sim$ 10 Å.
Annealing the film at 700 and 900 K leads to a coalescence of Co clusters, and to a gradually diffusion of some clusters through the oxide layer into the substrate. After annealing at 1000 K, Co disappears from the surface as is confirmed by AES (which shows the characteristic AES spectra of Al_2O_3) and by EELS (which shows the FK modes of Al_2O_3).

Chapter 8

The oxidation of CoAl(100)

In this chapter the oxidation of the CoAl(100) surface at 300, 1000 and 1100 K is presented. The oxidation of the (100) surface of intermetallic binary alloys NiAl [38, 82, 122], Ni_3Al [57, 80, 123], and FeAl [40, 124] was already investigated by different experimental techniques. At 300 K, the adsorption of oxygen induces a segregation of Al atoms to the surface and their reaction with adsorbed oxygen leads to the formation of an amorphous Al_2O_3 layer. Oxidation at higher temperature leads to the formation of well-ordered Al_2O_3 layers. Oxidation of the (100) surface of NiAl and FeAl at $\sim$ 1000 K leads to an oxide layer which shows a (2×1) structure with respect to the substrate. This (2×1) structure is explained by the formation of the θ-Al_2O_3 phase on the surface. As was shown in chapter 6, a different situation occurs for the Ni_3Al(100) surface, where another Al_2O_3 phase (namely γ'-Al_2O_3) grows at $\sim$ 1000 K. CoAl has the same B2 structure as NiAl and FeAl, and therefore it is interesting to see if similar alumina phases are growing on it. The oxidation of the CoAl(100) surface will be discussed in comparison to the data found for NiAl, FeAl and Ni_3Al. The chapter is organized as follows: In section 8.1 we present the cleaning procedure of CoAl(100) and the properties of the clean surface. The section 8.2 presents the oxidation of CoAl(100) surface at 300, 1000 and 1100 K. In section 8.3 the main results are shortly reviewed.

8.1 The clean CoAl(100) surface

The CoAl(100) sample was cut by spark erosion from a single crystal rod and the surface was mechanically polished. The accuracy of the surface orientation was better than 0.1°. The main impurities (C and O) were removed by several cycles of Ar^+ ion sputtering (1 μA, 1 kV) and subsequently annealing at 1500 K. Fig. 8.1

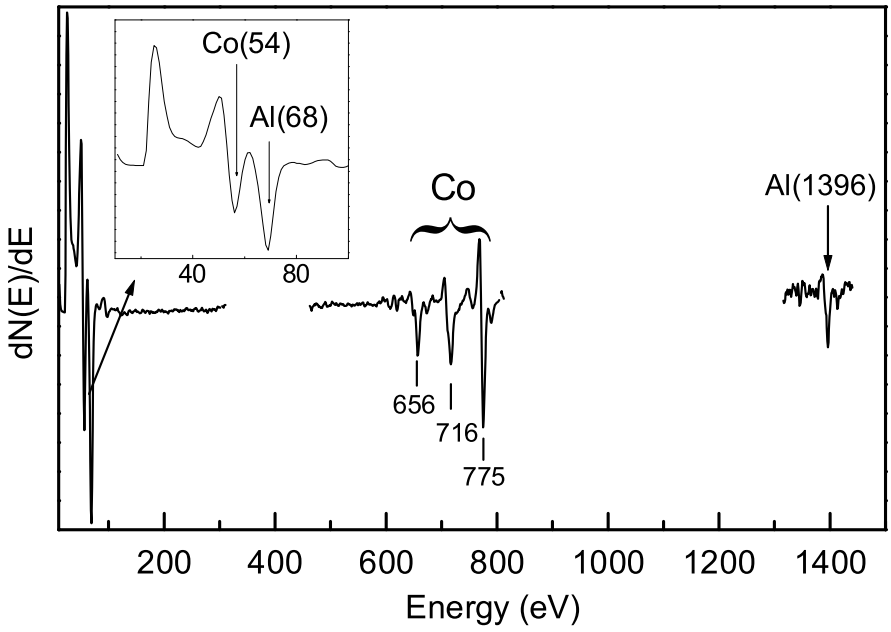

Figure 8.1: AES spectrum of the clean CoAl(100); The inset shows the AES spectrum in the energy region between 20 and 100 eV.

shows the AES spectrum of the clean CoAl(100) surface. In the high energy region the three LMM transitions of Co (656, 716 and 775 eV) and the KLL transition of Al (1396 eV) are displayed. The inset shows the AES spectrum in the energy region between 20 and 100 eV, with the transitions $L_{2,3}VV$ of Al^0(68 eV) and $M_{2,3}VV$ of Co(54 eV). The clean surface shows a (1×1) LEED pattern (Fig. 8.2) with sharp Bragg reflections and very low background.

Fig. 8.3 shows a typical EEL spectrum of the clean CoAl(100) surface which exhibits a pronounced shoulder (loss) at 235 cm^{-1}($\sim$ 29 meV). This mode represents a quasi-

transverse optical mode arising from the vibration of Al atoms perpendicular to the surface. A similar loss was observed in the EEL spectrum of NiAl(111)[37].

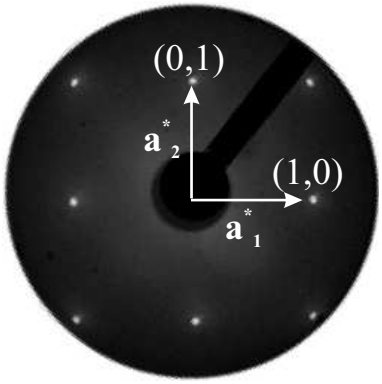

Figure 8.2: The LEED pattern of clean CoAl(100).

Fig. 8.4a shows a STM image with a large scanned area of 3392×3392 Å^2. The image displays flat and large terraces with a width of 500 - 1000 Å separated by steps with an average height of 2.8 Å. This step height corresponds to the lattice constant of CoAl(100) and represents a double atomic step (see fig. 8.4). The fact that the

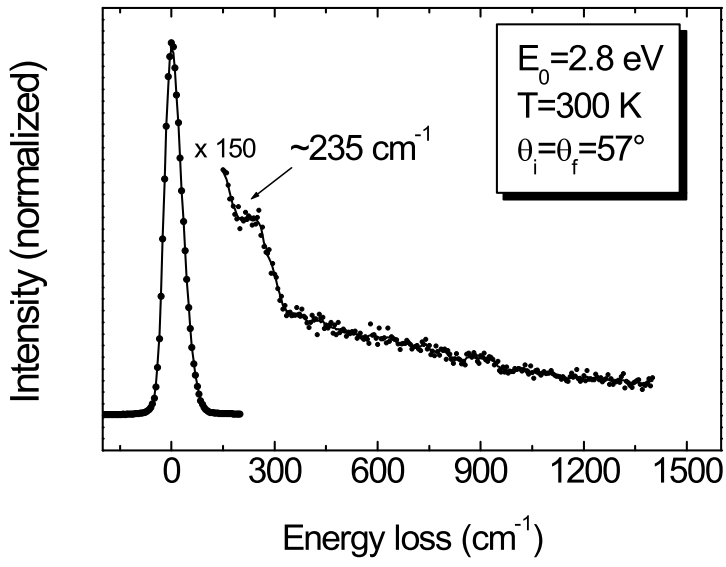

Figure 8.3: The EEL spectrum of the clean CoAl(100) surface.

terraces are always separated by double atomic steps strongly suggest that only one of the two possible terminations (Co or Al) occurs. Double atomic steps were found also for the clean CoGa(100) surface [41]. In the case of NiAl(100) surface three different terminations and structures of the surface were found as a result of different annealing temperature [125]. For high annealing temperature (1400 K), a (1×1)

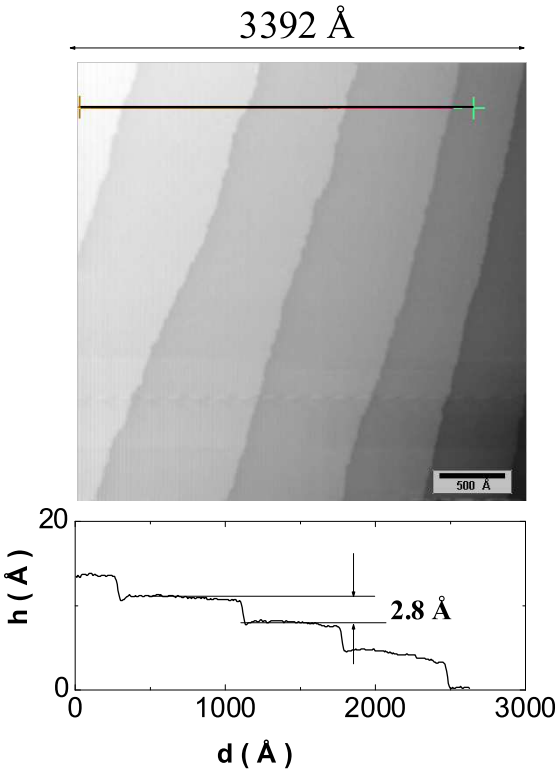

Figure 8.4: The STM images of clean CoAl(100) (1.7 V; 1 nA); The line scan below exhibits a step height of $\sim$ 2.8 Å.

structure of the NiAl(100) surface was found, which is terminated by Ni atoms. Long time annealing at temperature $\leq$ 500 K results in a defect enriched Al terminated NiAl(100) surface, while an intermediate annealing temperature around 800 K leads to an Al terminated missing row surface structure. The cleaning procedure of the CoAl(100) surface consist of sputtering cycles followed by annealing at 1500 K. This leads also to a (1×1) structure. In analogy with the cleaning procedure of

NiAl(100) we expect a Co termination of the (100) surface of CoAl. Unfortunately, our experimental techniques did not allow the determination of surface termination.

8.2 The oxidation of CoAl(100)

8.2.1 The growth of Al_2O_3 films on CoAl(100) studied by AES

Fig. 8.5 shows an AES spectrum of the CoAl(100) surface with 2000 L O_2 at 300 K. In addition to the AES peaks revealed by the clean CoAl(100) surface, the O(KLL)

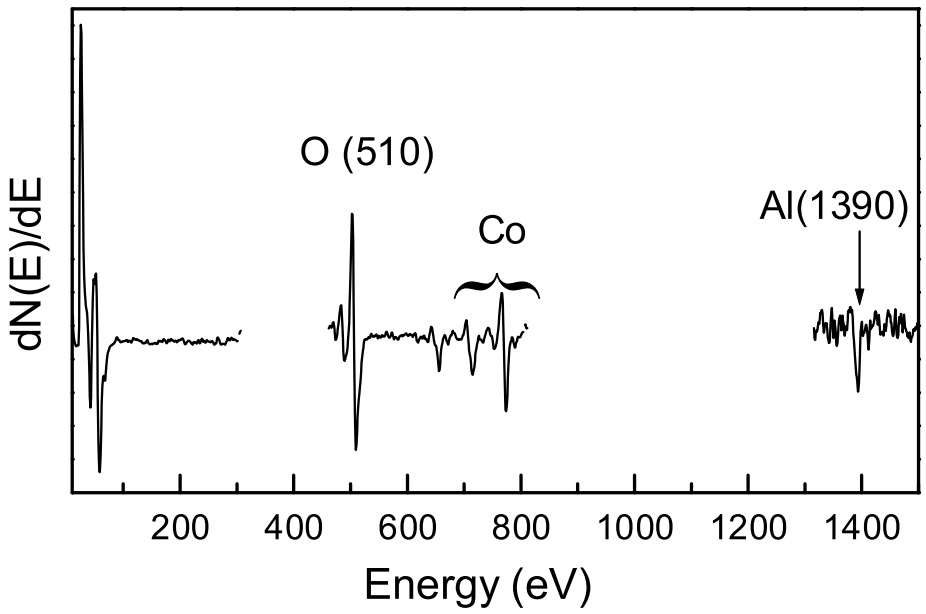

Figure 8.5: AES spectrum of CoAl(100) after exposure to 2000 L O_2 at 300 K.

transition is observed. The oxidation at 300 K as a function of oxygen exposure was monitored by AES in the energy region between 20 and 100 eV. The spectrum at the top in Fig. 8.6a shows the Auger transitions of Al^0 at 68 eV and of Co at 54 eV of the clean CoAl(100) surface. The middle spectrum and the bottom spectrum were taken after an exposure of 5 and 2000 L O_2. After oxidation with 5 L O_2 the intensity

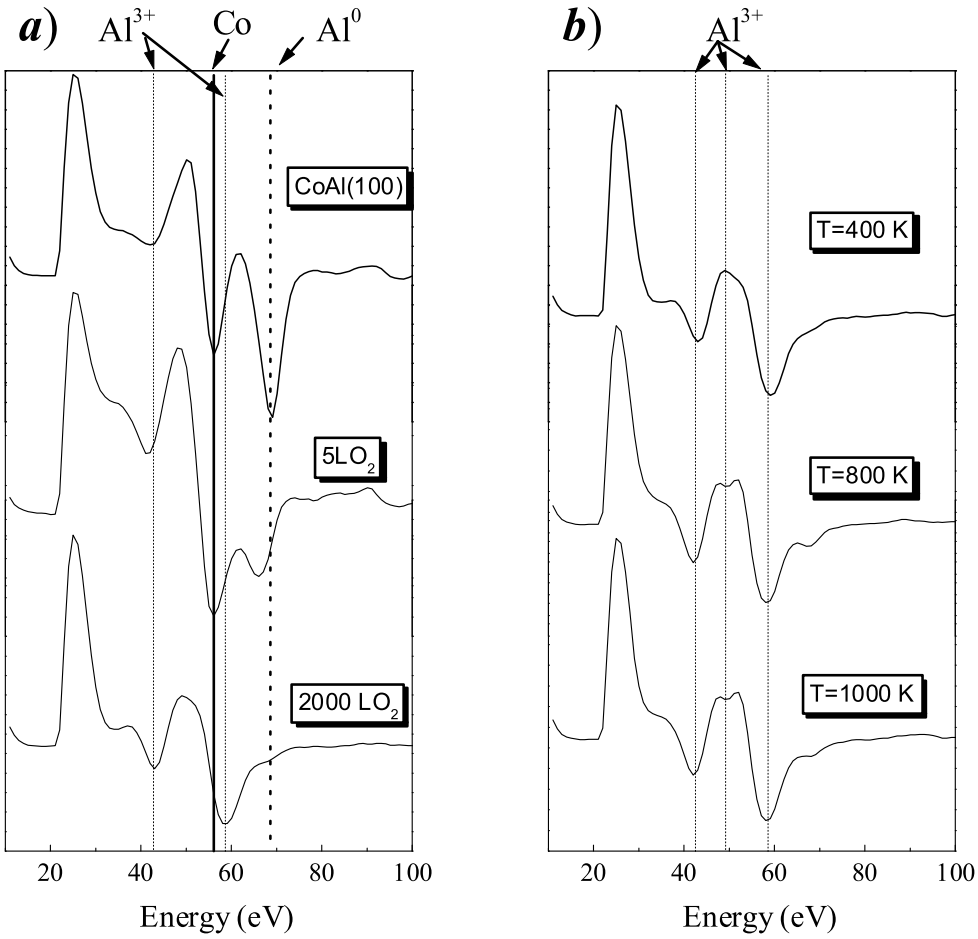

Figure 8.6: AES spectra of the CoAl(100) surface as a function of oxygen exposure; (a)for oxidation at 300 K; (b) for oxidation at 400, 800 and 1100 K.

of the Al^0 signal is decreased, and it is vanished almost completely after oxidation with 2000 L O_2. Subsequently, new Auger signals occur at $\sim$ 42 and $\sim$ 58 eV which originate from Al^{3+} ions [87]. This indicates that the Al atoms are involved in the oxidation process and an Al_2O_3 layer is formed on the surface. The Co signal at 54 eV is totally screened by this layer. From XPS studies on NiAl(110) [84], FeAl(110) [40] $Ni_3Al(111)$ and $Ni_3Al(100)$ [81] it is known that only Al atoms are oxidized and the Ni and Fe atoms remain unaffected. Our AES investigations suggest a similar situation in the case of CoAl.

After oxidation at 300 K with 2000 L O_2, the sample was annealed at elevated

temperatures. Fig. 8.6b shows the evolution of the AES transitions in the low energy region during annealing at 400, 800 and 1000 K. With the increase of the temperature, a new transitions at $\sim$ 47 eV is developed in addition to the transitions at $\sim$ 42 and $\sim$ 58 eV. They are characteristic for Al^{3+} ions. The Al KLL transition is also shifted to $\sim$ 1390 eV (not shown here), which is characteristic for the KLL transition of Al^{3+} ions.

For further investigation of the oxidation we took oxygen uptake curves at 300 and 1100 K by analyzing the p-to-p ratio of the O (510) and the Co (775) transitions. During the adsorption steps the oxygen partial pressure was adjusted between 3×10^{-8} and 1×10^{-7} mbar. The uptake curves for the adsorption at 300 K and 1100 K are shown in Fig. 8.7a. After a high initial growth rate the thickening drops

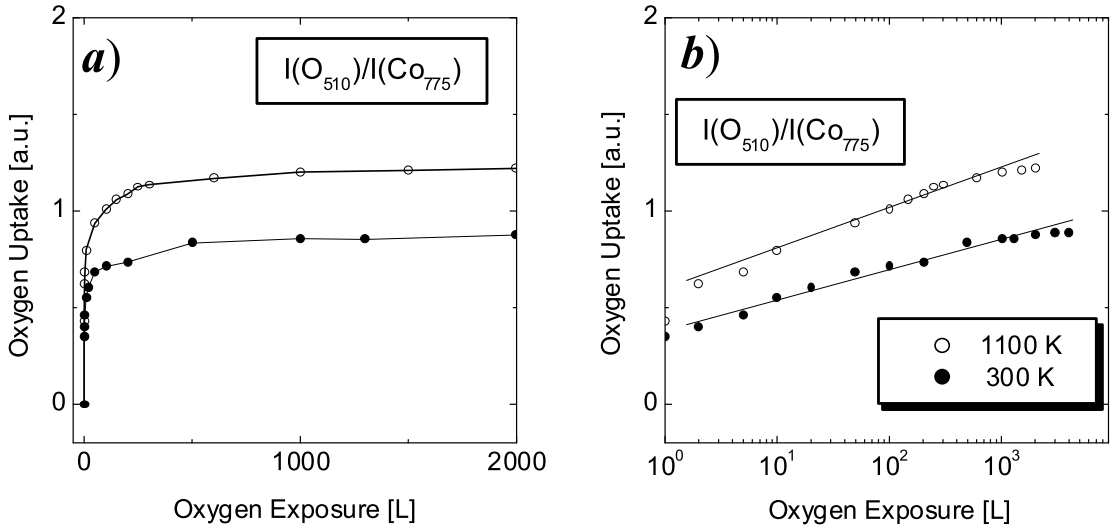

Figure 8.7: (a) Oxygen uptake curves of oxidation at 300 and 1100 K; $I_{O(510)}/I_{Co(775)}$; (b) The uptake curves in a logarithmic scale.

to very low rates of logarithmic type. After oxidation at 1100 K with 2000 L O_2 the I_O /I_{Co} ration amounts to $\sim$ 1.2, while after oxidation at 300 K with 2000 L O_2 the I_O/I_{Co} amounts to 0.8.

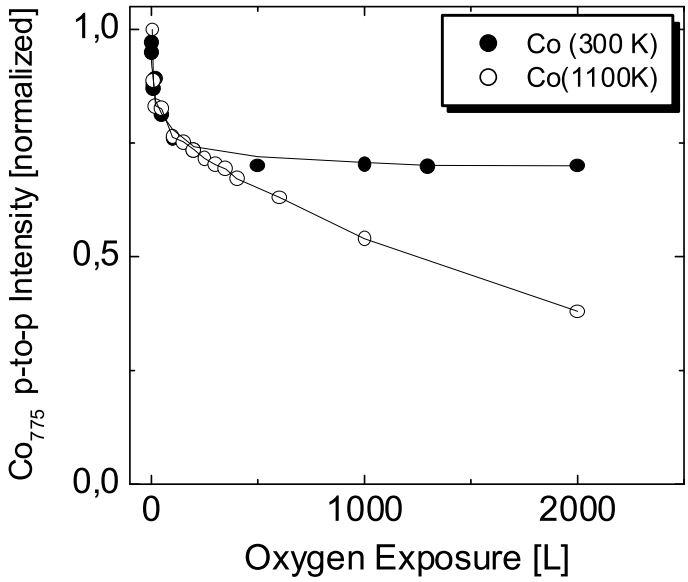

Figure 8.8: The Co(775) ratio variation as a function of oxygen exposure at 300 and 1100 K.

In the low temperature oxidation regime, the thermal activation is insufficient to account for ion generating and movement [42]. Other driving forces such as those generated by an electric field between the O^{2-} and M^{+} are postulated. This leads to a growth rates of logarithmic type. The corresponding theory was given by Cabrera and Mott [44]. The logarithmic growth rate can be seen in Fig. 8.7b which shows the curves of Fig. 8.7a in a logarithmic scale. The growth rate is also affected by the state of the metal. Since CoAl is a single crystal, there are no grain boundaries or other paths for easy ion movement. Moreover, the grown oxide is either amorphous or well-ordered. Thus, there are no paths of easy ion movement in the oxide layers which also results in a slow oxidation rate [42].

In order to give a rough estimation of the film thickness d, we have analyzed the attenuation of the Co AES transition at 775 eV by the Al_2O_3 overlayer (Fig. 8.8). We use the formula:

$$I_{Co} = I^0_{Co} \cdot e^{\frac{-d_{Al_2O_3}}{\lambda_{Al_2O_3}(E_{Co})\cos\theta}} \tag{8.1}$$

with a mean free path $\lambda_{Al_2O_3}(E_{Co(775)}) = 17$ Å according to Ref. [126]. θ (= 42°)

represents the entrance angle of the CMA. From this, the thickness of oxide films grown by oxidation with 2000 L O_2 at 300 K is estimated to be 5 Å ± 0.5 Å. After direct oxidation at 1100 K with 2000 L O_2 the film has a thickness up to 10 Å ± 0.5 Å. Annealing at temperatures around 1500 K removes the oxygen from the surface.

Fig. 8.9 shows the $I_{O(510\ eV)}/I_{Al(1396\ eV)}$ p-to-p intensity as a function of oxygen exposure at 300 and 1100 K. A similar behaviour with that observed in the case of $Ni_3Al(100)$ oxidation occurs. At 300 K, a thin amorphous oxide is formed on the CoAl surface. As we shown above the thickness of this oxide amounts to ∼ 5 Å. Due to the contribution of Al atoms from the substrate, the I_O /I_{Al} ratio is smaller

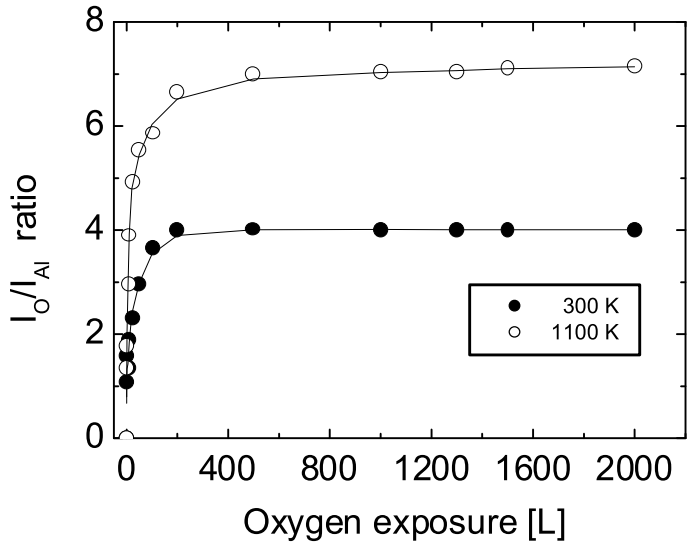

Figure 8.9: $I_{O(510\ eV)}/I_{Al(1396\ eV)}$ ratio as a function of oxygen exposure at 300 and 1100 K.

than the stoichiometric value. After an exposure of 2000 L O_2 the I_O /I_{Al} amounts to ∼ 4. In the case of oxidation at 1100 K the I_O /I_{Al} ratio increases with increasing oxygen exposure and after an exposure of ∼ 300 L O_2 it reach a value of ∼ 7 which correspond to the stoichiometric Al_2O_3 (see section 6.1). The I_O/I_{Al} found for Al_2O_3 grown on CoAl(100) is identical with those for alumina on $Ni_3Al(100)$,

which suggests that the composition of the oxide layer in both cases is the same, i.e. stoichiometric Al_2O_3. In the low exposure regime an island growth mechanism of the oxide is found by STM experiments (see section 8.2.4). This explain the lower value of the I_O/I_{Al} ratio for low exposure, when Al from the oxide-free areas contribute to the Al signal, but the actual I_O /I_{Al} ratio of a single Al_2O_3 island could not be determined.

8.2.2 The structure of the Al_2O_3 film

At 300 K, starting from the (1×1) pattern of the clean surface the diffraction spots became more and more diffuse with increasing oxygen exposure. At saturation level the substrate spots disappear completely and the LEED screen exhibits diffuse illumination. This indicates that the sample has lost long range order in the first atom layers perpendicular to the surface and the grown aluminum oxide layer is amorphous. A well ordered aluminum oxide layer can be prepared through annealing the oxygen saturated surface to 1000 K. Fig. 8.10a shows the LEED pattern of

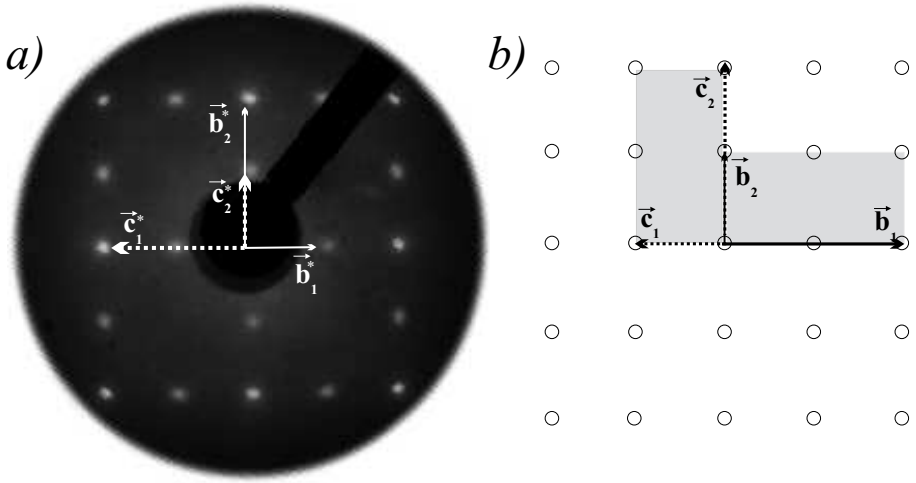

Figure 8.10: (a) LEED pattern of CoAl(100) surface after oxidation at 300 K with 2000 L O_2 and subsequently annealing at 1000 K showing a (2×1) structure (E_p = 65 eV); (b)The real space representation of the (2×1) structure.

the CoAl(100) surface after oxidation at 300 K with 2000 L O_2 and subsequently annealing at 1000 K. The pattern shows a (2×1) structure and is obtained from two domains oriented reciprocally perpendicular. $\vec{b}_1^*$, $\vec{b}_2^*$ and $\vec{c}_1^*$, $\vec{c}_2^*$ are the reciprocal vectors of the (2×1) structure corresponding to the first and second domain, respectively. Fig. 8.10b shows the real space representation of the basis vectors ($\vec{b}_1$, $\vec{b}_2$ and $\vec{c}_1$, $\vec{c}_2$) of the (2×1) structure with two domains. The unit cells of the two domains which are rotated with 90° are also shown. The (2×1) structure can be explained by the formation of the θ-Al_2O_3 phase. Fig. 8.11 shows a model of the

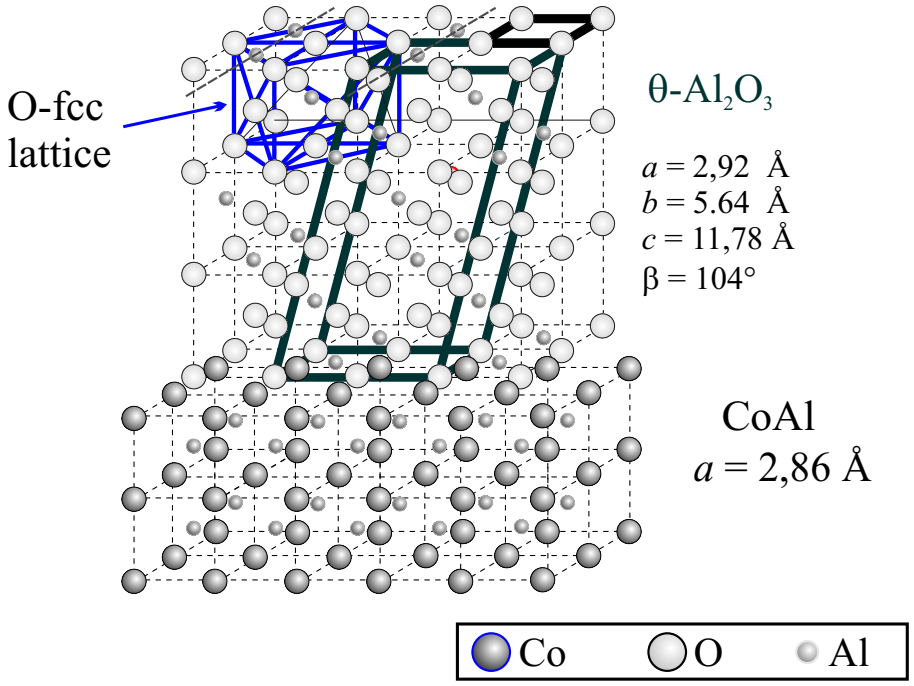

Figure 8.11: Structure model of θ - Al_2O_3/CoAl(100).

θ-Al_2O_3/CoAl(100) structure which illustrates the relationship between the oxygen-fcc sublattice and the CoAl(100)(bcc structure) substrate. The (110) plane of the fcc oxygen sublattice is perpendicular to the CoAl(100) surface and parallel to the CoAl[100] direction (or to the CoAl[010] direction for the second domain). This is the well-known Bain orientation relationship between bcc and fcc structures:

$$(100)_{\mathrm{CoAl}} \parallel (100)_{\text{O-sublattice}} \qquad \text{and} \qquad \begin{matrix}[100]_{\mathrm{CoAl}} \\ \\ [010]_{\mathrm{CoAl}}\end{matrix} \Bigg\| [110]_{\text{O-sublattice}}$$

The lattice constants of θ-Al_2O_3 agree very well with the (2×1) LEED pattern. The lattice mismatch only amounts to $\sim$ 1 % in one direction ($2 \cdot a_{\mathrm{CoAl}}$= 5.72 Å, $a_{\theta-Al_2O_3}$= 5.64 Å) and $\sim$ 2 % (b_{CoAl}=2.86 Å; $b_{\theta-Al_2O_3}$ = 2.91 Å) in the other direction. Thus, the θ-Al_2O_3 is compressed in one direction and expanded in the perpendicular direction.

After further annealing to higher temperatures, (1100 K < T < 1300 K) the LEED pattern (Fig. 8.12) shows streaks along the [100] and the [010] directions in addition to the (2×1) structure. The same LEED patterns are obtained by direct oxidation at corresponding temperatures. The presence of streaks in LEED patterns is usually assigned to a loss of order in the corresponding direction [11, 40, 82]. For Al_2O_3 grown on NiAl[100] another interpretation of this feature is also given [38]: using spot profile analysis of LEED (SPALEED) some satellite structure in the LEED pattern corresponding to a (9×1) superstructure were observed. A superstructure (n×1) periodicity, for larger n, gives always a LEED pattern with streaks. However in this case there is no perfect θ-Al_2O_3 layer on the CoAl(100) surface. It was found that the crystalline Al_2O_3 strips are embedded in re-grown NiAl terraces ($c(\sqrt{2} \times 3\sqrt{2})R45°$) and areas of ultrathin layers of amorphous Al-oxide which suggests a complicated interface structure favoring the formation of the Al_2O_3 stripes. In a surface X-ray diffraction study [127] on the oxidation of NiAl(100) surface, it was also found that the islands of θ-Al_2O_3 are embedded in a matrix of Al_2O_3 layers which show strong deviations from the pure θ-Al_2O_3 at the metal-oxide interface and at the oxide surface. Thus, the growth of a perfect ordered, pure θ-Al_2O_3 layer on NiAl(100), which produce a streaks-free (2×1) structure is somewhat complicated. The scenario described above for NiAl(100) is also valid for the oxidation of CoAl(100). As it was

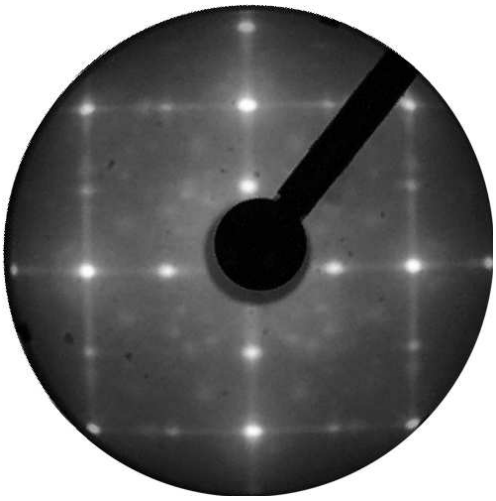

Figure 8.12: LEED pattern of CoAl(100) after oxidation with 2000 L O_2 and subsequently annealing at temperatures $\geq$ 1100 K (E_p = 65 eV).

shown above, it is possible to get a streaks-free (2×1) structure (Fig. 8.10) by oxidation at 1000 K. Higher oxidation temperatures ($\sim$ 1100 K) seems to induce a change in the order and, maybe leads to a mixture of θ-Al_2O_3 islands and oxide islands which deviate from the θ-Al_2O_3 structure and this could lead to a LEED pattern with streaks.

8.2.3 The vibrational properties of Al_2O_3/CoAl(100)

Fig. 8.13 shows a series of EEL spectra recorded as a function of oxygen exposure at 300 K. The spectrum (a) was recorded after an exposure of 0.8 L O_2. It exhibits two weak losses at 635 (ν_a) and 840 cm^{-1} (ν_b). With increasing oxygen exposure the high frequency mode grows faster and for exposure $\geq$ 20 L this mode is more intense than the mode ν_a. At saturation ($I_O/I_{Co} \sim 0.8$) the ratio of the relative intensities is $I(\nu_a)/I(\nu_b) = 2:3$, which is similar to that found for Al_2O_3 grown on Ni_3Al(100).

With increasing oxygen exposure a frequency shift to higher values is found: from 635 to 650 cm^{-1} for ν_a and from 840 to 890 cm^{-1} for ν_b. As it was discussed in section 6.2, the appearance of two modes in the EEL spectrum indicates that at

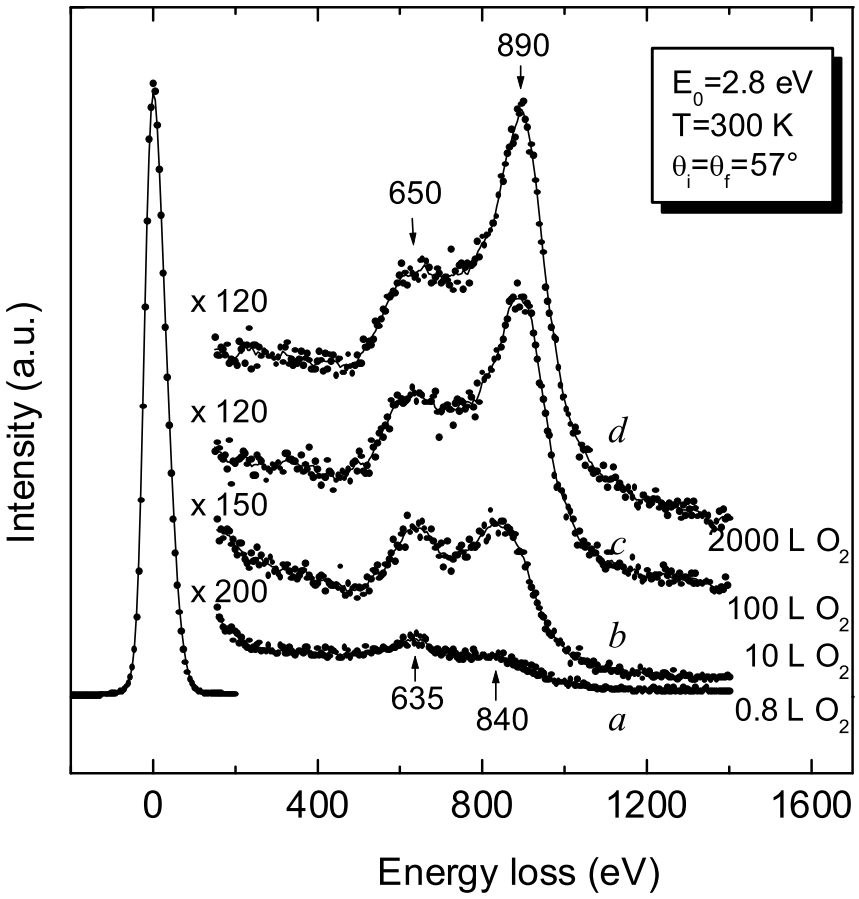

Figure 8.13: EEL spectra of amorphous alumina grown on CoAl(100) at 300 K.

300 K an amorphous Al_2O_3 (a-Al_2O_3) layer is formed. The frequencies of these two losses are in the range of amorphous Al_2O_3 layers (Table 6.1).

The LEED pattern corresponding to spectrum 8.13d is diffuse which support this conclusion. As it was already discussed in section 6.2, a-Al_2O_3 has a short range order and can be described as clusters of randomly oriented oxygen fcc lattices with Al cations solely occupying tetrahedral interstices. According to group theory two IR active modes are expected. Thus, we deduce that the spectra in Fig. 8.13 originate from a layer of amorphous aluminum oxide. The spectrum (d) in fig. 8.13 and the EEL spectrum obtained after oxidation at 300 K of $Ni_3Al(100)$ are similar regarding the relative intensity and the frequencies of the losses. These two modes

are characteristic for all a-Al_2O_3 layers grown on different surfaces of Ni-Al alloys (see Table 6.1). The calculated EEL spectrum shown in fig. 6.5 can also be compared with spectrum (d). It exhibits a good agreement with the experimental spectrum (d) in fig. 8.13. While the frequency of the ν_a mode is well reproduced, the frequency of the ν_b is shifted about 120 cm^{-1} to lower values in the calculated spectrum. This confirms our assumption that an a-Al_2O_3 film is grown on CoAl(100).

The phase transformation of the a-Al_2O_3 grown at 300 K was investigated as a function of the annealing temperature. First, the CoAl(100) surface was oxidized with 2000 L O_2 at 300 K, and afterwards gradually annealed. Each annealing step lasted for about two minutes. Fig. 8.14 shows EEL spectra taken after annealing at the indicated temperatures. After annealing at 500 K the loss feature is similar to that found at 300 K, only the intensity is slightly increased. After annealing at 600 K a different spectrum occurs which exhibits three losses at 415, 630 and 905 cm^{-1}. This indicates a transition from a-Al_2O_3 to a different phase of the oxide film. As mentioned in section 4.1 there is a phase transition to γ-Al_2O_3 at about 700 K in the thermal dehydration sequence of boehmite and of trihydroxides in vacuum. This involves an alteration of the occupation probability of the tetrahedral and octahedral vacancies in the oxygen sub-lattice. In γ-Al_2O_3 the Al ions occupy both tetrahedral and octahedral sites, whereas in a-Al_2O_3 only the tetrahedral vacancies are occupied. The change in occupancies accounts for the changes in the EEL spectra. Although the losses are quite broad, they are more intense than those of a-Al_2O_3. Also, the FWHM of the losses decreases as the annealing temperature increases. This indicates a higher level of ordering within the oxide layer which is clearly shown after annealing to 900 K. On the other hand it is also possible that in the temperature range between 600 and 900 K a - Al_2O_3 is transformed into disordered clusters (islands) of θ - Al_2O_3, in which also both vacancies (tetrahedral and octahedral) are occupied by Al^{3+} ions. In this work it was not possible to clarify exactly which Al_2O_3 is formed in the transition temperature range. For simplicity, in Fig. 8.14 a γ-like-Al_2O_3 is assumed which is the explanation for the phase transformation of Al_2O_3

on NiAl(100) [82]. Therefore, we propose a γ-like phase for this temperature range

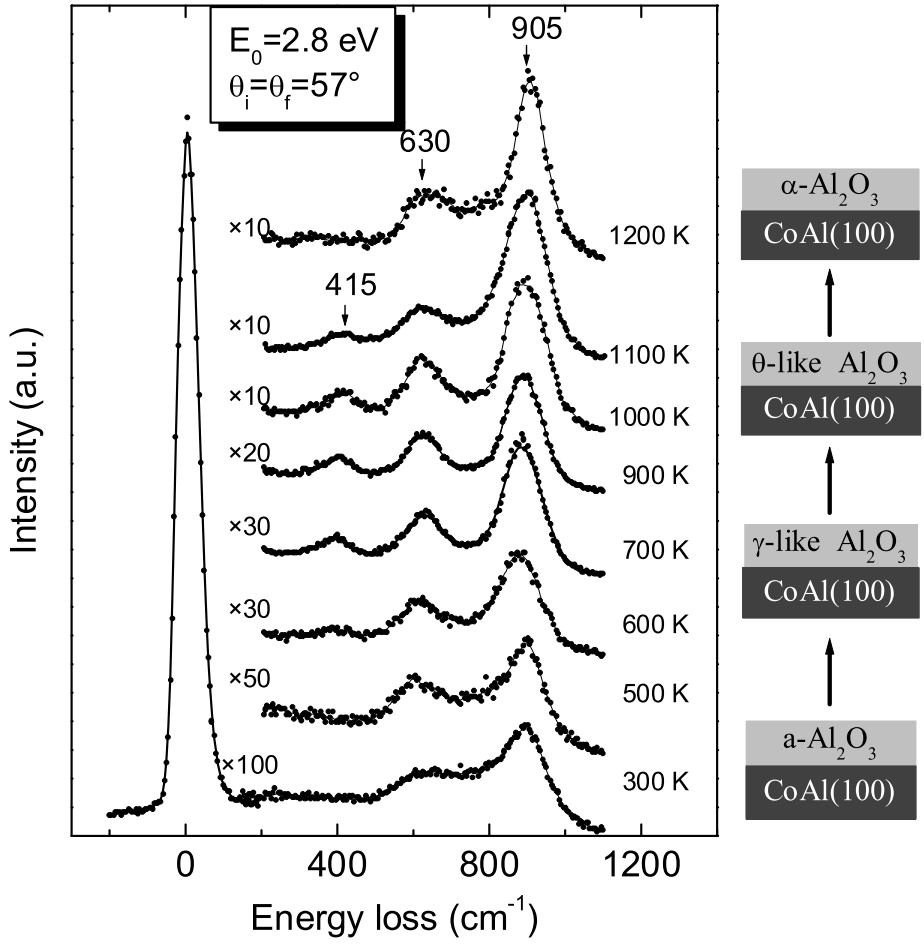

Figure 8.14: A series of EEL spectra of CoAl(100) surface oxidized with 2000 L O_2 at 300 K as a function of annealing temperature. The corresponding phase transformation is sketched on the right side of the figure.

(600 K < T < 900 K). The higher the annealing temperature, the higher the sharpness and the intensity of the losses. After annealing at 1000 K the three-peak structure is conserved, only a small increase of the intensity is found. LEED investigations have shown that in this temperature range the θ - Al_2O_3 phase is growing. Therefore another phase transformation: γ-like-$Al_2O_3 \longrightarrow \theta$ - Al_2O_3 takes place. The EEL spectrum found after annealing (or direct oxidation) at $\sim$ 1000 K is very similar to

that found for $Al_2O_3/Ni_3Al(100)$ (see section 6.2) and $Al_2O_3/NiAl(100)$ [82]. These EEL spectra can be fitted by calculations based on the dielectric theory, using the IR parameters of Al_2O_3. Thus, the formation of Al_2O_3 on the CoAl(100) is confirmed and was also expected from the point of view of thermodynamics because the heat of formation $\Delta H_{Al_2O_3} = 1690$ kJ/mol [128] is much higher that of Co-oxide $\Delta H_{Co_3O_4} = 892$ kJ/mol [129]. Annealing at 1100 K leads to a decrease of the intensity of the three losses. After annealing at 1200 K a new loss feature occurs consisting in only two modes located at 630 and 905 cm^{-1}. We suppose a transition from θ-Al_2O_3 to an α-like Al_2O_3, since α-Al_2O_3 is the only high-temperature phase of alumina. This transition is related with a change of the occupation probability of the octahedral and tetrahedral vacancies. As already discussed in section 6.2 for θ-Al_2O_3, both octahedral and tetrahedral sites are occupied; in α-Al_2O_3 the Al ions solely occupy the octahedra positions. This leads to only two modes in the EEL spectrum. The position of the losses is in agreement with those found for α-Al_2O_3 on NiAl(100) and NiAl(111) (see table 6.1). On the right side of the spectra the phase transformation of the Al_2O_3 layer during annealing is indicated. The same phase transformation of a-Al_2O_3 was found for $Al_2O_3/NiAl(100)$ [82].

8.2.4 The morphology of Al_2O_3 grown on CoAl(100)

The STM measurements presented in this chapter were performed after oxidation of CoAl(100) surface directly at 1000 K and 1100 K. They offer an overview on the first steps of CoAl(100) surface oxidation at high temperature. However, further experiments are necessary in order to study the amorphous oxide and phase transformation during annealing.

- *The structure of the alumina layer*

Fig. 8.15 shows two STM images taken on the CoAl(100) surface after oxidation with 10 L O_2 at 1000 K. Fig. 8.15a shows a STM image with an area of 424×212 $Å^2$. The formation of strongly anisotropic domains, with a rectangular shape, oriented

reciprocally perpendicular can be clearly observed. The domains are characterized

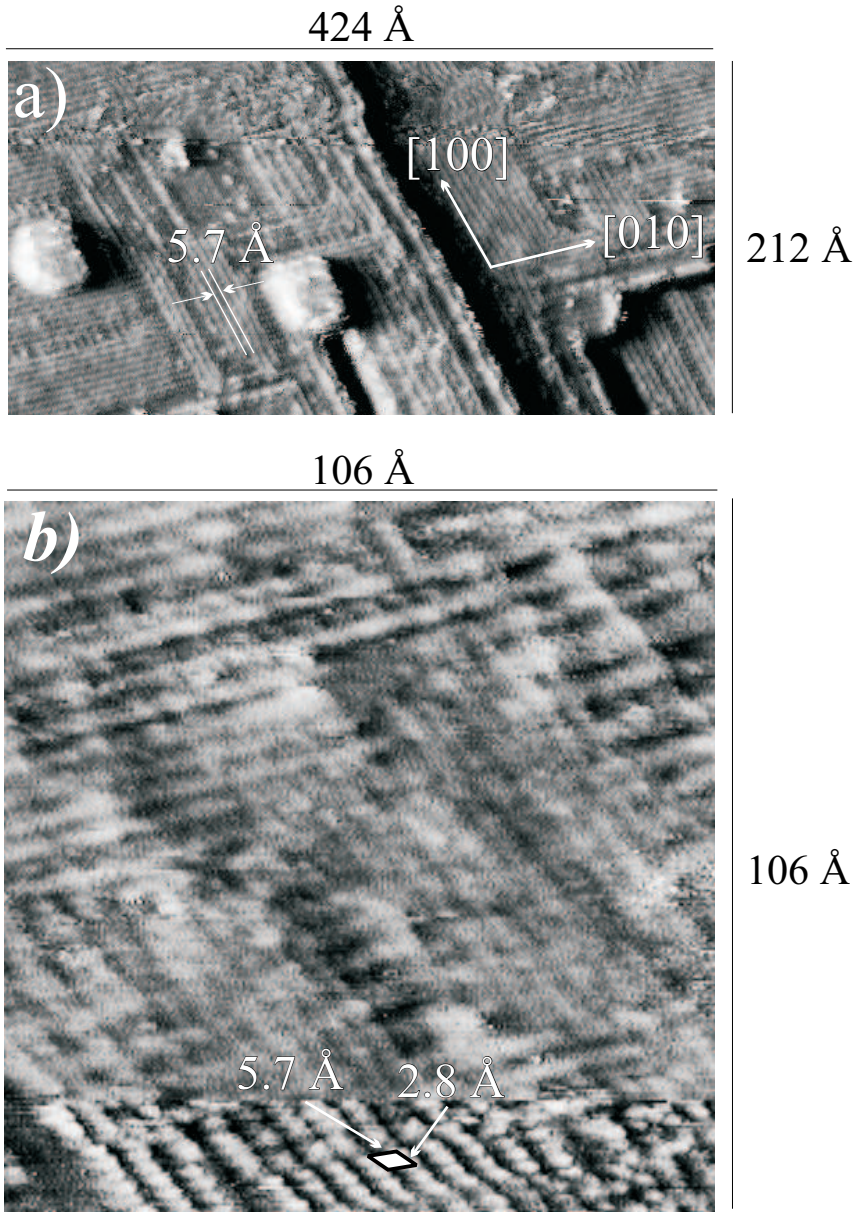

Figure 8.15: STM images of CoAl(100) surface oxidized with 10 L O_2 exposure at 1100 K (U_t = -2 V; I_t = 0.2 nA).

by parallel strips along the [001] and [010] direction, respectively. The spacing between the strips amounts to 5.7 Å which corresponds to 2 × a_{CoAl}. In fig. 8.15b a rectangular unit cell can be observed with the lengths of the basis vectors a ∼ 2.8 Å

and b $\sim$ 5.7 Å. Such a unit cell is expected from the top layer of θ-Al_2O_3 and explains the (2×1) structure observed by LEED (Fig. 8.10). In each oxygen layer of θ-Al_2O_3 the Al-ions form chains with a distance of 5.7 Å. Thus, the streaks in the STM images can be connected with the aluminum chains (or Al-missing chains). The protrusions should be attributed to the oxygen O^{2-} ions which forms a (2×1) missing rows structure after oxidation at this temperature. Therefore, it is more likely that in the STM images the strips are due to the rows where aluminum is missing. A similar situation was observed by Franchy et al. [130] for β-Ga_2O_3. The authors associated the Ga-missing rows with a depletion of charge of Ga due to the electrons transfer to O during oxidation. β-Ga_2O_3 and θ-Al_2O_3 are isomorphic, and therefore this explanation may holds also for θ-Al_2O_3/CoAl(100).

- *The initial states of oxidation*

Fig. 8.16a-d shows four STM images of CoAl(100) surfaces oxidized with a different amount of oxygen at 1100 K. The large scanned area (3400×3400 $Å^2$) offer an overview on the elemental steps of oxide growth. Fig. 8.16a-d show STM image from different areas on the surface. The reason for this is that for oxidation at 1100 K, the STM has to be removed from the sample and after cooling the sample to 300 K the same position on the sample cannot be found. Fig. 8.16a shows the CoAl(100) surface after oxidation with 0.5 L O_2 at 1100 K. The pressure was maintained during oxidation in this case at 5×10^{-9} mbar. This image exhibits five terraces separated by four steps. Already at this small exposure the rearrangement of the steps can be recognized. The shape of the step edges is changed in comparison with that observed for the clean surface (fig. 8.4). In fig. 8.16a only rectangular angles are found on the steps between two terraces. Long features, reciprocally perpendicular evidenced by "Ox" and white lines, are developed starting from the step edges along the terraces. The unoxidized surface of the terraces is marked by "T". The step height amounts to $\sim$ 3 Å which shows that the oxidation takes place on both terraces in the same way.

Fig. 8.16b shows a STM image of the CoAl(100) surface after oxidation with 1 L O_2

at 1100 K. In this image three terraces are separated by two steps. The oxide islands have a long, rectangular shape and start preferentially from step edges (ex.: areas marked with *Ox* in Fig. 8.16b). However, some isolated oxide islands are formed

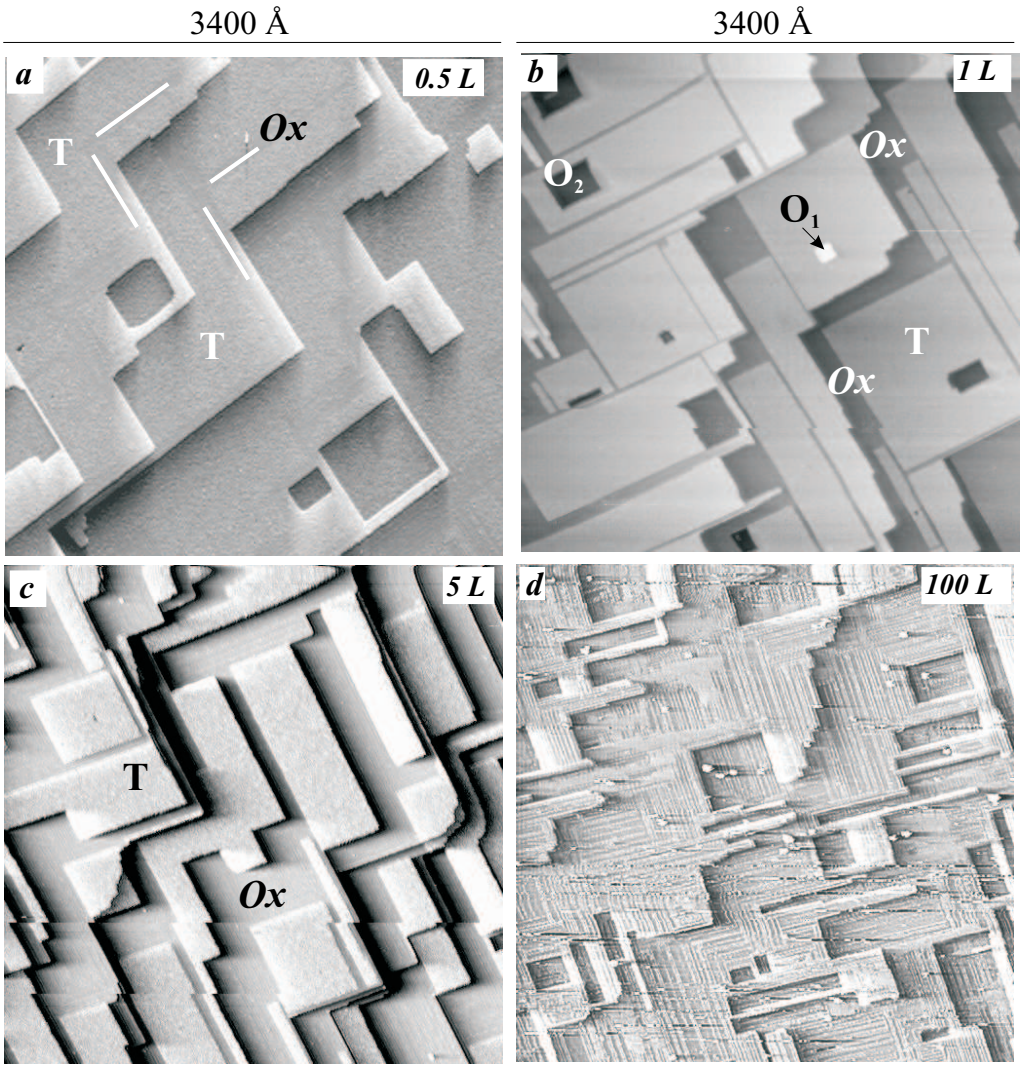

Figure 8.16: Large area STM images of the oxidized CoAl(100) surface. The oxygen exposure is indicated in each figure. The tunnelling parameters were: (a) $U_t = 2.2$ V; $I_t = 0.3$ nA (b) $U_t = 2.26$ V; $I_t = 0.2$ nA (c) $U_t = 1.81$ V; $I_t = 0.2$ nA (d) $U_t = 2.5$ V; $I_t = 0.2$ nA.

on the terraces (O_1, O_2). These oxide islands grow in two domain reciprocally

perpendicular. The area occupied by oxide in this case is ∼ 8%. Fig. 8.16c shows

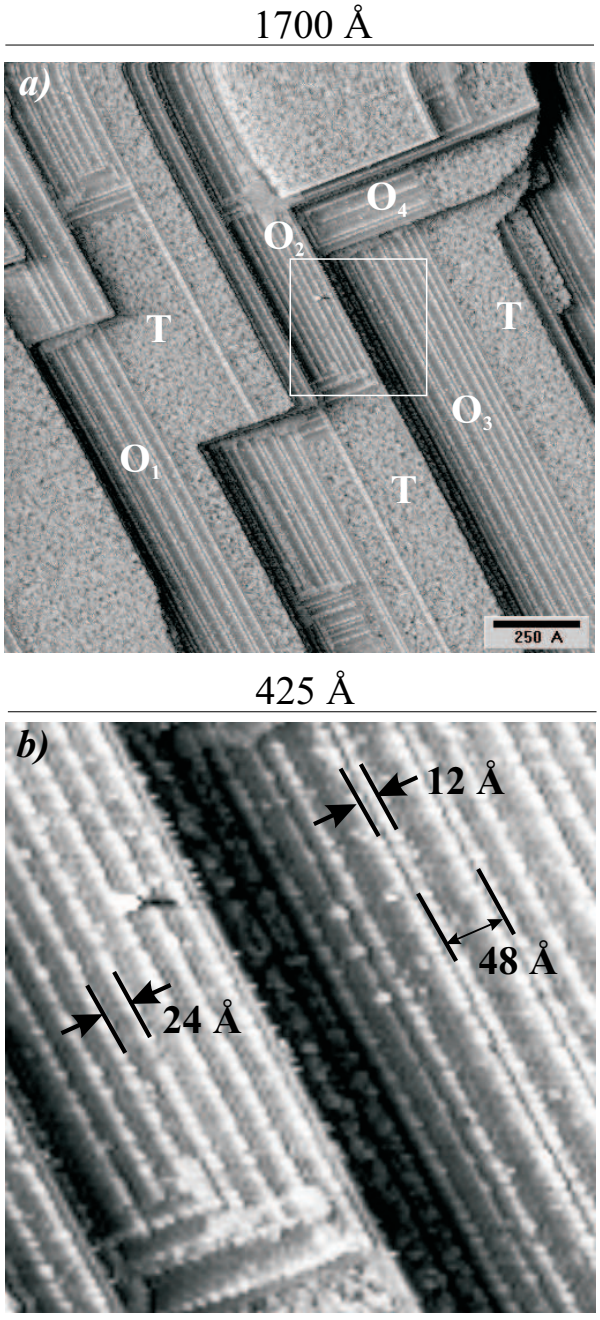

Figure 8.17: STM images of Al_2O_3/CoAl(100) after exposure of 3 L O_2 at 1100 K (U_t = - 2.5 V; I_t = 0.2 nA).

a STM image of the CoAl(100) surface after oxidation with 5 L O_2 at 1100 K. The

oxidized area ("Ox") in this case amounts to $\sim$ 40 %. Two steps which separate three terraces can be recognized. On all terraces the oxide islands have still the long, rectangular shape. "T" represents an area of the clean CoAl(100) surface.

Fig. 8.16d shows the CoAl(100) surface after exposure to 100 L O_2 at 1100 K. The oxide domains are very well visible over the whole surface. They are crossed by streaks which are parallel to the domain orientation. From these STM pictures we conclude that the growth of the Al_2O_3 on CoAl(100) presents many similarities with the growth of θ-Al_2O_3 on NiAl(100) [122] and with β-Ga_2O_3 on CoGa [130]. The reason of the strong anisotropy of the oxide islands was not clarified. In the case of Al_2O_3 grown on NiAl(100) [122] the authors have suggested as a possible reason the internal build up of stress during the growth and ordering process.

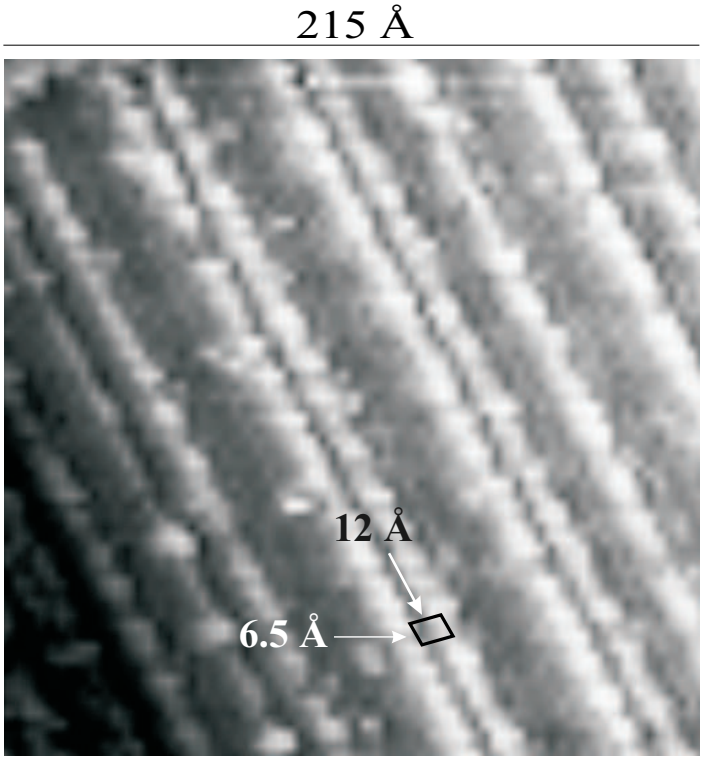

Figure 8.18: STM image of Al_2O_3/CoAl(100) after exposure of 3 L O_2 at 1100 K (U_t = - 2.5 V; I_t = 0.2 nA).

Fig. 8.17a shows a STM image with a scanned area of 1700 $\times$ 1700 Å^2 of the surface

after oxidation with 3 L O_2 at 1100 K. Several oxide domains (O_1, O_2, O_3, O_4) can be recognized. The domains O_1, O_2 and O_3 are aligned in the same direction while O_4 is perpendicular to this direction. The domains are crossed by double and single strips (on the domains O_1 and O_3) or only single strips (domain O_2). The free of oxide area of the terraces are marked with "T". Fig. 8.17b shows the STM image of the section marked with the square in fig. 8.17a. In this figure the distance between the double strips is $\sim$ 12 Å, while between the single strips the distance amounts $\sim$ 24 Å.

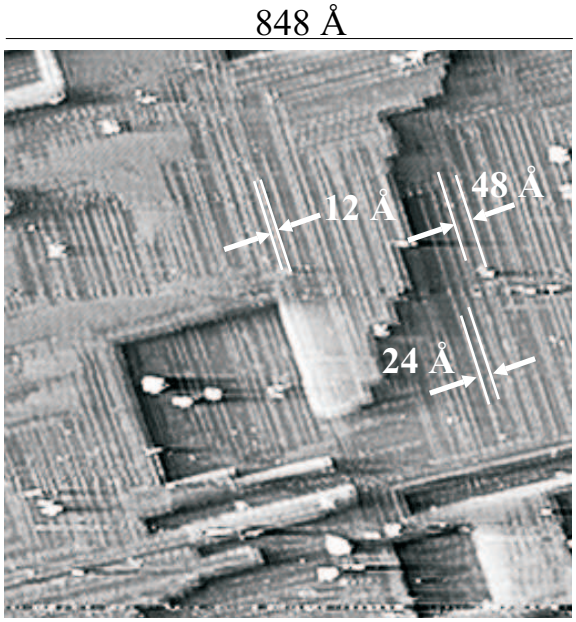

Figure 8.19: STM image of Al_2O_3/CoAl(100) after 100 L O_2 exposure at 1100 K (U_t = - 1.5 V; I_t = 0.2 nA).

The center-to center distance of the double strips amounts to 48 Å. After zooming in (see fig. 8.18), the corrugation along the double strips is clearly observed and is determined to be $\sim$ 6.5 Å. This gives a unit cell mesh of 12×6.5 Å which represents a superstructure of the oxide surface. With respect to the (100) surface of CoAl, the (12×6.5) unit mesh can be interpreted as a distorted (4×2) reconstruction, while with respect to the top layer of θ-Al_2O_3 a distorted (2×1) reconstruction results.

Fig. 8.19 shows a STM image with a scanned area of 848×848 Å of the CoAl(100) surface after exposure to 100 L O_2 at 1100 K. In this case the whole surface displays oxide domains, reciprocally perpendicular which are crossed by strips. The distance between the strips amounts 12 Å or a multiple of this distance, i.e. 24 Å or 48 Å. The shape of the strips and the distance between the strips are very similar with those found in the case of Al_2O_3 grown on the NiAl(100) surface [122]. In this case the authors have found oxide strips with an average width of 27 Å and with a centre-to-centre distance of 45 Å. Based on the SPALEED and STM measurements they conclude that the oxide surface consist of antiphase domains with a (9×1) superstructure containing (2×1) units.
In the STM investigations described above no evidences were found for a (n×1) structure which would explain the streaks observed in the LEED pattern (fig. 8.12).

8.3 Summary

In this chapter preliminary results of the elemental steps of the oxidation CoAl(100) are presented. Oxygen adsorption on CoAl(100) leads to the formation of thin aluminum oxide layers. The law of the growth rate is of logarithmic type. The structure and phases of these oxide films are determined mainly by the oxidation temperature. At room temperature the formation of an amorphous aluminum oxide is found. By annealing in the temperature range between 800-1000 K the a-Al_2O_3 is transformed into the θ–Al_2O_3 phase, which exhibits a (2×1) structure. After annealing at temperatures > 1200 K a transition to α-Al_2O_3 occurs. Upon annealing at temperatures $T > 1300$ K the Al_2O_3 film is removed from the surface and the clean CoAl(100) surface is found.

Summary

The aim of this work was the preparation and characterization of thin oxide films on the low indexed surface of intermetallic compounds $Ni_3Al(100)$ and CoAl(100), as well as the study of Co growth on the clean and oxidized $Ni_3Al(100)$ surface.

- The clean $Ni_3Al(100)$ surface

The LEED pattern of clean $Ni_3Al(100)$ shows a (1×1) structure. STM images of the $Ni_3Al(100)$ surface display flat and large terraces (500 - 1000 Å) separated by steps. The step height amounts to 3.5 Å which corresponds to the lattice constant of Ni_3Al and represents a double atomic step. This suggest that different terraces have always the same termination.

- Co/$Ni_3Al(100)$

At low coverage (0.1 ML) and 300 K, cobalt deposited on $Ni_3Al(100)$ surface shows two-dimensional growth. For deposition of 0.3 ML the nucleation takes also place in the second layer. The surface of 3.5 ML Co deposited at 300 K displays a morphology of islands with a mean diameter of $\sim$ 90 Å. This configuration is unstable with regard to annealing which drive the system into an equilibrium configuration of large and flat islands. After annealing at 700 K a fcc structure is stabilized, Co growing with the (100) plane parallel to the substrate. The Co film is stable on $Ni_3Al(100)$ surface up to 750 K when it starts to diffuse into the substrate. At 1100 K, Co is disappeared completely from the surface via diffusion into the substrate.

- Al_2O_3/$Ni_3Al(100)$

At room temperature the oxygen adsorption on $Ni_3Al(100)$ leads to the formation of a thin amorphous aluminum oxide layer ($\sim$ 5 Å). Annealing an oxide covered

surface at 1100 K, leads to a well ordered γ'-Al_2O_3 film. Oxidation directly at 1100 K also leads to the formation of a well ordered γ'-Al_2O_3. The thickness of the oxide film prepared at 1100 K is $\sim$ 10 Å. The STM experiments performed on $Ni_3Al(100)$ surface oxidized at 1100 K show an island growth mode of the oxide. The completely oxide covered surface shows two superstructures with the lattice constants of 18 Å and 54 Å. The band-gap of ultrathin amorphous and well-ordered Al_2O_3 formed on $Ni_3Al(100)$ are strongly diminished with respect to the bulk values. The lowering of band-gap values of thin alumina films on Ni_3Al is explained with the existence of defects induced states located in the band-gap region. The oxidation in higher O_2 pressure range (p $\geq$ 5×10−6 mbar) leads to a thicker oxide layer which shows a (1×1) structure for an exposure $\geq$ 2000 L O_2.

- **$Co/Al_2O_3/Ni_3Al(100)$**

Co deposited at room temperature on $Al_2O_3/Ni_3Al(100)$ shows a three dimensional (Volmer-Weber) growth mode. After a nominal deposition of 30 Å the cobalt film has a roughness of $\sim$ 10 Å. Annealing of the film at 700 and 900 K leads to the coalescence of Co clusters, and to a gradually diffusion of Co through the oxide into the substrate. The decrease of the Co film thickness is confirmed also by AES experiments. After annealing at 1000 K Co is disappeared from the surface.

- **$Al_2O_3/CoAl(100)$**

Oxygen adsorption on CoAl(100) leads to the formation of a thin aluminum oxide layers. The structure and phases of these oxide films are determined mainly by the oxidation temperature. At room temperature the formation of an amorphous aluminum oxide is found. By annealing in the temperature range between 800-1000 K a-Al_2O_3 is transformed into the θ-Al_2O_3 phase, which exhibits a (2×1) structure. Oxidation at 1100 K leads likewise to a (2×1) structure with respect to the substrate. After annealing at temperatures $>$ 1200 K a transition to the α-Al_2O_3 phase occurs. Upon annealing at temperatures T $>$ 1300 K the Al_2O_3 film is removed from the surface and the clean CoAl(100) surface is found.

Bibliography

[1] R. Franchy, Surf. Sci. Rep. **38**, 199 (2000).

[2] J. S. Moodera, L. R. Kinder, T. M. Wong, and R. Meservey, Phys. Rev. Lett. **74**, 3273 (1995).

[3] T. Miyazaki and N. Tezuka, J. Magn. Magn. Mater. **139**, L231 (1995).

[4] J. Slaughter, E. Chen, R. Whig, B. Engel, J. Janesky, and S. Tehrani, JOM **52**, 16 (2000).

[5] W. Chen and H. Ahmed, J. Vac. Sci. Technol. B **15**, 1402 (1999).

[6] L. Schelp, A.Fert, F. Fettar, P. Holody, S. Lee, J.-L. Maurice, F. Petroff, and A. Vaurés, Phys. Rev. B **56**, R5747 (1997).

[7] R. Desmicht, G. Faini, V. Cros, A. Fert, F. Petroff, and A. Vaurés, Phys. Rev. B **72**, 386 (1998).

[8] G. Binasch, P. Grünberg, F. Saurenbach, and W. Zinn, Phys. Rev. B **39**, 4828 (1989).

[9] N. Kobayashi, S. Ohnuma, S. Murakami, T. Masumoto, S. Mitani, and H. Fujimori, J. Magn. Magn. Mater. **188**, 30 (1998).

[10] J.-L. Maurice, J. Briático, J. Carrey, F. Petroff, L. Schelp, , and A. Vaurés, Phil. Mag. **A79**, 2921 (1999).

[11] G. Ertl and J. Küppers, *Low Energy Electrons and Surface Chemistry* (VCH Verlagsgesellschaf GmbH, Berlin, 1985).

[12] K. Kliewer and R. Fuchs, Adv. Chem. Phys. **27**, 355 (1974).

[13] P. Lambin, J.-P. Vigneron, and A. Lucas, Phys. Rev. B **32**, 8203 (1985).

[14] H. Ibach and D. L. Mills, *Electron Energy Loss Spectroscopy and Surface Vibrations* (Academic Press, New York, 1982).

[15] H. Lüth, *Surfaces and Interfaces of Solids*, 3 ed. (Springer-Verlag, Berlin, 1993).

[16] L.-M. Yu, P. Thiry, T. C. A. Degiovanni, and R. Caudano, Phys. Rev. B **49**, 11613 (1994).

[17] P. Lambin, J.-P. Vigneron, and A. Lucas, Comp. Phys. Commun. **60**, 351 (1990).

[18] P. Senet, P. Lambin, J. P. Vigneron, I. Derycke, and A. A. Lucas, Surf. Sci. **226**, 307 (1990).

[19] K. Kliewer and R. Fuchs, Phys. Rev. **144**, 495 (1966).

[20] G. Binnig, H. Rohrer, C. Gerber, and E. Weibel, Phys. Rev. Lett. **40**, 57 (1982).

[21] R. Gomer, *Interaction on Metals Surface* (Springer-Verlag, Berlin, 1975).

[22] G. Somorjai, *Chemistry in two dimension: Surface*, 1 ed. (Cornell University Press, Ithaca and London, 1981).

[23] M. Seah and W. Dench, Surf. Interf. Analysis **1**, 2 (1979).

[24] C. Davisson and L. Germer, Phys. Rev. **30**, 705 (1927).

[25] C. Davisson and L. Germer, Rev. Sci. Inst. **31**, 112 (1960).

[26] E. Wood, J. Appl. Phys. **35**, 1306 (1964).

[27] E. Bauer, Z. Kristallogr. **110**, 372 (1958).

[28] E. Bauer and H. Poppa, Thin Solid Films **12**, 167 (1972).

[29] F. Frank and J. Merwe, Proc. Roy. Soc. London **A198**, 216 (1949).

[30] M. Volmer and A. Weber, Z. Physik. Chem. **119**, 277 (1926).

[31] I. Stransky and L. Krastanow, Sitz. Ber. Akad. Wiss., Math.-naturwiss. Kl. Abt. IIb **146**, 797 (1938).

[32] A.-L. Barabasi and H. Stanley, *Fractal Concepts in Surface Growth* (Cambridge University Press, Cambridge, 1995).

[33] K.-H. Meiwes-Broer, *Metal Cluster at Surfaces: Structure, Quatum Properties, Phisical Chemistry* (Springer-Verlag, Berlin, 2000).

[34] J. Villain, J. Phys.(Paris) **1**, 19 (1991).

[35] V. Henrich and P. Cox, *The surface science of metal oxide*, 1 ed. (Cambridge University Press, Cambridge, 1994).

[36] H.-J. Freund, H. Kuhlenbeck, and V. Staemmler, Rep. Prog. Phys. **59**, 283 (1996).

[37] R. Franchy, J. Masuch, and P. Gassmann, Appl. Surf. Sci. **93**, 31 (1996).

[38] R.-P. Blum, D. Ahlbehrendt, and H. Niehus, Surf. Sci. **396**, 176 (1998).

[39] R.-P. Blum, D. Ahlbehrendt, and H. Niehus, Surf. Sci. **366**, 107 (1996).

[40] H. Graupner, L. Hammer, K. Heinz, and D. M. Zehner, Surf. Sci. **380**, 335 (1997).

[41] G. Schmitz, P.Gassmann, and R. Franchy, Surf. Sci. **397**, 339 (1998).

[42] F. P. Fehlner, *Low-Temperature Oxidation - The Role of Vitreous Oxides* (John Wiley & Sons, New York, 1986).

[43] C. Wagner, Z. Physik. Chem. B **21**, 25 (1933).

[44] N. Cabrera and N. F. Mott, Rep. Prog. Phys. **12**, 163 (1948).

[45] H. Ibach, *Electron Energy Loss Spectrometer, The Technology of High Performance*, Vol. 63 of *Springer Series in Optical Science* (Springer-Verlag, Berlin, 1991).

[46] K. Besocke, Surf. Sci. **181**, 145 (1987).

[47] *Handbook of Auger Electron Spectroscopy*, Physical Electronics Industries, 1976.

[48] B. Lippens and S. Steggerda, *Physical and Chemical Aspects of Absorbants and Catalysts* (Academic Press, New York, 1970).

[49] Y. T. Chu, C. W. W. J. B. Bates, and G. C. Farlow, J. Appl. Phys. **64**, 3727 (1988).

[50] H. J. van Beek and E. J. Mittermeijer, Thin Solid Films **122**, 131 (1984).

[51] W. Pies and A. Weiss, in *Landolt-Börnstein, Zahlenwerte und Funktionen aus Naturwissenschaft und Technik*, edited by K. Hellwege and A. M. Hellwege (Springer-Verlag, Berlin, 1975), Vol. III/7b.

[52] J. H. Westbrook, *Intermetallic compounds: principles and practice* (John Wiley & Sons, Chichester, 1994), Vol. 1.

[53] A. Taub and R. Fleischer, Science **243**, 616 (1989).

[54] T. B. Massalski, *Binary alloy phase diagrams*, 2 ed. (William W. Scott jr., ASM International, 1992).

[55] N. Baluc, J. Bonneville, K. J. Hemker, J. L. Martin, R. Schublin, and P. Spätig, Mat. Sci. Eng. A **164**, 383 (1993).

[56] G. Saada and P. Veyssière, Structural Intermetallics - Proceedings of the First International Symposion on Structural Intermetallics **1**, 379 (1993).

[57] D. Sondericker, F. Jona, and P. M. Marcus, Phys. Rev. B **33**, 900 (1986).

[58] M. Foiles and M. S. Daw, J. Mater. Res. **2**, 5 (1987).

[59] V. Kuznetsov, R. Kadyrov, and G. Rudenskii, J. Mater. Sci. Technol. **14**, 320 (1998).

[60] R. Kobistek, G. Bozzolo, J. Ferrante, and H. Schlosser, Surf. Sci. **307-309**, 390 (1994).

[61] A. Paciaroni, C. Petrillo, and F. Sacchetti, J. Phys.(Paris) **7**, 865 (1997).

[62] E. Wachtel, V. Linse, and V. Gerold, J. Phys. Chem. Solids **34**, 1461 (1973).

[63] A. Bradley and G. Seager, J. Inst. Met. **64**, 81 (1937).

[64] M. Cooper, Phil. Mag. **89**, 805 (1963).

[65] D. Sellmyer, G. Casey, and J. Franz, J. Phys. Chem. Solids **33**, 561 (1972).

[66] J. Rhee, Y. Kudryavstev, K. Kim, and Y. Lee, J. Phys. Chem. Solids **87**, 5887 (2000).

[67] G. Sauthoff, *Intermetallics* (VCH Verlagsgesellschaf GmbH, Weinheim, 1995).

[68] P. Mrozek, M. Menyhard, J. Wernisch, and A. Jablonski, Phys. Stat. Sol. A **84**, 39 (1984).

[69] S. Tanuma, C. Powell, and D. Penn, Surf. Interf. Analysis **17**, 911 (1991).

[70] B. Degroote, H. Pattyn, S. Degroote, A. Vantomme, J. Dekoster, and G. Langouche, Thin Solid Films **380**, 111 (2000).

[71] H. Brune, Surf. Sci. Rep. **31**, 121 (1998).

[72] G. Reiss, J. Vancea, H. Wittmann, J. Zweck, and H. Hoffmann, J. Appl. Phys. **67**, 1156 (1990).

[73] D. Bürgler, C. Schmidt, D. Schaller, D. Meisinger, and H.-J. Güntherodt, Phys. Rev. B **56**, 4149 (1997).

[74] J. Bland, A. Johnson, R. Bateson, and H. Lauter, J. Magn. Magn. Mater. **104-107**, 1798 (1992).

[75] N. S. Stoloff, C. T. Liu, , and S. C. Deevi, Intermetallics **8**, 1313 (2000).

[76] S. Street, C.Xu, and D. Goodman, Annu. Rev. Phys. Chem. **48**, 43 (1999).

[77] S. Addepalli, B. Ekstrom, N. Magtoto, J.-S. Lin, and J. Kelber, Surf. Sci. **442**, 385 (1999).

[78] C. Becker, K. von Bergmann, A. Rosenhahn, J. Schneider, and K. Wandelt, Surf. Sci. **486**, L443 (2001).

[79] D. R. Lide(Ed.), *CRC Handbook of Chemistry and Physics* (FL, Boca Raton, 1994), Vol. 9/123.

[80] A. Venezia and C. Loxton, Surf. Sci. **194**, 136 (1988).

[81] U. Bardi, A. Atrei, and G. Rovida, Surf. Sci. **268**, 87 (1992).

[82] P. Gassmann, R. Franchy, and H. Ibach, Surf. Sci. **319**, 95 (1994).

[83] S. Tanuma, C. Powell, and D. Penn, Surf. Interf. Analysis **17**, 927 (1991).

[84] R. M. Jaeger, H. Kuhlenbeck, H.-J. Freund, M. Wuttig, W. Hoffmann, R. Franchy, and H. Ibach, Surf. Sci. **259**, 235 (1991).

[85] C. Becker, J. Kandler, H. Raaf, R. Linke, T. Pelster, M. Drger, M. Tanemura, and K. Wandelt, J. Vac. Sci. Technol. A **16**, 1000 (1998).

[86] M. Liehr, P. Thiry, J. Pireaux, and R. Caudano, J. Vac. Sci. Technol. A **2**, 1079 (1959).

[87] G. Schmitz, P. Gassmann, and R. Franchy, J. Appl. Phys. **83**, 2533 (2000).

[88] R. L. Strong and J. L. Erskine, Phys. Rev. B **25**, 5547 (1982).

[89] J. J. Rechtien, C. R. Kannewurf, and J. O. Brittain, J. Appl. Phys. **38**, 3045 (1967).

[90] H. Ibach, H. D. Bruchmann, and H. Wagner, Appl. Phys. A **29**, 113 (1982).

[91] D. Ignatov, C.R. Acad. Sci. USSR **54**, 329 19 (1946).

[92] A. Kalinina, Russian Journal of Inorganic Chemistry **4**, 568 (1959).

[93] M. Gautier, J. P. Duraud, L. P. Van, and M. J. Guittet, Surf. Sci. **250**, 71 (1991).

[94] F. S. Ohuchi and R. H. French, J. Vac. Sci. Technol. A **6**, 1695 (1987).

[95] W. J. Gignac, R. S. Williams, and S. P. Kowalczyk, Phys. Rev. B **32**, 1237 (1985).

[96] B. Ealet, M. H. Elyakhloufi, E. Gillet, and M. Ricci, Thin Solid Films **250**, 92 (1994).

[97] A. Jimenéz-Gonzales and D. Schmeisser, Surf. Sci. **250**, 59 (1991).

[98] S. Andersson, P. A. Brhwiller, M. F. A. Sandell, J. Libuda, A. Giertz, B. Brena, M. B. A. J. Maxwell, H.-J. Freund, and N. Mrtensson, Surf. Sci. **442**, L964 (1999).

[99] A. Bianconi, R. Z., Bachrach, S. H. Hagstrom, and S. A. Flodström, Phys. Rev. B **19**, 2837 (1979).

[100] S. Ciraci and I. P. Batra, Phys. Rev. B **28**, 982 (1983).

[101] F. Bartolucci, G. Schmitz, P. Gassmann, and R.Franchy, J. Appl. Phys. **10**, 6467 (1996).

[102] N. F. Mott and E. A. Davis, *Electronic Processes in Non-Crystalline Materials*, 2 ed. (Clarendon Press, Oxford, 1979).

[103] N. F. Mott, Adv. Phys. **16**, 49 (1967).

[104] N. F. Mott, Phil. Mag. **17**, 1259 (1968).

[105] T. Bertrams, A. Brodde, and H. Neddermeyer, J. Vac. Sci. Technol. B **12**, 2122 (1994).

[106] K. H. Hansen, E. L. T. Worren, F. Besenbacher, and I. Stensgaard, Surf. Sci. **475**, 96 (2001).

[107] G. Schmitz, Ph.D. thesis, Universitt Düsseldorf, 1999.

[108] T. Bertrams, A. Brodde, H. Hannemann, C. Vetrice, and H. Neddermeyer, Appl. Surf. Sci. **75**, 125 (1993).

[109] B. Wolf, C. Warner, D. Bonnel, M. Bobeth, S. Baunack, and W. Pompe, Phys. Stat. Sol. A **145**, 319 (1994).

[110] D. Coulman, J. Winnerlin, R. Behm, and G. Ertl, Phys. Rev. Lett. **64**, 1761 (1989).

[111] G. Doyen, D. Dravoka, E. Kopatzki, and R. Behm, J. Vac. Sci. Technol. A **6**, 1761 (1989).

[112] N. Magtoto, C. Niu, M. Anzaldua, J. Kelber, and D. Jenninson, Surf. Sci. **472**, L157 (2001).

[113] J. Doychak, J. Smialek, and T. Mitchell, Metallurgical. Transactions A **20**, 499 (1988).

[114] U. Koops and M. Martin, Solid State Ionics **136**, 971 (2000).

[115] G. Reiss, H. Brckel, and A. Htten, Phys. Rev. B **14**, 339 (1998).

[116] H. Boere, Electron. Lett. **34**, 1754 (1998).

[117] W. Wulfhekel, M. Klaua, D. Ullmann, F. Zavaliche, J. Kirschner, R. Urban, T. Monchesky, and B. Heinrich, Appl. Phys. Lett. **78**, 509 (2001).

[118] M. Bowen, V. Cros, F. Petroff, A. Fert, C. M. Boubeta, J. L. Costa-Krämer, J. V. Anguita, A. Cebollada, F. Briones, J. M. de Teresa, L. Morellón, M. R. Ibarra, F. Güell, F. Peiró, and A. Cornet, Appl. Phys. Lett. **79**, 1655 (2001).

[119] M. Bäumer and H.-J. Freund, Progr. Surf. Sci. **61**, 127 (1999).

[120] L. Z. Mezey and J. Giber, Jpn. J. Appl. Phys. **21**, 1596 (1982).

[121] C. T. Campbell, Surf. Sci. Rep. **27**, 1 (1997).

[122] R.-P. Blum and H. Niehus, Appl. Phys. A **66**, 529 (1998).

[123] I. Costina and R. Franchy, Appl. Phys. Lett. **78**, 4139 (2001).

[124] S. Man'kovsky, A. Ostroukhov, V. Floka, and V. Cherepin, Phys. Met. (Ukraine) **18**, 57 (1996).

[125] J. Méndez and H. Niehus, Appl. Surf. Sci. **142**, 152 (1999).

[126] D. Briggs and M. P. Seah, *Practical Surface Analysis* (John Wiley & Sons, New York, 1983).

[127] A. Stierle, V. Formoso, F. Comin, and R. Franchy, Surf. Sci. **467**, 85 (2000).

[128] R. C. Weast and M. J. Astle, *CRC Handbook of Chemistry and Physics*, 59 ed. (CRC Press, Boca Raton, FL, 1978-1979), pp. D–67.

[129] R. C. Weast and M. J. Astle, *CRC Handbook of Chemistry and Physics*, 70 ed. (CRC Press, Boca Raton, FL, 1989-1990), pp. D–64, D–67.

[130] R. Franchy, M. Eumann, and G. Scmitz, Surf. Sci. **337**, 337 (2001).

Acknowledgments

I would like first to express my gratitude towards my advisor, Prof. Dr. René Franchy. His leadership, support, attention to detail, hard work, daily availability for discussions and his constant support was really essential for my thesis. I thank him also for making my study in Germany possible.

I would like to express my gratitude to Prof. Dr. Harald Ibach for giving me the possibility to make this Ph.D Thesis in the Institut für Schichten und Grenzflächen (ISG-3).

I am very grateful to Prof. Dr. Klaus Schierbaum for accepting to be the co-referee of my thesis.
My special thanks are addressed to Dr. Rudolf David and to Dr. Laurens Verheij for many useful discussions and help.

I am very grateful to Prof. Dr. Emil Burzo for his encouragement and constant support before and during my Ph.D studies.

I would like to thank to Mrs. Christa Elsaesser for useful help and valuable tips.
Special thanks to my colleague and friend Dr. Vitaly Podgursky for his help and useful discussions during the experimental work.
I thank to Mr. Martin Teske for introducing me in the fascinating world of Scanning Tunneling Microscopy.

I also thank to Mr. Udo Linke for high-quality and fast preparation of the single crystals.

I thank to Mr. Norbert Tiefes, to Mr. Dieter Strobl, and to Mr. Rainer Rausch, as well as to all members of Electrical and Mechanical Workshops for rapid and high-quality design and reparation of the devices.
I would like to thank the many graduate and undergraduate students I have worked with in the Institut für Schichten und Grenzflächen (ISG), for useful discussion and for giving me the possibility to know Germany and German people beyond official relationships.

Special thanks to my friend Vasile Caciuc for his constant support and *on-line* LaTeX tips.

Last but not least, I thank to my family, especially to my wife, Adriana, and to my son, Andrei, for their patience and essential affective support during my Ph.D. studies.